**Ana Catarina dos Santos Martins**

Bachelor of Science in Biomedical Engineering

# Computational Neurostimulation: Characterization of electromagnetic fields during Spinal Cord Magnetic Stimulation

Dissertation submitted in partial fulfillment
of the requirements for the degree of

Master of Science in
**Biomedical Engineering**

Advisers: Ander Ramos-Murguialday, Research Scientist, University of Tübingen

Iñaki Ortego Isasa, Research Scientist, University of Tübingen

Co-adviser: Carla Quintão, Auxiliar Professor, NOVA University of Lisbon

Examination Committee

Chairperson: Pedro Manuel Vieira
Raporteur: Pedro Cavaleiro Miranda
Member: Carla Quintão

FACULDADE DE CIÊNCIAS E TECNOLOGIA
UNIVERSIDADE NOVA DE LISBOA

**September, 2018**

**Computational Neurostimulation: Characterization of electromagnetic fields during Spinal Cord Magnetic Stimulation**



This document was created using the (pdf)LaTeX processor, based in the "novathesis" template[1], developed at the Dep. Informática of FCT-NOVA [2].
[1] https://github.com/joaomlourenco/novathesis [2] http://www.di.fct.unl.pt

*You must strive to find your own voice because the longer you wait to begin, the less likely you are going to find it at all.*

*- Tom Schulman, Dead Poets Society*

# Acknowledgements

First and foremost, I would like to express my gratitude to my advisers Ander Ramos-Murguialday and Iñaki Ortego Isasa, who gave me the opportunity to join their research group. They taught me many things that I'll keep in mind for my professional life. I would like to thank the great team I had the pleasure to meet, including Edu, Carlos, Ainhoa, Wala, Andreas, Florian, Judith and Delphin.

Gostaria de agradecer imenso a todo o apoio da minha co-orientadora Carla Quintão, que me ajudou muito a garantir a minha estadia no estrangeiro e me apoiou sempre que eu necessitei, mesmo quando não tinha tempo para o fazer.

À Universidade Nova de Lisboa pela oportunidade maravilhosa de poder realizar a minha tese de mestrado em Tübingen. Ao projeto Erasmus+, porque sem o seu suporte financeiro seria muito complicado realizar esta experiência.

Um grande obrigada à minha família, que sempre me ajudou em tudo o que podia, nunca questionando as minhas capacidades e acreditando sempre que seria bem sucedida.

Grazie mille per tutto Matteo.

Por último, um agradecimento aos melhores amigos do mundo. Por todo o apoio que me deram desde sempre e até agora.

# Abstract

Spinal Cord Magnetic Stimulation is able to change excitability and remodulate the spinal neuronal networks after Spinal Cord Injury. Clinical assessments allow the study of the changes in synaptic efficacy and behaviour after intervention. Nevertheless, the mechanisms underneath recovery are not fully understood. Computational modelling of neurostimulation has been revealed as an important tool to predict the interaction of electromagnetic fields with the biological tissues. Thus, this study is a proof of concept for the use of computational methods to understand the mechanisms of Magnetic Stimulation on the Spinal cord level. The main goal is to calculate the distribution and magnitude of the electric field and electric current density inside the human body during stimulation, both of which were calculated through numerical methods. First, the stimulation devices were modulated and compared with the properties of reference given by the manufacturer. Later, Magnetic Stimulation was studied using a simple model based on the lumbar part of a realistic human model and, finally, in a realistic human model. The results show that the low frequency solver used to solve the electromagnetic problem is in agreement with the basic principles of Magnetic Stimulation. The simulations with the simplistic human model showed that the 8-Figure coil might allow a more focused but less deep stimulation than the Circular coil. Additionally, the use of different electric conductivities led to different electric current density's magnitude. Magnetic Stimulation in a realistic human model allowed us to see the electric field and electric current density inside the body. The results show that the complexity of the human body and the dielectric properties of biological tissues determine the field distribution inside the body. Further studies are required in order to predict the stimulation of the neuronal circuitry in the spinal cord.

**Keywords:** Spinal Cord Injury, Spinal Cord Magnetic Stimulation, Neurostimulation, Computational modelling, Electromagnetism

# Resumo

A Estimulação Magnética da Espinal Medula consegue alterar a excitabilidade e remodelar a rede neuronal depois da lesão da Espinal Medula. A avaliação da condução das fibras nervosas permite identificar alterações da eficácia sináptica e comportamentais. Apesar disso, os mecanismos envolvidos nestas alterações comportamentais não são totalmente conhecidos. Modulação computacional tem-se revelado como uma ferramenta importante para compreender a interação de campos electromagnéticos com os tecidos biológicos. Assim, este estudo é uma prova de conceito para a utilização de métodos computacionais a fim de compreender os mecanismos desencadeados pela Estimulação Magnética da Espinal Medula. O objetivo deste projeto é o cálculo da distribuição e magnitude do campo elétrico e da corrente de densidade elétrica no corpo humano devido à Estimulação Magnética, através de métodos numéricos. No princípio, procedeu-se à caracterização dos aparelhos de estimulação e assegurou-se que estavam modelados conforme o estipulado pela empresa que os produz. De seguida, estudou-se a Estimulação Magnética num modelo simplista baseado na parte lombar do corpo humano e, por fim, no modelo realista do corpo humano. Os resultados demonstram que a aproximação para frequências baixas utilizada para resolver o problema electromagnético vai de encontro aos princípios básicos da Estimulação Magnética. As simulações no modelo simplista do corpo humano revelam que a bobina com a forma de 8 permite uma estimulação mais focal, mas menos profunda que a bobina Circular. Adicionalmente, é evidente que o uso de diferentes condutividades altera a densidade de corrente elétrica. A Estimulação Magnética do modelo do corpo humano permitiu obter a distribuição espacial do campo elétrico e da densidade de corrente elétrica no mesmo. Os resultados demonstram que a complexidade do corpo humano e as propriedades dielétricas dos tecidos biológicos determinam a distribuição do campo elétrico e da densidade de corrente elétrica. No futuro, é necessário realizarem-se mais estudos de modo a prever a estimulação da rede neuronal da Espinal Medula.

**Palavras-chave:** Lesão da Espinal Medula, Estimulação Magnética da Espinal Medula, Neuroestimulação, Modulação Computacional, Electromagnetismo

# Contents

# List of Figures

# List of Tables

# Acronyms

| | |
|---|---|
| B-field | Magnetic Field. |
| CMAP | Compound muscle action potential. |
| CNS | Central nervous system. |
| CPGs | Central pattern generators. |
| cTMS | Continuous transcranial magnetic stimulation. |
| E-field | Electric Field. |
| EPSP | Excitatory postsynaptic potentials. |
| ES | Electric stimulation. |
| FDTD | Finite-Difference Time-Domain. |
| FEM | Finite Element Models. |
| IPSP | Inhibitory postsynaptic potentials. |
| iTMS | Intermittent transcranial magnetic stimulation. |
| LF | Low Frequency. |
| LTD | Long-term depression. |
| LTP | Long-term potentiation. |
| M1 | Primary motor cortex. |
| MEP | Motor-evoked potential. |
| MS | Magnetic stimulation. |
| PAS | Paired associative stimulation. |
| PNS | Peripheral nervous system. |
| QS | Quasi-static. |

| | |
|---|---|
| rTMS | Repetitive transcranial magnetic stimulation. |
| SAR | Specific energy absorption rate. |
| SCI | Spinal Cord Injury. |
| SNAP | Sensory nerve action potential. |
| TBS | Theta burst stimulation. |
| TES | Transcranial electrical stimulation. |
| TMS | Transcranial magnetic stimulation. |
| ViP | Virtual Population. |

CHAPTER 1

# Introduction

## 1.1 Overview

Spinal cord injury (SCI) is a devastating neurological disorder that affects over 130,000 individuals each year and an estimated 2–3 million people worldwide are living with SCI-related disability [1]. This condition can be caused by penetrating bullet wounds (26%), vehicular accidents (38%), sports accidents (7%) and falls (22%) [2]. This disease leads to many obstacles in daily lives and has a great impact on the physiological, psychological and social behaviour of the patient. It causes total or partial loss of sensory and motor capabilities. Furthermore, it can also cause infections in the bladder and kidneys, bowel problems and respiratory and cardiac disfunctions [3]. The motor disfunction varies according to the level of the spinal cord that was injured, mainly causing disfunction below the injury site. Tetraplegia is paralysis caused by a lesion at the cervical spinal cord level and it results in impairment of arms, trunk, legs and pelvic organs. Paraplegia derives from the damage of the thoracic spinal cord: the patient is still able to move its arms but the function of the trunk, legs and pelvic organs is changed, depending on the level of the injury [4]. After SCI, the neural circuits undergo a remodulation in segmental connections due to the loss of supraspinal and propriospinal inputs. This changes dramatically the connectivity in the spinal cord because primary afferents, interneurons and motor neurons change their activity [5]. Scientists believe that neurons can recover from this loss by recreating circuits through neuroplasticity.

Rehabilitation uses plasticity to let the undamaged circuits earn the functionality of the damaged circuits. This means, it aims circuit remodelling instead of regeneration of the damaged tissues [6]. Neurons are excitable cells which can be activated when the transmembrane potential reaches a threshold that leads to membrane depolarization. Slower changes in the membrane potential are mediated by neurotransmitters, which are

released at the synaptic cleft and can give raise to excitatory postsynaptic potentials (EPSP) and inhibitory postsynaptic potentials (IPSP) [7]. The Hebbian theory proposes that learning processes lead to the remodulation of the neuronal circuitry. On one hand, EPSP leads to a long-lasting increase of the synaptic strength in a group of neurons and this phenomenon is called long-term potentiation (LTP). On the other hand, IPSP creates a long-lasting decrease of the synaptic strength, inducing long-term depression (LTD) [8, 9]. During the past years many studies were made using transcranial magnetic stimulation (TMS) to stimulate the damaged areas after injury. This revealed that a phenomenon similar to LTP is induced when the damaged area (cortical or subcortical areas) is stimulated [10]. Furthermore, a paired stimulation where TMS elicites descending motor volleys by stimulating the neurons from the primary motor cortex (M1) and, simultaneously, muscles are activated through electrical stimulation, revealed to also induce similar changes and create associative learning [11].

Spinal cord stimulation changes the excitability of the spinal neuronal networks. The spinal cord can be stimulated through magnetic stimulation (MS) and electric stimulation (ES). Additionally, the stimulation can be non-invasive or invasive, when it is carried on by an external device or a device placed inside the body, respectively. Non-invasive MS is going to be the main topic of the study. MS can interact with the human tissues and, more precisely, with the neuronal circuitry since it produces currents inside the body that can interact with neurons causing their depolarization or hyperpolarization, depending on their orientation in relation to the current.

The big question that is still unsolved concerns the mechanisms that underlie the remodulation of the spinal neuronal networks after spinal cord stimulation. Clinical assessments allow the study of the changes in synaptic efficacy and behaviour after the intervention. Nevertheless, the interaction of external electromagnetic fields created by external devices with the human body and with the neuronal circuitry is not fully understood: What is the field distribution created by the stimulation device? Which neurons are excited by these fields? What are the changes in excitability in these neurons? What are the pathways that are changed and which effect in behaviour does it cause? For this reason, this topic has gained an increased attention in the scientific community. The motor cortex, simultaneously with other parts of the brain, is responsible for planning the movement initiation and execution. At the same time, the connectivity of the spinal cord is extremely important because it determines the quality of the movement. The translation of descending inputs to spinal interneurons and motoneurons allows the existence of movement. The sensory information carried by afferent neurons allows the regulation of movement through different mechanisms. Since spinal neuronal networks are decisive in the quality of movement, the main purpose of this thesis is to study the effect of MS in the spinal cord and peripheral nerves.

This study is a proof of concept to the use of computational methods to study the effects of spinal cord MS and its results are opening more questions and topics that should be further developed due to the limitations of this study. There is lack of information

regarding the dielectric properties of the biological tissues and the neuronal structures by which the spinal cord is composed. Furthermore, it is not possible to estimate the acumulative effect of stimulating with bifasic pulses. Apart from these limitations the study was proceeded as it follows: As a first step, the stimulation devices were studied; as a second step, the effects of MS were studied in a multi-layered model; finally, the field distribution inside the human body. Computational methods, including simulation softwares like Sim4Life [12] and full body human models developed by the IT'IS Foundation [13, 14] might allow to fully understand the mechanisms of electromagnetic stimulation. In the future, we expect to get better rehabilitation strategies that will include activity-based stimulation, leading to targeted therapies in patients with SCI.

This thesis is organized as follows. In the next section of the same chapter the state of the art of bioelectromagnetism, MS and computational models is chronologically revealed. In chapter 2, the theoretical aspects which are important to understand the basis of this study are mentioned. At first, the spinal cord anatomy and the main pathways of movement are described. Then, the basis of neuron activation, including the ionic movement and the modulation of the neuronal activity, is revealed. Afterwards, the physical principles of MS and its parameters that are relevant for neuronal activation will be briefly mentioned. In the end of the chapter, the principles of the computational models, the physics of the solver used in the simulations, the relevance of the dielectric properties of the human tissue are explained in detail. Chapter 3 includes materials that were used and simulations that were done using Sim4Life. Chapter 4 gathers together the results and discussion of these simulations. Chapter 5 presents the main limitations of this study and includes some suggestions for future work and improvements.

## 1.2 State of the Art - Brief Historical Perspective

The electrophysiology was born in 1771 when Luigi Galvani discovered bioelectricity. In 1820, Oersted discovered that currents passing through a coil can create a magnetic field. The principles of MS were explained by the english physicist Michael Faraday in 1881, who discovered that in the presence of a time-varying magnetic field (B-field), an electric field (E-field) perpendicular to this variation would be created. Later, it was discovered that the propagation of a time-varying B-field in the human tissue creates currents inside the body. These currents were named Eddy currents. In 1874, the American physician Robert Bartholow stimulated electrically a patient, producing a contraction. By increasing the intensity of the current, it caused severe problems to the patient. This incident made the public concerned about this technique, which revealed the importance of having safety guidelines of electromagnetic stimulation in humans [15].

In 1980, Merton and Morton built a high-voltage electrical stimulator which could induce the contraction of muscles directly from the scalp. This non-invasive technique was called transcranial electrical stimulation (TES). They placed electrodes on the scalp's surface. A brief, high-voltage electric shock over the M1 led to a brief and synchronous

muscle response. Back then, scientists understood that electric stimulation could be used for many purposes, but it had the inconvenient that it was a painful technique that required some experience in placing the electrodes to diminish pain [16].

In 1985, Baker and colleagues discovered that they could stimulate the brain and peripherical nerves with transcranial magnetic stimulation (TMS) (Figure 1.1). TMS has the big advantage of being also a non-invasive technique which doesn't cause pain. They understood that the stimulation of deeper nerves (median or ulnar nerves in the centre of the forearm) can be induced without pain [17]. Furthermore, they demonstrated that the stimulation of M1 with a single TMS pulse can interact with muscles which receive corticomotor input from the stimulated motor areas [17].

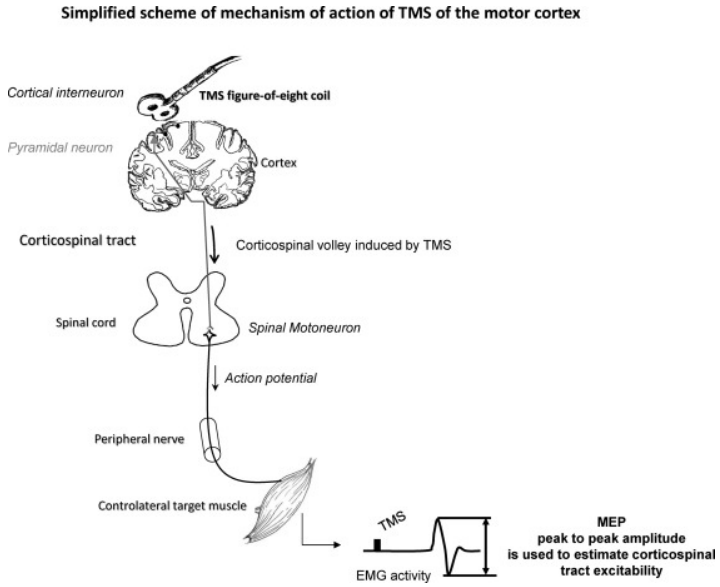


Figure 1.1: Transcranial magnetic stimulation (TMS) applied over the motor cortex. It leads to the stimulation of interneurons preferentially oriented in a plane parallel to the brain surface. As a consequence of the stimulation, the transynaptic activation of pyramidal cells takes place, evoking descending volleys in the pyramidal axons which project to spinal motoneurons. The activation of motoneurons causes the contraction of the muscle innervated by them, which can be measured through electrodes on the surface of the skin. The electrical signal measured is called motor-evoked potential (MEP) (from [18]).

On the $20^{th}$ century, the first studies made in humans were published. These studies showed that TMS could be used to understand the mechanisms underlying cortical and corticospinal reorganization after SCI [19]. Posterior studies tried to understand the impact of the injury on the communication between motor cortex and corticospinal pathways [20, 21]. So, at this point, it was known that SCI changes the organization of M1, corticospinal tract and spinal cord [22]. Appart from this application, TMS has been an important tool in clinical neurophysiology to access the functional integrity of the corticospinal and corticobulbar motor pathways, spinal roots and peripheral roots in many neurological disorders [23].

In 2007, Allen and colleagues discovered that a single TMS pulse could promote the

neural activity during hundreds of milliseconds [24]. In addition, repetitive TMS (rTMS) induced changes that would persist after the stimulation period [25] (see Figure 1.2).

The effects of the frequency of repetition were studied: the application of high-frequency TMS ($\geq$ 5Hz) induces an increase on the neuronal activity [26], while the use of low-frequency TMS ($<$ 5Hz) induces a decreased neuronal activity. If after peripherical nerve stimulation, a TMS pulse is applied to the motor cortex within a difference of time or latency longer than the time required for the afferent inputs to reach the cortex (e.g., 25 ms: $PAS_{25}$) a higher output is obtained [27]. Whereas, if TMS occurs before the afferent stimulus arrives to the cortex, a decreased response takes place [28]. This combination of magnetic stimulation with electric stimulation is called paired associative stimulation (PAS). PAS applied at low frequencies (e.g. 0.05Hz) induces a decreased or increased on excitability depending on the pulse width of each single pulse (see Figure 1.2). The theta burst stimulation (TBS) is similar to rTMS but there is a constant period of non-stimulation between bursts (see Figure 1.2). The TBS can use high frequencies (e.g. 50 Hz) or low frequencies (e.g. 5 Hz) and induce a decreased or increased response, respectively. This is valid both for continuous TMS (cTMS) and intermittent TMS (iTMS) [25] (see Figure 1.2).

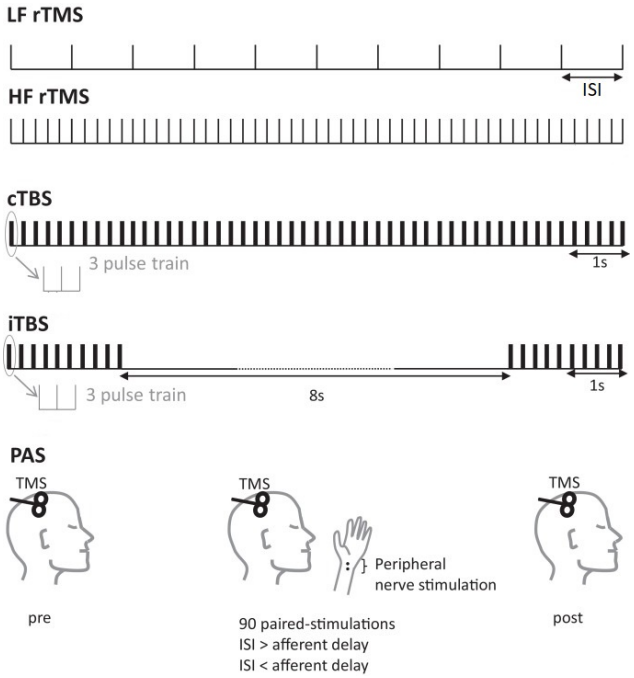


Figure 1.2: Simple rTMS protocols consist of identical stimuli spaced by an identical inter-stimulus interval (ISI). The effects of stimulation depend on stimulation frequency: at low frequency (LF rTMS $< 5$ Hz), rTMS depresses excitability in the motor cortex, whereas at high frequency (HF rTMS $> 5$ Hz), cortical excitability is increased. Continuous Theta burst stimulation (cTBS) involves bursts of high-frequency stimulation repeated with low frequency. In an intermittent TBS (iTBS) protocol, bursts are delivered for a certain time, then repeated with a certain frequency. Paired associative stimulation (PAS) protocols combine TMS over the motor area and a repetitive stimulation of peripheral nerve afferents of the target muscle (adapted from [18]).

The stimulation's parameters play an important role in TMS (see Figure 1.3). In 2001, McConnell understood that regions located further away from the stimulation coil will be less effectively stimulated [29]. In 2009, Pasley and colleagues concluded that neurons which are closer to the threshold stimulation will be more easily activated by the stimulation and that the structural architecture and functional organization of the stimulated area will play a important role in the effectiveness of TMS [30]. In 2011, Di Lazzaro and colleagues demonstrated that by using many TMS protocols it is possible to target specific cortical excitatory and inhibitory networks [31].

It is known that MS can interact with the neuronal circuitry by changing its activity, but the mechanisms underneath this change are not fully understood. Many numerical techniques have been used to calculate the E-field induced by a magnetic coil at the surface of a semi-infinite tissue space, a homogeneous tissue cylinder and a multi-layered sphere. In 1991, a nerve axon in a limb was modelled as a cylinder. The simulation allowed to predict the volume of stimulated tissue within the limb (see Figure 1.4a), the dependence between the threshold stimulus strength, the pulse duration and axon diameter. In this model, the current waveform was described through an RLC circuit (see Figure 1.4a). The

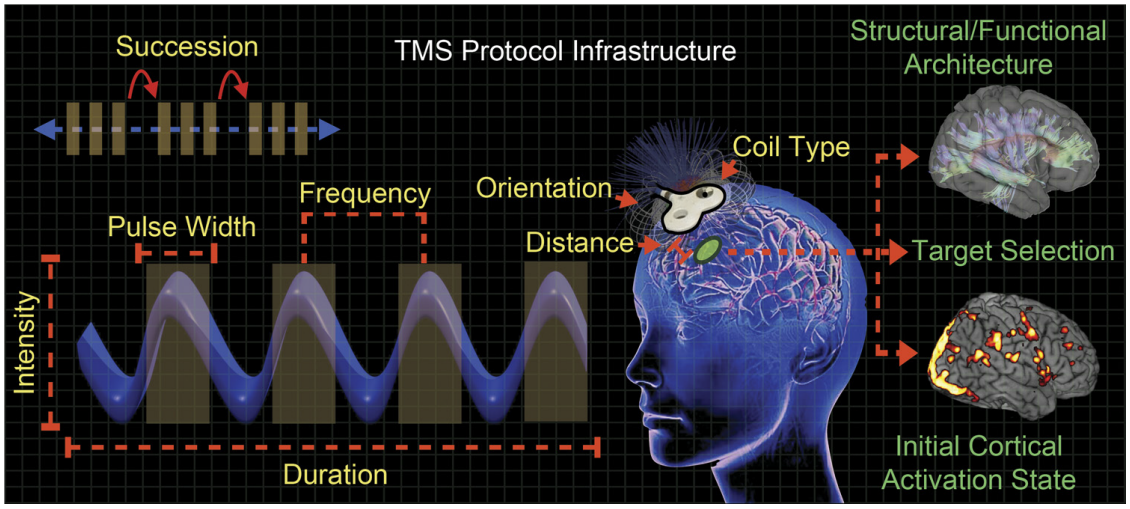


Figure 1.3: Stimulation Parameters in TMS (from [32]).

E-field in the cylinder was calculated by solving Maxwell's equations and the distribution of the transmembrane potential within a cable model (see Figure 1.4b [33]).

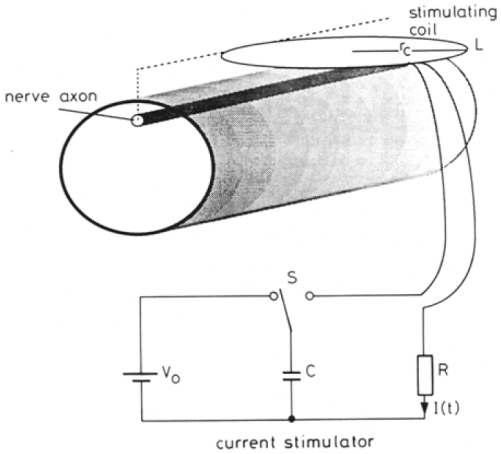


(a) Schematic diagram of the cylindrical limb, nerve axon and stimulating circuit.

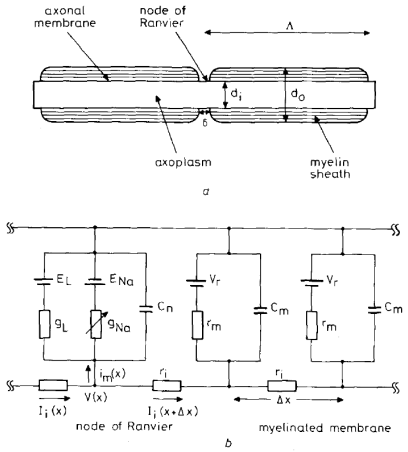


(b) Cable model of the axon membrane.

Figure 1.4: Schematic of the stimulation of a myelinated nerve. The circuit used for stimulation on the left and the model of the axon on the right. From [33]

In 1992, the E-field and the derivative of the E-field were calculated in a semi-infinite tissue, using different coil geometries. They analysed circular, square, double circular, square and quadruple square coils. Additionally, they demonstrated the quasi-static (QS) approach that was followed to obtain the fields. The results showed that the stimulation volume in the square coil is more focused than the generated with the circular coil [34].

In 1994, W. Wang et al. studied the distribution of the E-field and conduction current (J) in tissues where the time rate of change of the applied B-field is low enough that the magnetic diffusion time in the conductive tissues is negligible and so, the J in the tissues dominates the displacement current [35].

In 2010, J. Ladenbauer et al. developed a simulation method utilizing surface electrodes and implants to stimulate the lumbar posterior root fibres and to study the potential activation of the motor neurons within the ventral roots by this two stimulation methods (non-invasive and invasive) [36].

In 2016, Neufeld et al. demonstrated the applicability of functionalized anatomical phantoms with electromagnetic and neuronal dynamics solvers to investigate neuronal stimulation during magnetic resonance imaging [37]. One year after, Davids et al. studied peripheral nerve stimulation during magnetic stimulation in the kilohertz range. They used the model McIntyre-Richardson-Grill model to modulate the myelinated neurons of the peripheral nerves [38].

The dielectric properties of the biological tissues are used to predict the field distribution inside the human body. This leads to the need of acquiring appropriate dielectric properties of each biological tissue. The theoretical aspects regarding this matter were reviewed by Schwan, in 1957, were the dielectric phenomena of the biological tissues and their interaction at cellular level are explained. Posteriorly, other authors studied the same matter. Nowadays, the main references of the dielectric properties are the studies done by Gabriel. First, the information regarding the dielectric properties previously studied was collected. The information revealed discrepancy between the different studies and a gap of knowledge about some tissues at specific frequencies [39]. On a second study, three experimental techniques based on automatic swept-frequency network and impedance analysis lead to the experimental characterization of the dielectric properties of some tissues of the human body in the frequency range between 10 Hz and 20 GHz. The results were consistent with previous measurements. It is also mentioned by the author that this values might have errors bellow 10 kHz and be significant below 100 Hz [40]. Furthermore, in order to facilitate the use of the dielectric properties of the materials, parametric expressions were used to describe them. The most famous models are Debye and Cole-Cole. A study where the dependence of the dielectric properties in function of frequency was modelled and revealed the parameters of the multiple Cole-Cole dispersion equation for some biological tissues [41].

Computational Neurostimulation demands biological models of neural networks to simulate the effects of neurostimulation [42]. The applicability of this branch of science might have a huge impact in experimental and clinical interventions due to use of quantitative models, associating dose to behavioural and clinical outcomes [43]. This methodology could, theoretically, estimate, through forward models like Finite Element Models (FEM), the current flow patterns throught the body, how the currents can depolarize cell membranes, the changes of neuronal firing rates, the way the information is processed and, finally, predict possible behavioural or high cognitive function changes [43].

In 2014, a computational framework, which includes anatomical phantoms of the human body, able to simulate the interaction of electromagnetic fields with complex and anisotropic systems, was developed [44]. Anatomical models with 1 mm resolution, such as the Virtual Population (ViP) [13, 14] are seen as an important tool to model the physical, biological

and physiological processes in the human body [44]. In this software, FEM is used to calculate the E-field and B-field, by solving differential equations on elements, which are defined by the resolution of the model. A database which contains the properties of the tissues of the human body, including electric permittivity ($\varepsilon$) and electric conductivity ($\sigma$) in function of frequency [45], is available online and allows a more accurate calculation of the fields induced in the body.

CHAPTER 2

# Theoretical Concepts

In this chapter all the concepts necessary to fully understand the methodology used to study the effects of MS of the spinal cord and roots are going to be described. At first, the spinal cord anatomy is presented, the microscopic organization of the grey matter and the main functions of the white matter tracts are characterized. Subsequently, a basic description about neural activation is described, generic concepts about synapses, ionic movement and modulation of neurons are mentioned. This section is not important for the results, it was written because this information might turn useful for further studies in this area. Afterwards, the principles of MS, including the most relevant stimulation's parameters are explained. In the end, the principles of computational models are introduced, the solver used by the software to solve the electromagnetic problems is described and the basics principles about the dielectric properties of the biological tissues are explained.

## 2.1 Spinal Cord

### 2.1.1 Anatomy

The spinal cord allows the communication between the brain and the peripherical nerves and can produce spinal reflexes. In the human body, the spinal cord is the extension of the medulla oblongata and extends from the foramen magnum until approximately the level of the disc between the vertebrae L1 and L2 (see Figure 2.1). It is protected by the vertebral column and three membranes, called meninges: *dura mater*, *arachnoid mater* and *pia mater*. Furthermore, between the *arachnoid* and *pia mater* there is cerebrospinal fluid – subarachnoid space – and between the *dura mater* and *periosteum* - epidural space - there is a huddle of loose fibrous and adipose connective tissues. These also contributes to the protection of the spinal cord (see Figure 2.2) [46, 47].

On the posterior part of the spinal cord, the afferent fibres enter and on the anterior

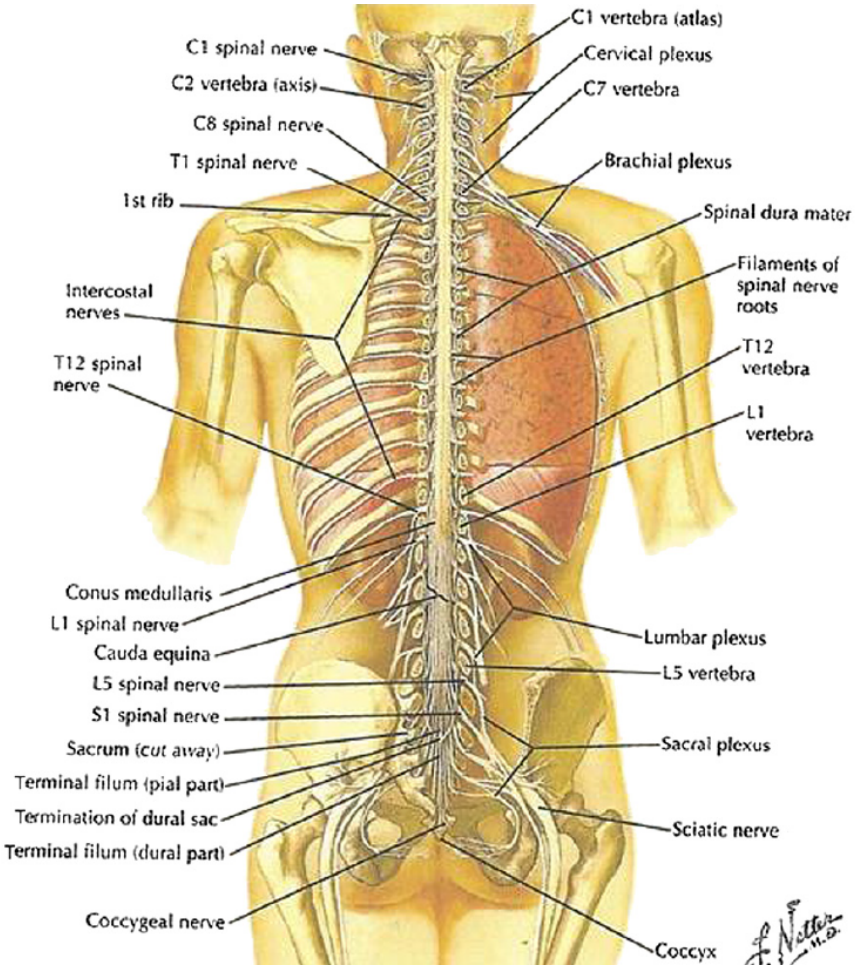


Figure 2.1: Spinal cord anatomy. It shows the distribution of the spinal cord in the human body and the position of each nerve towards the position of each vertebrae.

part, the efferent fibres leave the spinal cord. The afferent axons enter in the spinal cord via the dorsal roots and are responsible for bringing the sensorial information from the peripherical nervous system (PNS) to the central nervous system (CNS). On the anterior part of the spinal cord, in the ventral part, the efferent fibres leave the spinal cord to transmit the motor information to the peripheral circuitry [48]. The dorsal root ganglia, which belongs to the dorsal roots, contains the cell bodies of the afferent neurons (see Figure 2.2). Both afferent and efferent axons connect to each other to form the spinal nerve (see Figure 2.3). The spinal nerves leave the vertebral canal through the intervertebral foramina and each nerve's name is based on the five possible vertebra levels: cervical, thoracic, lumbar, sacral and coccygeal. The cervical nerves are associated to the muscles and glands and receive sensory input from the neck, shoulder, arm and hand. The thoracic nerves are associated to the chest and abdominal wall. The lumbar nerves control the hip and leg. The sacral nerves innervate the lower digestive tract and genitals. The coccygeal nerve innervates the skin over the coccyx [3].

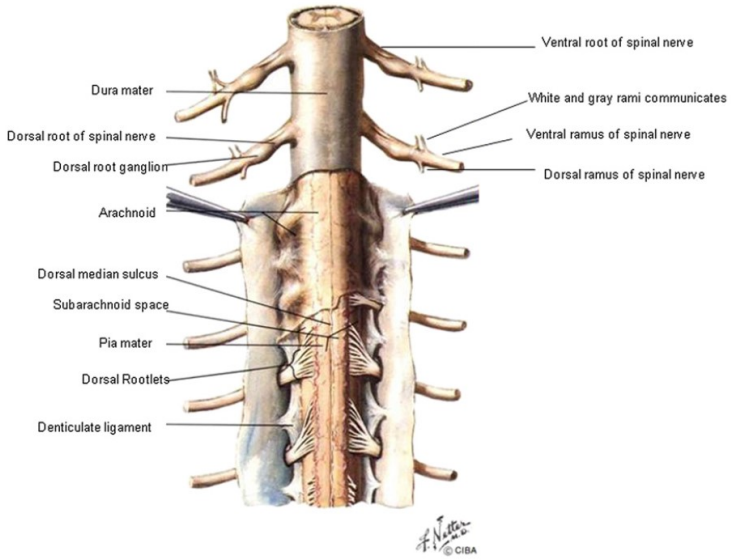


Figure 2.2: Posterior view of the cord indicating the meningeal layers, denticulate ligaments, and dorsal root ganglia (reprinted from Netter Anatomy Illustration Collection, Elsevier Inc. All rights reserved).

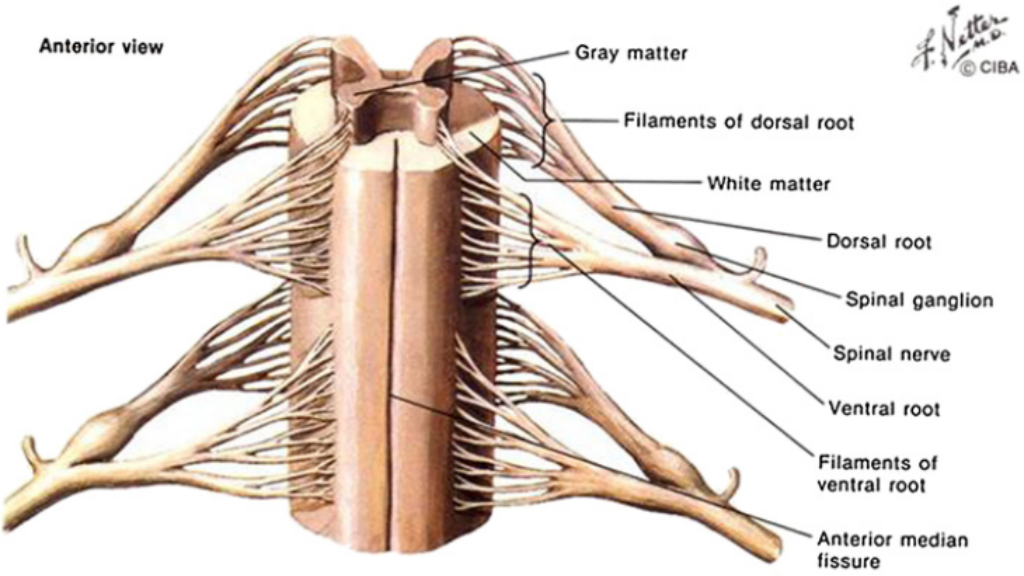


Figure 2.3: Anterior view of the cord showing dorsal and ventral roots of the spinal cord and formation of the spinal nerves (reprinted from Netter Anatomy Illustration Collection, Elsevier Inc. All rights reserved).

#### 2.1.1.1 Gray Matter

The Gray Matter is in the centre of the spinal cord and contains a H-shaped structure. A sagittal cut through the central canal splits the spinal cord in two symmetrical halves that communicate through a narrow bridge or commissure, which is composed of grey and white matter. The central canal is filled with cerebrospinal fluid and it is a continuation of the fourth ventricle [49].

An important division that should be mentioned is the anterior and posterior columns of the grey matter in relation to the coronal section that passes through the central canal, also called ventral and dorsal horns. The dorsal horn receives sensory inputs of all sorts, including the afferents Ia and Ib from muscles but also somatosensory fibres from skin and deeper tissues. The ventral horn contains alpha and gamma motor neurons [49].

In general, the gray matter can be divided in 10 imaginary laminae enumerated as Rexed's Laminae I to X, based on its functional significance. Laminae I-IX are distributed from the dorsal to the ventral of each half of the grey matter. The Lamina X is located around the central canal. In the dorsal horn, Laminae I-V contain neurons which process the sensory inputs and some of this inputs interact directly with the reflex pathways. In the ventral horn, Laminae VI-VII contain most of the interneurons involved in reflexes: the Ia afferent interneurons (IaINs) are found in Lamina VII, Renshaw cells are found in Laminae VII and occasionally found in Lamina IX, the interneurons intercalated in pathways from Golgi tendon organ Ib afferents (IbINs) are in the Lamina VI and in the dorsal part of Lamina VII. In the Lamina VIII and IX can be found the motornuclei for each muscles, being the lamina VIII for axial muscles and the Lamina IX for limb muscle (see Figure 2.4) [50].

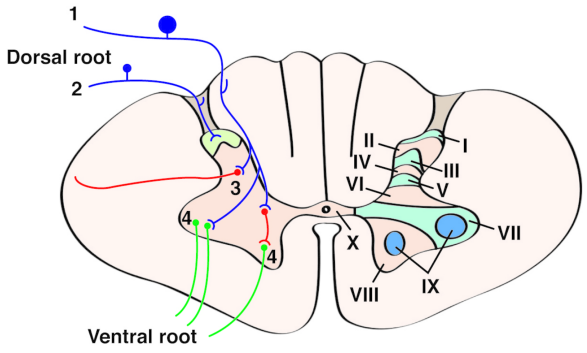


Figure 2.4: The principle afferents, interneurons and efferent are shown symbolically as well as the Rexed's Laminae. The heavily myelinated afferents (1) enter in the posterior funiculus and connect with the interneurons (3) and motor neurons (4). The small diameter afferent (2) enter near the substantia gelatinosa (from [51]).

#### 2.1.1.2 White Matter

The white matter is important to establish the communication between the spinal cord and the brain. The ascending spinal projection connects the spinal cord to supraspinal levels

and transports sensory information. The sensory information includes pain, temperature, position sense and touch from somatic structures and pressure pain and visceral information from internal organs [52].

In the posterior part of the white matter there are two columns called fasciculus gracilis and cuneatus. The fibres are distributed from the sacral to the cervical spinal nerves from medial to lateral, respectively. They transmit sensory information about proprioception, tactile discrimination and vibration sense. The tracts are ipsilateral until they reach the medulla and synapse with their nuclei. The fibres will pass by the medial lemniscus and decussate until they reach the ventral posterior nucleus of thalamus and project their fibres to the somatosensory cortex, passing by the internal capsule [53].

The spinocerebellar tracts are in the posterior and lateral part of the periphery of the spinal cord and carry proprioceptive and cutaneous information. This information is carried from the Golgi tendon organs and muscle spindles to the cerebellum, allowing coordinated movements [54].

The spinothalamic tracts carry nociception, temperature, non-discriminative pressure and touch information to the somatosensory area of the thalamus. This information leads to the compulsion to act and it is responsible for activating a fast response to, for example, pain or itch. The anterior spinothalamic tract transmits the information for touch and the lateral spinothalamic tract transmits the information for pain and temperature [55].

The corticospinal tracts belong to the pyramidal tracts, as the corticobulbar tracts, but they terminate in the spinal cord, while the corticobulbar tract terminates in the brainstem. The pyramidal tracts are responsible for the control of the motor function in the body. At the spinal cord level, the corticospinal tracts are divided in ventral and lateral tracts. They usually decussate, so they are responsible for the control of movement of contralateral muscles. They are originated in the primary, premotor and somatosensory cortex, cingulate motor region within the frontal lobe and also integrate the information from other motor areas, such as the prefrontal, temporal and parietal lobes. It passes through the internal capsule, basis pedunculi of the midbrain and pons. They crossover at the caudal end of the medulla (decussation of the pyramids). From the total number of fibres, 85% will occupy the lateral corticospinal tract and the remaining fibres will form the anterior corticospinal tract. The neurons of the corticospinal tract can interact with the motor neurons, through the interneurons [56].

The rubrospinal tract is small tract in humans. It initiates in the red nucleus, which lays between the rostral part of the midbrain and the upper cervical segments of the spinal cord. This indicates that it doesn't play an important role in the movement of the lower limbs and it was found that it intervenes in the aid of motor neurons which innervate the flexor muscles[56].

The reticulospinal tracts begin in the precentral gyrus, they sinapse in the reticular formation of the brain stem and descend to the spinal cord. In most of the cases, they have inhibitory effects on the alpha and gamma motor neurons. They are mainly involved in the preparatory and movement-related activities, such as movement regulation, postural

control and modulation of sensory and autonomic functions[57].

#### 2.1.1.3 Motor Control

Voluntary movements are initiated in the premotor area of the cortex by the upper motor neurons that form the descending pathways. These upper motor neurons synapse with lower motor neurons that will stimulate the skeletal muscles. The motor activity requires the synchronous activity of many muscles. A motor unit is constituted by the nerve cell, its axons and the muscle that is innervated. The movements that are performed have characteristics such as the force, the target, the velocity of the movement and the type of movement and are performed by activating specific motor units with specific frequencies [58].

In any projected motor performance, the basal ganglia and cerebellum set a pattern and a timing for the stimulation of specific motor units. Smaller motor units are activated by sensory afferents from muscle spindles during reflex activities, postural maintenance, walking and running. The larger motor units are present in phasic movements where there is a burst in the activity of the agonist muscle, followed by a burst in the antagonist muscle [58].

The stretch reflex is a monosynaptic reflex which regulates the skeletal muscle length. When a muscle lengthens, there is an increased activity in the muscle spindle, which will cause the contraction of the alpha motoneuron ($\alpha$-motoneuron) that will lead to the contraction of the muscle and so, regulating the length of the muscle by increasing the resistance of stretching. The gamma motoneurons ($\gamma$-motoneurons) also regulate the stretch by tightening and relaxing the fibres of the spindle [58].

During the flexion of a muscle, the extension of an antagonist muscle takes place, while the agonist or the muscle which is flexed contracts. These two kinds of muscles (agonist and antagonist) are also responsible for stabilizing the fixators. There are two disynaptic spinal pathways responsible for this: Ia reciprocal inhibition and the Ia non-reciprocal inhibition pathways. In the first case, the Ia afferent forms the agonist muscle synapses with a group of inhibitory interneurons (Ia interneurons) that synapse with the motorneuron of the antagonist muscle, causing the inhibition of the motor pool of the antagonist muscle. In the latter case, the Ib interneurons are activated by Ia and Ib afferents and project to the antagonist and the non-antagonist muscle. Furthermore, the inhibition of $\alpha$-motoneuron is done by recurrent inhibition, were the Ia afferent synapses onto the interneurons Renshaw cell, which directly inhibit the $\alpha$-motoneuron [59] (see Figure 2.5). The muscle tone is very important because it is related to the responsiveness of the muscle to stretch and it is ensured by the motoneurons, which innervate the muscle.

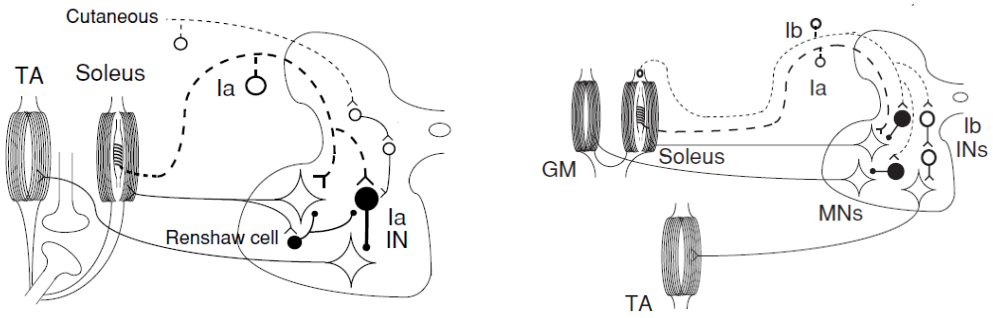


(a) Reciprocal and recurrent inhibition pathways in soleus and tibialis anterior.

(b) Non-reciprocal inhibition pathway.

Figure 2.5: Spinal neuronal networks and their main pathways (From [60]).

Locomotion involves antigravity support of the body, stepping, the maintenance of equilibrium and means of propulsion. The antigravity support implicates antigravity reflexes that lead to the firm extension of the knees, hips and back. Stepping is another important pattern of movement that is integrated in the spinal cord, midbrain and diencephalon. It was also found in animals, such as cats and dogs that this pattern can also be accomplished by stimulating interneurons at the spinal cord level, generally known as central pattern generators (CPGs). Studies in humans did not evidence the presence of the CPGs and it is only known that the gait mechanisms are controlled by reticulospinal, vestibulospinal and tectospinal tracts [58].

The function of the motor and sensory nerves can be studied through nerve conduction studies that use transcutaneous measurements, such as: the compound muscle action potential (CMAP), sensory nerve action potential (SNAP) and Hoffmann's reflex (H-reflex). The parameters that are used to study the synaptic efficacy are the conduction velocity, latency and the amplitude. The measurement of CMAP is done by stimulating the motor fibres with such intensity that all the functional motor fibres are stimulated and the response is measured in the muscle. The SNAP measures the action potentials of the sensory fibres that were stimulated below motor threshold. Finally, the H-reflex elicites the activation of sensory fibres and measures the myographic response at the muscle level, which is specially interesting because it transverses the anterior and posterior roots of the spinal cord [61].

## 2.2 The basis of neuronal activation

The fundamental task of the nervous system is to communicate and process information to regulate the activity of the body. The basic structure of the nervous system is the neuron. Neurons communicate with one another through synapses, which can be either electrical or chemical. The electrical synapses are mediated by intercellular pores or channels bridging the interiors of the neurons synapsing and passing the current flow from one side to another. These are located at the gap junctions and they are sensitive to the transmembrane voltage.

Action potentials trigger the secreation of neurotramitters in the case of chemical synapses. They are mediated by messengers and neurotransmitters that are transported via synaptic vesicles from the presynaptic membrane and doc to the postsynaptic membrane [62] (see Figure 2.6).

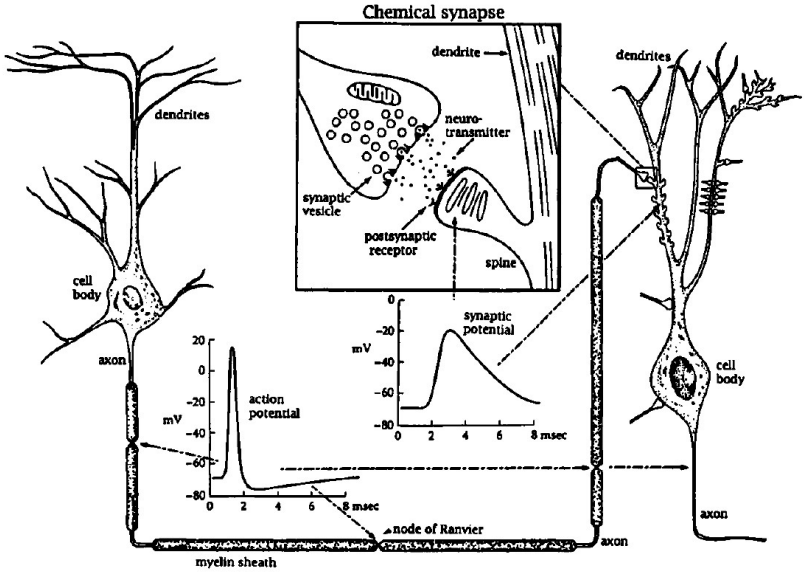


Figure 2.6: Neurons transmit information through electrical and chemical synapses. The electrical signals travel from the cell body of the neuron until the end of the axon in the form of an action potential. These action potentials can trigger the secretion and release of neurotransmitters which can afterwards bind to the postsynaptic receptors, leading to the depolarization of the next neuron (from [62]).

Depending on the type of neuron, its resting potential is usually around -70 mV in relation to the outside of the cell. This is ensured by the permeability and active transport of the cell membrane and the concentration gradients between the intracellular and extracellular mediums. If the potential of the cell increases it might lead to its depolarization and an action potential will take place. Membrane depolarization is characterized by ionic currents generated at the cellular membrane. The action potential takes place due to the presence of voltage dependent potassium ($K^+$) and sodium ($Na^+$) channels [7].

### 2.2.1 Ionic movement

The ions that are more relevant for the nervous system are $Na^+$, $K^+$, calcium ($Ca2^+$) and chloride ($Cl-$). The energy source for the ion movement is the ionic concentration gradient across the membrane which is maintained by ionic pumps. The concentration gradients create electrochemical potentials around the cellular membrane, which lead to the flow of ions in accordance to diffusion due to concentration differences and drift due to potential differences [63]. The diffusion due to concentration differences is mathematically

described by the Fick's law in one dimension:

$$J_{diff} = -D\frac{\partial[C]}{\partial x} \tag{2.1}$$

Where $J_{diff}$ is the diffusion flux in molecule/(sec·cm$^2$), $D$ is the diffusion coefficient in cm$^2$/s , $[C]$ is the concentration in molecules/cm$^3$ and $x$ is distance. This law states that the diffusion flux of molecules tends to diminish the gradient of concentration.

The Ohm's law explains the movement of ions due to the potential differences. Thus, the drift of particles due to the presence of an E-field is as it follows:

$$J_{drift} = \sigma \cdot E = -\mu z[C]\frac{\partial V}{\partial x} \tag{2.2}$$

Where $J_{drift}$ is the drift flux in molecules/(s·cm$^2$), $\sigma$ is the electrical conductivity in molecules/(V $\cdot$ s $\cdot$ cm), $E = \frac{\partial V}{\partial x}$ is the E-field (V/m) and $V$ is the electric potential, $\mu$ is the mobility in cm$^2$/(V $\cdot$ s) and $z$ is the valence of the ion. This law states that the drift of positively charged particles diminishes the electrical potential gradient.

The diffusion coefficient $D$ was described in 1905 by Einstein who described it as a random walk process. Diffusion was then related to mobility as it follows:

$$D = \frac{kT}{q}\mu \tag{2.3}$$

Where k is the Boltzmann's constant (1.38x1023 J/K), $T$ is the temperature in K and $q$ is the charge of the molecule in C. This equation is important because it allows one to compare the two kinds of mechanisms responsible for the flow of ions, since it contains D and $\mu$.

In the case of neurons, the ion movement across the membrane is influenced by E-field and by the concentration gradients. The Nernst-Planck equation describes the ion flow, considering the contribution of the drift and diffusion current or the electrochemical potentials:

$$J = J_{diff} + J_{drift} = -D\frac{\partial[C]}{\partial x} - \mu z[C]\frac{\partial V}{\partial x} = \frac{kT\mu}{q}\frac{\partial[C]}{\partial c} - \mu z[C]\frac{\partial V}{\partial c} \tag{2.4}$$

The Nernst equation expresses mathematically the concentration of ions while the membrane is at rest for the case of equilibrium potential for each of the ions ($E_i$), when the current through the membrane is equal to zero ($I = 0$) because the electric field and the gradient concentration cancel each other. The equilibrium potential ($E_i$) for each of the ions is given by the following equation:

$$E_i = \frac{RT}{zF} ln \frac{[C]_{out}}{[C]_{in}}. \tag{2.5}$$

Where R is the gas constant 1.98 cal/(K $\cdot$ mol), T is the temperature and zF is the total molar charge, z standing for the number of ions and F is equal to the Avogadro number ($N_A$) multiplied by the charge ($q$). The maintenance of the concentrations is ensured by active transport of ions, where ions are pumped out or in from the cellular membrane against the concentration gradient and by selective permeabilities of certain ions.

### 2.2.2 Modelling neuronal activity

Spike initiation in neurons follows the all-or-none principle: after a threshold is reached an action potential will take place and, if this threshold is not reached, there is no propagation of an action potential. After the voltage threshold is reached the neuron depolarization takes place due to the opening of the sodium channels. This biophysical mechanism was first understood by Hodgkin and Huxley in the squid giant axon, which lead to further modelling of the action potential propagation. The depolarization mechanism is also characterized by the refractory period, which is a property that varies according to the kind of neuron that is stimulated. This property might be useful for a targeted stimulation of neurons [64]. Many studies regarding memory and the process of learning have shown that under proper stimulation protocols, the excitability of neurons can be changed leading to a phenomenon called long-term plasticity [65].

In general a membrane of the neuron can be described through a electric circuit (see Figure 2.7). The current through the circuit is:

$$I_m = I_c + I_i = C_m \frac{dV_m}{dt} + \frac{V_m - E_r}{R_m}, \tag{2.6}$$

where $V_m$ is the membrane potential, $I_m$ is the current passing through the membrane ($A/cm^2$), $C_m$ is the membrane capacitance($F/m^2$), $R_m$ is the membrane resistance ($\omega/cm^2$), $G_m = \frac{1}{R_m}$ is the membrane conductance ($S/cm^2$) and $E_r$ is the resting potential of the cell.

The relation between $V_m$ and the ionic current $I_i$ can be linear or non-linear and this defines a linear and a non-linear cellular membrane, respectively. In general, the membrane is linear when the electrical signal is passed to other parts of the neuron in favour of the electrochemical gradient so, the diffusion is passive $\Big(I_i = G_m(V_m - E_i)$, where $G_m$ is constant$\Big)$. In a non-linear behaviour, the membrane is described by a time-varying conductance in respect to the $V_m$ or time.

The membrane polarization for a passive neuron exposed to an E-field can be modulated through the cable theory, which represents a neuron that contains voltage dependent channels as an electrical circuit in a resistive media. This model is presented here since it is the simplest model to describe the behaviour of the neuron towards changes in $V_m$.

#### 2.2.2.1 Cable Theory

While considering small changes in the transmembrane voltage, the neuron can be described as a electronic circuit. The voltage dependent channels can be described with a linear channel conductance and in this way the neuron can be described as an electronic circuit composed of resistances, capacitances and inductances. In the case of the cellular membrane, it is said to be linear when there is a linear relationship between $I_i$ and $V_m$, as it was mention [62]. The representation of the cellular membrane can be seen in Figure 2.7.

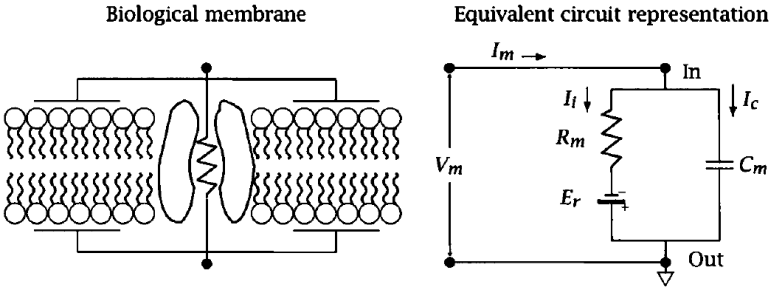


Figure 2.7: Circuit representation of the biological membrane [62].

Usually dendrites and axons can be seen as cylinders, so they are generally seen as electrical conductors, coated by an isolant membrane, myelin. In Figure 2.8 it is possible to see this model, where the $r_m$ is the membrane resistance, $c_m$ is the membrane capacitance and $r_i$ is the cytoplasm resistance, and $r_0$ is the extracellular resistance, $x$ the distance along the cylinder and a is the radius of the cylinder.

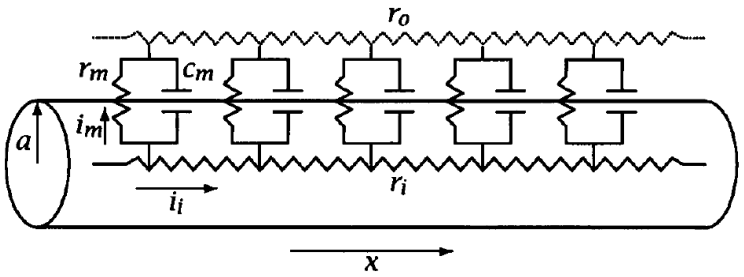


Figure 2.8: The electrical circuit of the conductive cylinder that can model an axon or a dendrite [62].

The first approximation that is made in this model is that the membrane parameters are linear and uniform along the cylinder. This means that these parameters do not change with variations in the membrane potential. Then, the current flow is supposed to be uni directional and along $x$.

The model is described mathematically by the following equation:

$$\lambda^2 \frac{\partial^2 V}{\partial x^2} - \tau \frac{\partial V_m}{\partial x} - (V_m - V_r) = \lambda^2 \frac{\partial E_x}{\partial x} \tag{2.7}$$

where $V_r$ is the resting membrane potential, $E_x$ is the component of the total electric field along the axon (direction $x$), $\lambda$ is defined as space constant and it helps understanding how far a charge can go and it is equal to $\sqrt{\frac{r_m}{r_i + r_o}}$. $\tau$ is the membrane time constant which gives insight about how fast the membrane potential changes in response to changes in current in the cytoplasm and it is equal to $r_m c_m$. The full demonstration and solutions of this equation can be seen in the reference [62]. This expression is important to understand that regions where axons terminate, bend or branch are low threshold points [76].

To conclude, all the elements of a neuron, including dendrites, somas and axons are susceptible to be depolarized due to the E-field created by stimulation devices. The

depolarization might depend on passive or active membrane properties and also on the orientation of the neuron relatively to the direction of propagation of the currents generated inside the body. In general, when the current flows parallel to the neuron the probability that its going to depolarize is higher than if it runs parallel. This happens because, as it is shown in Figure 2.9, a perpendicular current causes both depolarization and hyperpolarization in the same node of the neuron, which doesn't bring any significant effect due to the diameter of the neuron [66].

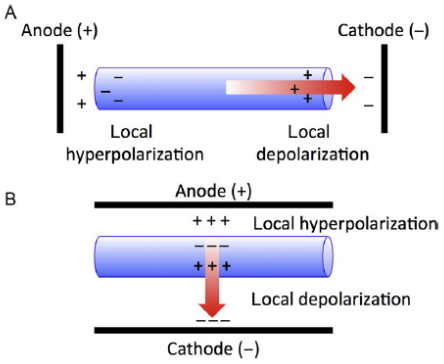


Figure 2.9: (A) Polarization of the cylinder modelling a neuron with parallel electrodes. The current leads to the hyperpolarization of the segment of the neuron the closest from the anode and to the depolarization of the segment the closest from the cathode. (B) Polarization of the cylinder perpendicular to the current flow, which leads to neglectable stimulation due to the small diameter of the neuron, that leads to neglectable interchange of ions (from [66]).

## 2.3 Magnetic Stimulation

MS is a non-invasive and painless technique to stimulate neuronal circuits, due to this fact, it has been used as an alternative method of stimulation to ES [67].

The stimulation of the neuronal tissue is acomplished by placing a coil at the surface of the body with a time-varying current passing through it that varies sufficiently fast to create a strong E-field inside the body and interact with neurons (see Figure 2.10). The rate of current change is proportional to the intensity of the E-field. In Figure 2.11 the MS at the level of the scalp, usually called transcranial magnetic stimulation is shown [68]. A strong pulsed B-field will be generated by the time-varying current passing through the coil. Finally, the time varying B-field creates currents inside the body that might interacte with neurons by depolarizing or hyperpolarizing them [69] (see Figure 2.10).

The stimulation device is transducing coil of high voltage (400V-3kV), high-current (4kA-20kA) discharge system [70]. The time-varying B-field generated can reach a peak strength of 1-2.5 Tesla (T). Nowadays, there are commercial devices that can be used to stimulate in a safe way, Magstim is a company that provides coils and stimulators for these purposes.

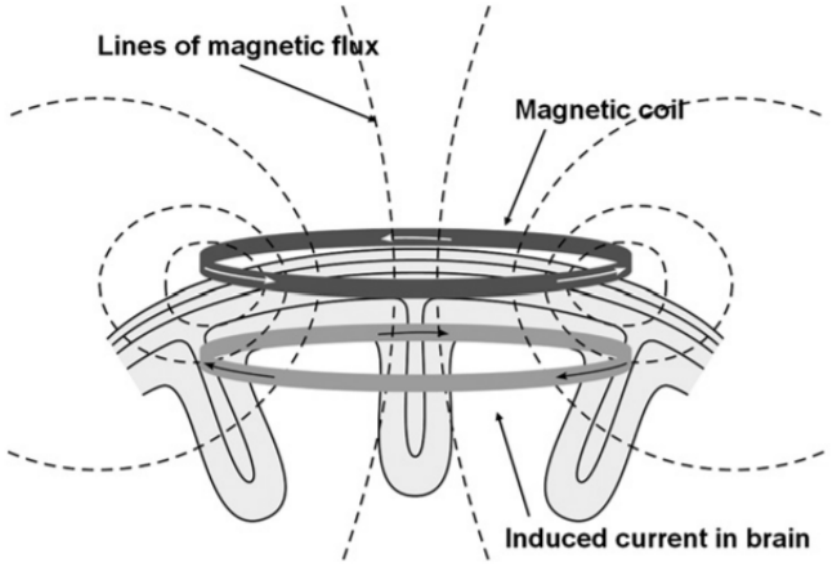


Figure 2.10: The current passing through the coil generates a time-varying magnetic field, that will give rise to a current parallel to the plane of the current passing through the coil, with opposite direction. When this current is high enough, it can lead to neuron depolarization. Figure reproduced from [71].

MS has some parameters that can be changed including the intensity of the current passing through the coil, the location and orientation of the coil, the waveform of the current, the type of coil used for the stimulation and the frequency of stimulation.

The waveform of stimulation is an important parameter that should be taken into consideration. There are mainly two types of waveform, monophasic and biphasic. In both cases, the integral of the E-field generated during the duration of the pulse is zero and its intensity is related to the rate of current change. In the case of the monophasic waveform, it is initiated by a really strong current during 0.1 ms and it is proceeded by a low intensity damped current which has a duration in the ms range. In physiological terms, only the first part of the wave is effective and can interact with the neuronal circuitry. In the case of the biphasic waveform, it is usually a cosine in the range of kHz and it creates a strong current both positive and negative phases of the wave. Due to this, we can say that the biphasic wave is more effective than the monophasic wave because it can interact with the neuronal circuitry during the all duration of the stimulation. Furthermore, since the orientation of the currents is different, it can stimulate different areas [70].

The coil is also an important stimulation parameter since it allows the user to define the volume that is stimulated, giving the possibility to choose between more focal or disperse stimulation. In the case of the Single Circular coil, it can stimulate large volumes in an uniform way, resulting in a less focused stimulation. The 8-Figure coil, which consist in two circular coils in the same plane, has the main advantage of producing a higher E-field in the area where both coils intersect, which means that it produces a more focused stimulation. This is an advantage to the user since it is easy to know the stimulated area [73]. The

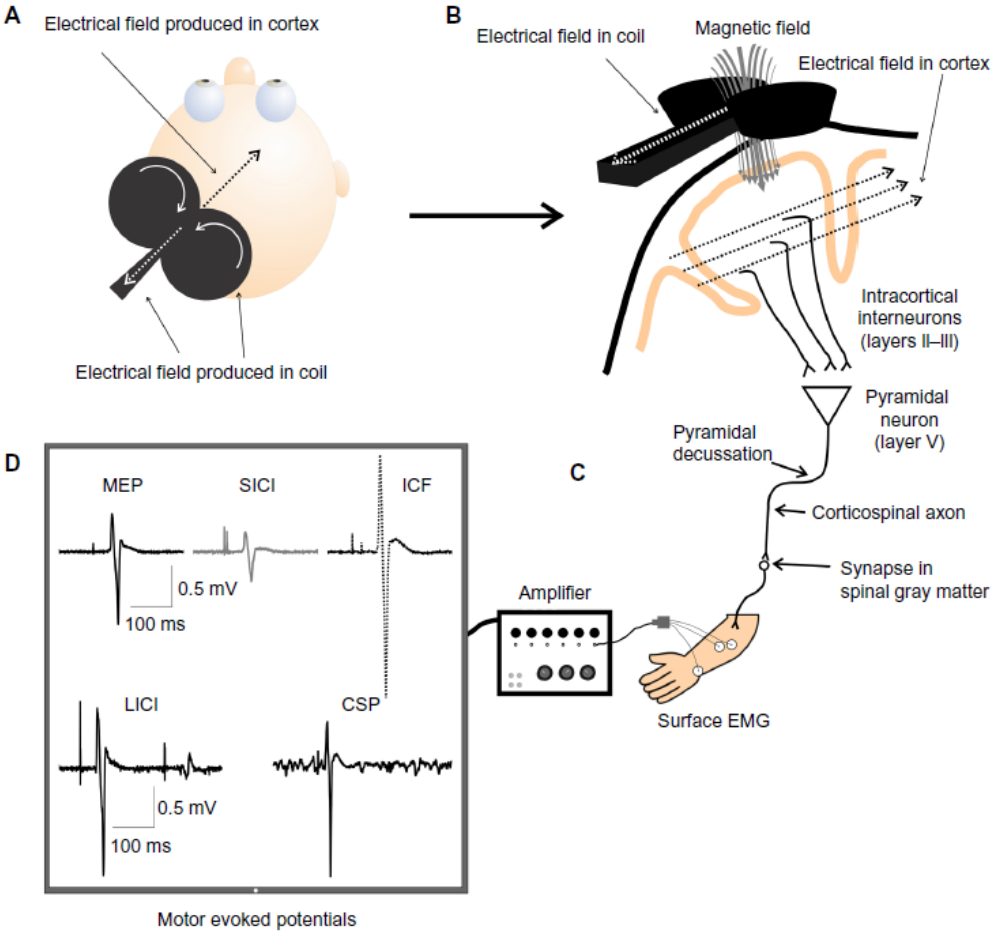


Figure 2.11: Schematic of transcranial magnetic stimulation (TMS). (A) A TMS coil placed over the scalp will generates an E-field in the coil, that will produce an E-field in the cortex in the opposite direction. (B) The E-field produced by the coil induces a B-field traversing the skull and dura. This time-varying magnetic field produces an E-field in the cortex in the opposite direction of the electrical field in the coil. Then, in the cortex, the intracortical interneurons will be activated synapsing on pyramidal neurons and thus activates the corticospinal tract. The descending corticospinal tract then connects to a motor neuron in the spinal gray matter, that will transport the signal to the muscle. (C) The electromyographical response resulting from TMS-induced activation of the corticospinal tract is captured via electrodes recording from the target muscle. (D) Amplified EMG is projected onto a computer screen for quantification of motor evoked potential's (MEP) amplitude and latency. This is another clinical assessment used to avaliate the conduction of nerves. Figure reproduced from [72].

surface of the coil that is in contact with the area of stimulation is also important since, in the case of the circular coil one of the sides has a current that is clockwise and on the other side has a current that is anti-clockwise. The same kind of considerations need to be taken into account for the 8-Figure coil [70].

The depth of penetration of the stimulation is limited by the decay with distance of the B-field. In general, the penetration increases with the stimulus intensity and coil diameter [70]. Smaller coils produce more intense fields at short distance, but their field depth drops more rapidly with distance [74].

Physically, the B-field generated by the coil can be calculated based on the Biot-Savart's law. The E-field created by MS has two sources: (1) the E-field created due to a time-varying B-field in the biological tissues (2) the built up charges in the interface between tissues with different conductivities [68, 75, 76], that will be explained later in this chapter.

Precise spatial location of the stimulation is one of the most important keys for efficient stimulation. One of the biggest limitations of TMS is its spatial resolution. Thus, computational models using Finite Element Method (FEM) can be a useful tool to predict current distributions in very complex heterogeneous media like human body [77].

## 2.4 Interaction of electromagnetic fields with the human body

In our daily life we are exposed to electromagnetic radiation and that's the main reason why this topic became of big relevance. While using MS, subjects are exposed to time-varying B-fields, which create currents inside the human body [70]. In this study, our focus is the effects at low frequency since we only studied the effect of a pulse created by the stimulator 2,5 kHz.

In the literature, the effects of the interaction of the electromagnetic fields with the human body have been obtained by external measurements to the body and also via computational methods. The measurements that are done to assess indirectly to the effects are the specific energy absorption rate (SAR), current density (J) and power density (S), among others. This quantities allowed to construct the restrictions to exposure [78]. It is known that the main effects of the electromagnetic radiation in the human body are dependent on the frequency and for low-frequency there is production of currents inside the body, that can lead to the modulation of the neuronal circuitry. Above 100 kHz, there is a heating effect or an increase of temperature inside the body [78].

At low frequencies and in the presence of an electromagnetic field, there are field forces applied to the particles inside the body and, consequently, currents inside the biological tissues will take place. In the case of time-varying fields, eddy currents are created [79]. These currents can interact with excitable tissue, such as neurons.

Mainly, we can distinguish three main mechanisms to explain the interaction of time-varying electric and B-fields with the human body: coupling to low-frequency E-fields, B-fields and absorption of energy from electromagnetic fields.

In the case of coupling to low-frequency E-fields, the interaction of the time-varying E-fields with the human body results from the flow of electric charge, formation of electric dipoles and reorientation of electric dipoles already present in the tissue. The effects that this kind of interaction can cause vary depending on the dielectric properties each tissue. These properties are mainly the electric conductivity ($\sigma$), which influences the flow of the electric current and the electric permittivity ($\varepsilon$) (influences the magnitude of the polarization effect) and they are dependent on the tissues and the frequency of the field [78].

The effect of coupling to low-frequency B-fields are the induction of an E-field inside the body that gives raise to electric current. This is the main effect of magnetic stimulation. The magnitude of the induced field and the current density is dependent on the radius, of the coil, the electric conductivity of the tissue and the rate of change and magnitude of the magnetic flux density. The exact path of the current varies with the electrical conductivity of the tissue. It is due to this fact that it is so relevant to use human models with high anatomical resolution and contain realistic dielectric properties for each tissue [78].

The absorption of energy from electromagnetic fields is a phenomenon that mostly happens for frequencies higher that 100 kHz because in low-frequency there is no significant energy absorption and no measurable temperature rise in the human body. Between the frequencies 100 kHz and 20 MHz, the absorption in the trunk increases with the increase in frequency and there is a big absorption in the legs and neck. In the range of frequencies from 300 MHz to several GHz, nonuniform absorption takes place and at frequencies above 10 GHz the absorption of energy occurs mainly at the body surface [78].

## 2.5 Modelling and Computational Methods

### 2.5.1 Principles

Computational neurostimulation is a branch of the computational methods that has been growing because it constitutes a powerful tool to understand the mechanisms under neuronal stimulation with MS and electric stimulation.

Computational neurostimulation comprehends four main steps in order to fully understand the interaction of the electromagnetic fields with the neuronal circuitry [43]:

- Use of forward models, for example FEM, to predict the E-fields or currents generated by a source inside the human;
- Create models that predict the response of cells that interact with the fields and currents generated inside the body;
- Understand the consequences of cellular polarization on neuronal information processing;
- Finally, predict if the changes in the network can lead to a behavioural change.

One big challenge for scientists is that the predictions are made without taking into consideration the natural activity of the human body, for example, in the first step, the neuronal activity of the body at the spinal cord level is not taken into consideration. The thing that can be always thought is that, through computational models, it is possible to understand the change that is introduced to the system and so, establish a mechanism of causality [43].

In this study it is necessary to have an accurate model of the human body and the main region of interest will be the trunk, giving special importance to the spinal cord and the nerves. Furthermore, its dielectric properties should be well known, as it will be explained later. The stimulation device must be properly defined, including the geometry and the input current. So, as a first step, an accurate modelling of the system should lead to a proper result of the E-fields or currents generated [43].

In the second step, after the calculation of the macroscopic response of the body to the source, it should be possible to predict the neuronal structures that will be driven to depolarization. The prediction of the E-field allows to understand the region that is most likely to be depolarized [43]. During electromagnetic stimulation, the axon will fire where the negative gradient of the component of the electric field in the axial direction of a Ranvier node reaches a maximum or where the neuron bends. This is matematically described as activation function [80].

In the third step, given the changes of pattern activity in the neurons directly affected by the stimulation, the main purpose is to understand which changes in the network of might be induced [43].

The fourth step comes with the will to link the changes of cellular function to behaviour. The goal is to predict the changes of behavioural changes in real life through simple stimulations techniques that can target a certain function.

### 2.5.2 Calculating the field distribution

The calculation of the field distribution used, solves Maxwell's equations through the FEM and by applying the QS approximation to simplify the procedure. This solver was developed by Sim4Life and it is named Electromagnetic Low Frequency (LF) solver. The main assumptions of the solver are going to be clarified by demonstrating the process that leads to the equations that are used to calculate the E-field and B-field.

At the macroscopic point of view, the interaction of electromagnetic fields with the human body is characterized through Maxwell's equations:

$$\nabla \cdot \vec{E} = \frac{\rho}{\varepsilon}, \tag{2.8}$$

$$\nabla \cdot \vec{B} = 0, \tag{2.9}$$

$$\nabla \times \vec{E} = -\frac{\partial \vec{B}}{\partial t} \text{ and} \tag{2.10}$$

$$\nabla \times \vec{B} = \mu \vec{J} + \mu\varepsilon \frac{\partial \vec{E}}{\partial t}. \tag{2.11}$$

Where $\vec{E}$ is the E-field, $\rho$ is the charge density distribution, $\varepsilon$ is the electric permittivity, $\vec{B}$ is the B-field, $\vec{J}$ is the electric current density or generally called conduction current and $\varepsilon\frac{\partial\vec{E}}{\partial t}$ is the displacement current.

Gauss's law (Equation 2.8) states that the flux of the E-field $\vec{E}$ through any closed surface is equal to the charge inside the volume. In the integral form it is written as $\oint_S \vec{D}\cdot d\vec{a} = \int_V \rho\ dv$ where $d\vec{a}$ denotes the vector element of surface area $a$ normal to the surface and $d\vec{v}$ is the volume element. By applying the divergence theorem the previous equation is obtained [81].

Gauss's law of the B-field (Equation 2.9) states that in any closed the surface, the flux of B-field $\vec{B}$ that enters is equal to flux that leaves the surface. In the integral form it can be written through $\oint_S \vec{B}\cdot d\vec{a} = 0$ [82].

Faraday's law (Equation 2.10) states that the variation in time of the flux of B-field around a volume creates a an electromotive force ($\xi$). This can be expressed as $\xi = -\frac{\partial\phi_b}{\partial t}$, where $\phi_b$ is B-field flux through a surface $\phi_b = \int_S \vec{B}\cdot d\vec{a}$. Furthermore, the $\xi = \int_C \vec{E}\ d\vec{l}$ which means that this is also equivalent $\int_C \vec{E}\cdot d\vec{l} = \frac{\partial\int_S \vec{B}\cdot d\vec{a}}{\partial t}$.

Ampere's law with Maxwell's addition (Equation 2.11) states that a magnetic field is created due to the electric current density and to the displacement current.

In this solver the fields and the input current of the coil are sinusoidal waves, which means that the system is under steady state. The fields can be described as $\mathrm{Aexp}(i(\omega t+\phi))$, where A is the amplitude, $\omega$ is the angular velocity and $\phi$ is the phase. Thus, Maxwell's equations can be rewritten, since the time derivative ($\frac{\partial}{\partial t}$) can be simply replaced by $j\omega$, where $j = \sqrt{-1}$. By doing this substitution, the phasor's form of Maxwell's equations is obtained:

$$\nabla\cdot\vec{E} = \frac{\rho}{\varepsilon}, \tag{2.12}$$

$$\nabla\cdot\vec{B} = 0, \tag{2.13}$$

$$\nabla\times\vec{E}\ = -j\omega\vec{B} \text{ and} \tag{2.14}$$

$$\nabla\times\vec{B} = \mu\vec{J} + \mu\varepsilon j\omega\vec{E}. \tag{2.15}$$

After the rearrangement of Maxwell's equation, the expressions that are going to be used to calculate the B-field and E-field will be described. According to Helmholtz theorem, a sufficiently smooth, rapidly decaying vector field can be resolved by a sum of an irrotational vector field ($\vec{E_I}$) and a solenoidal vector field ($\vec{E_S}$). An irrotational vector field has no curl and a solenoid vector field doesn't have divergence. By definition, the curl of the vector potential $\vec{A}$ is equal to the B-field ($\vec{B} = \nabla\times\vec{A}$) and in Coulomb Gauge $\nabla\cdot\vec{A} = 0$. The E-field can be rewritten by the Helmholtz decomposition[83]:

$$\vec{E} = -\frac{\partial\vec{A}}{\partial t} - \nabla\phi. \tag{2.16}$$

Where $\nabla\cdot\vec{E_S} = \nabla\cdot\frac{\partial\vec{A}}{\partial t} = 0$ and $\phi$ is the scalar potential and $\vec{E_I} = -\nabla\phi$, since $\nabla\times\vec{E_I} = -\nabla\times\nabla\phi = 0$. The $\vec{E_S}$ is the field created by the time-varying current passing through the

coil. The $\vec{E_I}$ is the electrostatic E-field created by the build up in the interface between the two media.

Since the fields are sinusoidal waves, we can write the E-field as:

$$\vec{E} = -j\omega\vec{A} - \nabla\phi. \tag{2.17}$$

The relation between J and E-field is given by:

$$\vec{J} = \sigma\vec{E} <=> \vec{J} = \sigma(-j\omega\vec{A} - \nabla\phi). \tag{2.18}$$

$\vec{J}$ flows accordingly the E-field created by induction. When this field is perpendicular to a surface which separates two tissues, there is a charge build up, creating an electrostatic E-field, that is created to ensure that $\vec{J}$ is continuous.

The Equation 2.15 can be rewritten by plugging it with the following equations:

$$\vec{B} = \nabla \times \vec{A}, \tag{2.19}$$

$$\vec{J} = \sigma\vec{E} + \vec{j_0}, \tag{2.20}$$

$$\hat{\varepsilon} = \varepsilon_r\varepsilon_0 + \frac{\sigma}{j\omega} \text{ and} \tag{2.21}$$

$$\vec{E} = -j\omega\vec{A} - \nabla\phi. \tag{2.22}$$

Where $\hat{\varepsilon}$ is the complex permittivity, $\varepsilon_r$ is the relative permittivity, $\varepsilon_0$ is the permittivity and $\sigma$ is the electric conductivity. These quantities will be studied in the next section. This rearrangement of Equation 2.15 yields in a new expression:

$$\nabla \times \frac{1}{\mu}\nabla \times \vec{A} = \omega^2\hat{\varepsilon}\vec{A} - j\omega\hat{\varepsilon}\nabla\phi + \vec{j_0} \tag{2.23}$$

that is important important because it creates an equation where the variables are just $\vec{A}$ and $\nabla\phi$.

The continuity equation, if there is charge conservation, is $\nabla \cdot \vec{J} + \frac{\partial\rho}{\partial t} = 0$ and states that in an enclosed volume, the variation of charge density is equal to the flux of current density through a surface. This equation can be modified by substituting the following equations:

$$\nabla \cdot \vec{E} = \frac{\rho}{\varepsilon}, \tag{2.24}$$

$$\vec{J} = \sigma\vec{E} + \vec{j_0} \text{ and} \tag{2.25}$$

$$\vec{E} = -j\omega\vec{A} - \nabla\phi \tag{2.26}$$

and the charge continuity equation becomes:

$$\nabla \cdot \hat{\varepsilon}\nabla\phi = -j\omega\nabla \cdot \hat{\varepsilon}\vec{A}. \tag{2.27}$$

when no charges are created ($\nabla \cdot j_0 = 0$) or sources are closed loops.

For low frequencies, the E-field and B-field can be considered uncoupled so, they can be calculated independently. This approximation is valid in the case the size of the objects

which are exposed to the field can be neglected while comparing with the wavelength of the radiation. In this scenario, it can be considered that the fields propagate instantaneously due to their long wavelength. Thus, the QS approximation is verified and the shielding effect of the induced current, as well as the capacitive effect can be neglected. The last assumption, shows that $\vec{J}$ is more relevant than the displacement current (D), for this range of frequencies. To test the validity of the QS approximation the software tests if the condition $(\frac{d}{\lambda})^2 << 1$, where d is the worst-case diameter of the computational domain and $\lambda$ is the wavelength. It is demonstrated in the manual of the software that if this condition is verified, then the two first terms of the right handed side of the Equation 2.23 tend to zero and that the equation can be further simplified as it follows:

$$\nabla \times \frac{1}{\mu} \nabla \times \vec{A} = \vec{j_0}. \tag{2.28}$$

In case the $\mu = \mu_0$, the vector potential $\vec{A}$ can be also calculated through the Biot-Savart's law:

$$\vec{A}(\vec{r}) = \frac{\mu_0}{4\pi} \int_C \frac{\vec{j_0}(\vec{r\prime})}{|\vec{r} - \vec{r\prime}|} d^3\vec{r\prime}. \tag{2.29}$$

In our case, there are current sources so, the current source $(\vec{j_0})$ is different of 0. The vector potential $\vec{A}$ is calculated by solving Equation 2.28. If $\mu = \mu_0$, $\vec{A}$ is calculated with the Equation 2.29. The E-field is obtained by solving Equation 2.27.

For most of the cases in this study, $\sigma >> \omega\epsilon$. Thus, Equation 2.27 can be further simplified:

$$\nabla \cdot \sigma \nabla \phi = -j\omega \nabla \cdot (\sigma \vec{A}). \tag{2.30}$$

By substitution of the values $\vec{A}$ and $\nabla\phi$ in Equation 2.17, the E-field is calculated and the B-field is calculated by $\vec{B} = \nabla \times \vec{A}$.

The dielectric properties of the biological materials including $\sigma$, $\varepsilon$ and $\mu$ appeared in these equations which reveals that they are important for the calculation of the field intensity and distribution inside the human body. In the next section they will be better described.

#### 2.5.2.1 The Properties of biological tissue

The use of computational models depends highly on the dielectric properties to calculate the electromagnetic fields inside the body. The propagation of electromagnetic field in the human tissue varies accordingly to their electric properties. These electrical properties are $\varepsilon$ and $\sigma$ and they vary with temperature and highly on frequency. $\sigma$ influences the flow of the electric current in the body and multiplied by the E-field yields the $\vec{J}$ and it is expressed by S/m. $\varepsilon$ influences the magnitude of the polarization effect and is expressed in F/m [78, 79].

Typically, $\varepsilon$ decreases with frequency and $\sigma$ is low for low frequencies and increases with frequency. The magnetic permeability of the tissues in the human body is really close

to the magnetic permeability of free space, which means that the B-field doesn't alter its distribution while interacting with the human body.

A biological body is made of a complex group of tissues that can be considered as lossy dielectrics and are described by complex permittivity [83]:

$$\hat{\epsilon} = \varepsilon_r - \frac{\sigma}{j\omega} \tag{2.31}$$

In the presence of an external E-field, polar molecules will reorient in a phenomenon called dielectric relaxation. The main dielectric dispersions are called $\alpha$, $\beta$ and $\gamma$. A big modification in the dielectric properties over a frequency range is usually called a dielectric dispersion. At low frequencies, $\alpha$ dispersion gives place and it is associated to the diffusion at the cellular membrane. The study of dielectric properties of biological or any electrolyte system is very difficult due to the electrode polarization in this range. This is one of the reasons why the mechanisms under $\alpha$ dispersion are not fully understood. The dispersion $\beta$, at hundreds of kilohertz, is due to the polarization of the cell membrane, which acts as a barriers to the flow of ions between the intracellular and extracellular media. This effect is also known as interfacial polarization of biological membrane systems or Maxwell-Wagner Effect. Furthermore, there is also the polarization of proteins and organic molecules. At the gigahertz range, there is the polarization of the water molecules, usually named dispersion $\gamma$ [40].

Dielectric relaxation is a frequency-dependent process as mentioned previously. This processed can be expressed through parametric equations, which are characterized by relaxation time constants. The Debye equation describes it through a single-time-constant response:

$$\hat{\varepsilon} = \varepsilon_\infty + \frac{\varepsilon_s - \varepsilon_\infty}{1 \; + \; j\omega\tau} \tag{2.32}$$

Where $\varepsilon_\infty$ is the dielectric constant at high frequencies, $\varepsilon_s$ is the static permittivity at low frequency and $\tau$ is the relaxation time of a material.

Another model is the Cole-Cole and this model is especially relevant for this study since it was used to construct the IT'IS 3.1 database. The IT'IS 3.1 database was constructed based on the dispersion relationships of previous studies [45]. The model used was decribed in a previous study [41], where the dielectric properties of the tissues in each of the dielectric relaxations were described through multiple Cole-Cole dispersion:

$$\hat{\varepsilon} = \sum_n \frac{\triangle\varepsilon_n}{1 + (j\omega\tau_n)^{1-\alpha_n}} + \frac{\sigma_i}{j\omega\varepsilon_0}, \tag{2.33}$$

where $\triangle\varepsilon = \varepsilon_s - \varepsilon_\infty$[1] and $\triangle\varepsilon_n$ is the variation for each term, $\omega$ is the angular frequency, $\alpha_n$ is the distribution parameters for each term, $\tau_n$ is the relaxation time for each term, $\sigma_i$ is the static ionic conductivity, $\varepsilon_o$ is the permittivity in air and $j = \sqrt{-1}$. A four Cole-Cole model was used to get the dielectric properties, since it fitted better the data [41].

[1]The value was fixed to 2.5 or 4 for low and high water-content tissues respectively in the study [41]. The rest of the parameters for each tissue is presented in the article.

In Figure 2.12 the comparison between the experimental data (points) with the 4 Cole-cole model (line) is shown and the three dispersion regions that were described previously are clearly seen for the case of the muscle.

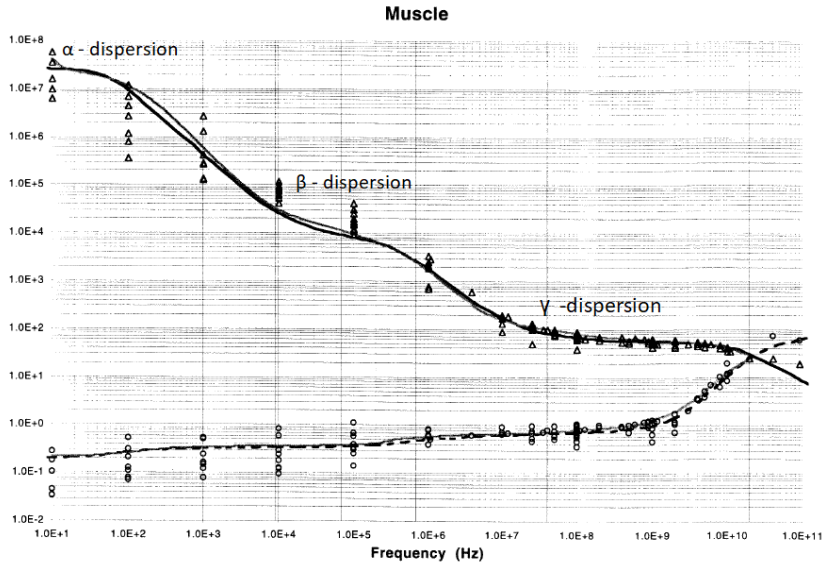


Figure 2.12: Dielectric properties of the Muscle. The dielectric properties were calculated based on the four Cole-Cole model and the three dispersion reagions are evident for this tissue. Figure reproduced from [41].

The dielectric properties of the human tissue are nowadays available for the range of Hz until GHz. The biggest concern about the use of these databases for this study is that they have errors for frequencies bellow 10 kHz.

CHAPTER 3

# Methods

In this chapter the methodology used to study the effects of time-varying magnetic fields within the human body is described. At first, the stimulation coils that were used are going to be physically described based on the information that was given by the manufacturer, followed by the simulations that were done to ensure that they were properly defined. As a second step, a simplified Multi-layered model of the human body is defined to study the impact of the frequency change, the use of different stimulation coils and different dielectric properties on the E-field produced inside the body. Finally, a study with a human body model that will allow the study of the electromagnetic fields distribution in a realistic scenario will be described.

## 3.1 Materials

A computer Fujitsu with a processor Intel Core(TM) i7-7700 and installed memory (RAM) of 64 GB was used to do the simulations. The modelling, calculation and analysis of the field distribution was done by using a commertial software, Sim4Life, that is owned by the company Zurich Med Tech (ZMT) [12]. This software allows solving extremely complex electromagnetic problems. Furthermore, we used the Human-Body models from the IT'IS Foundation [13, 14] in order to compute the field distribution inside the body and finally, two different databases of the dielectric properties were used: IT'IS 3.1 and the IT'IS LF 3.1. To simplify the language from now on, the first database will be mentioned as standard and the and low frequency (LF). These tissue properties databases belong both to the IT'IS Foundation and were constructed based on the studies that used the Cole-Cole model [45] and a review of other studies. In the case of the standard database, the properties vary within the frequency range from Hz until GHz and its limitations are evident for low frequencies as it was mentioned before. The LF database used fixed values

of $\sigma$ and $\varepsilon = 1$ for all tissues and all the frequency range until 1 MHz. The latter database was done based on evidences that show that there isn't a big change in $\sigma$ in this range of frequencies and the fact that $\varepsilon$ doesn't play an important role in solving electromagnetic problems in this frequency range.

### 3.1.1 Sim4Life

Sim4Life is a simulation platform that can simulate the interaction of electromagnetic waves with the human body through solvers that can calculate at the macroscopic level and at the microscopic level. The main solvers offered by this software are: Electromagnetic Finite-Difference Time-Domain (FDTD) solver, Electromagnetic LF solver, Thermal Solver, Flow Solver, Acoustic Solver and Neuronal Dynamics Solver. All the information that is calculated with the solvers can be processed afterwards in the software or exported to other programs in other to analyse the data [12].

In general, the main application of this software is to understand the interaction of electromagnetic waves with the human body since it is one of the most complete softwares in this area, allowing to solve complex electromagnetic problems. It can be used in deep brain stimulation, in transcranial magnetic stimulation, in nerve stimulation [80], stimulation due to magnetic resonance imaging, the effect of gadgets like smartphones in our daily routine, the effects of ultrasounds and other possible therapies, calculate the safety limits of exposure to new devices that might constitute a new therapy. These are some of the possible applications that this software can have. In order to calculate the field distribution inside the human body, the software needs Human-Body models.

### 3.1.2 Virtual Family

In this section, the research and developments performed to achieve the most actual anatomical models are going to be mentioned.

The Virtual Family (ViP) is a computational whole-body anatomical human models that arose from the need of simulating the interactions between various environments human body (Figure 3.1). The complex geometry of the human body is an important feature for a more realistic simulation, allowing a better comprehension of the effects inside the body with external sources. Although these models represent a huge improvement of the models used in the past, it is important to keep in mind that they need further improvement.

Depending on what is studied by each simulation, different levels of resolution are needed. For example, in the case of studies regarding the stimulation of the neural system, it is needed to have a resolution that goes until the cellular level, which makes also the computational procedure much more challenging. In general, the limitations of these models have to do with the lack of accuracy and detail in certain regions. Towards making these models more useful, it is necessary to create more specific models that are compatible and can be imported to the general model of the human body [14].

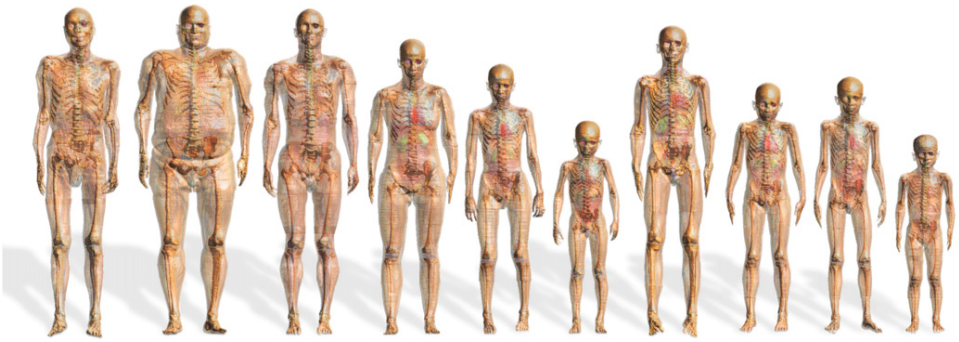

Figure 3.1: The complete Virtual Population from IT'IS foundation representing humans of different age groups and body shapes. Figure reproduced from [14].

The Virtual Population has been widely used in order to solve questions such as exposure, the effects of mobile phones, wireless devices, magnetic resonance imaging scanners, safety of medical treatments, product development and optimization and other questions respecting basic research.

The design of each anatomical model needed the following steps [14]:

- Recruitment and scanning of whole-body of volunteers;
- Pre-processing of magnetic resonance imaging data which was acquired with a 1.5 T scanner on a Magnetic Ressonance machine as explained in [14];
- Segmentation of medical image data to generate a label-field so, distinguishing the different tissues of the human body, the software iSeg (ZMT Zurich MedTech AG, Switzerland) was used for this purpose.
- Processing the label-field to remove artefacts;
- Processing of surfaces, including extraction simplification and smoothing of surfaces and finally create a surface model.

Resonance images is subjective and there are some areas where it is difficult to distinguish the end of an organ and the beginning of another. For example, the transition of the midbrain, pons, medulla oblongata and spinal cord are not strictly defined. Another issue is the limitation of the resolution of the model, structures with smaller diameter that 1 mm are ignored and therefore the nerves are not defined. In Reference [14] it is possible to see the full description of the tissues included in each model. The most important regions for this study is the spinal cord and the nerves, the spinal cord, the dorsal and ventral root, the sciatic and tibial nerves are included [14].

## 3.2 Magneto Quasi-Static Solver

The mathematical description of this solver is characterized in Section 2.5. In this part of the text, the most important settings used to perform an electromagnetic LF simulation

are described.

The main structure of the the solver is as it follows:

- Setup: the frequency that is used to define the fields and the dielectric properties is selected here;
- Materials: the materials that were modelled are here defined. The user defines the properties that each of the materials will have;
- Current Sources: the amplitude of the source is defined in this part;
- Boundary conditions: for the Magneto Quasi-Static Solver the all boundary conditions are neglected as zero Neumann boundary conditions, which means that the normal flux vanishes;
- Sensors: the volume where the fields are going to be calculated is established here, as well as the data that is recorded for the simulation;
- Grid: to define the resolution of the model. Here it is possible to define the number of cells were the Maxwell's Equations will be calculated;
- Voxel: create the voxels based on the grid previously defined. The voxels are created based on the Topological Voxeler, where the geometry of the object that is modulated is the starting point for the discretization;
- Solver: contains all the settings related to the solver, such as convergence related settings.

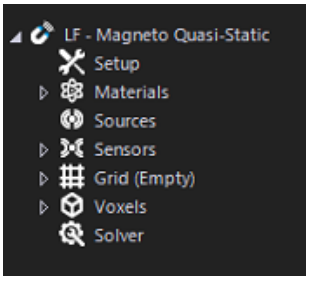


Figure 3.2: The structure of the solver.

## 3.3 Characterization of the stimulation devices

The stimulation unit and coils are shown in Figure 3.3. The magnetic stimulator unit used is the Magstim Rapid$^2$ (Figure 3.3a). This device is produced by the company Magstim. It is a stimulator unit that delivers biphasic current pulses to the coils which are connected to it. More specifically, the current pulse that passes through the coil is sinusoidal with a shape of a A*sin($2\pi$ft), where A is the peak intensity and f is the

frequency. The frequency of the waveform is 2500 Hz, but this value might vary slightly due to differences in coil's inductance. So, as it was mentioned in the previous chapter, the solver makes the approximation that all the fields are sinusoidal waves, which limits us to the study of sinusoidal waves. Thus, we will study only the effects of the stimulation with a single pulse of 2500 Hz. In fact, the variation in time of the current ($2\pi A\cos(2\pi ft)$) is proportional to the E-field, since the vector potential $\vec{A}$ it is calculated based on the Biot Savart's Law (Equation 2.29).


(a) The magnetic stimulatior unit.

(b) Single 90 mm Coil by Magstim.

(c) Double 70 mm Coil by Magstim.

Figure 3.3: The stimulator and coils used in this project.

The main characteristics of both coils were used for modulation are present in Table 3.1. The peak current is a parameter characteristic of the coil and is kept constant in all the simulations, so it won't be further mentioned. This means that the simulations that are shown correspond to a stimulation at 100% intensity in reality.

Table 3.1: Specifications of the Double 70 mm Coil and the Single 90 mm Coil.

| Coil | Double 70 mm Coil | Single 90 mm Coil |
|---|---|---|
| Average conductance ($\mu$H) | 15.5 | 23.47 |
| Inside diameter (mm) | 56 (x2) | 66 |
| Outside diameter (mm) | 87 (x2) | 123 |
| Number of turns | 9 (x2) | 14 |
| Peak Current (A) | 5600 | 4800 |

The Circular coil that was used is the Single 90 mm Coil (Figure 3.3b). The modulation of the coil in the software Sim4Life is shown in Figure 3.4. This coil is usually used for the stimulation of the lumbosacral nerve roots.

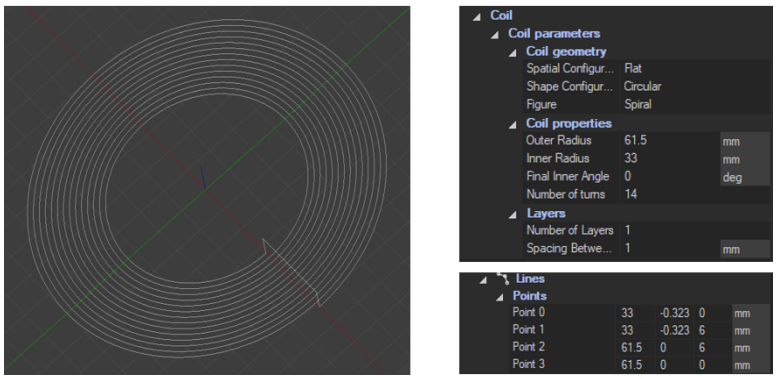


Figure 3.4: Circular coil model in Sim4Life. On the left side, it is possible to see the physical model of this coil. On the right side, on the upper part, the coil's spiral is parametrized and, on the lower, the line that connects the extremities of the coil is defined.

The 8-Figure coil that was used is the Double 70mm Coil (Figure 3.3c). In Figure 3.5, the modulation of the coil is shown. This coil is usually used for excitation of spinal roots and the peripheral nerves [84].

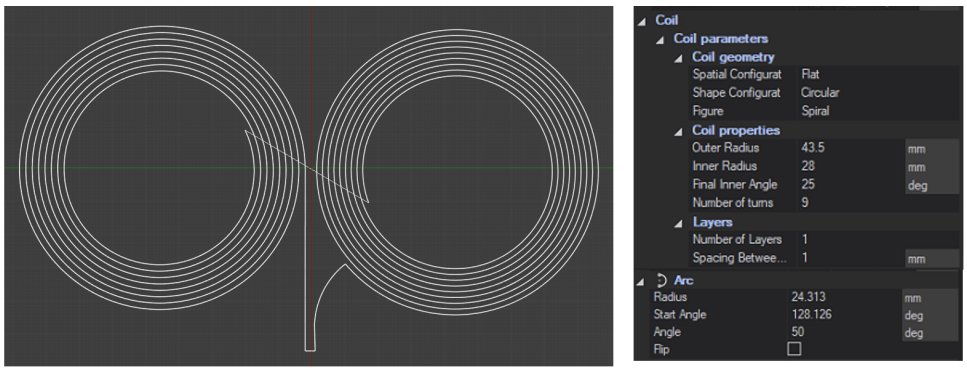


Figure 3.5: 8-Figure coil model in Sim4Life. On the left side, there is the physical model. This model is constituted by two equal spirals, two lines and an arc. On the right side, on the upper part, the spiral is parametrized, on the lower part the arc is defined and the other two lines that connect the rest of the elements.

The model of the Circular coil and 8-Figure inside air and next to a conductive medium

are shown in Figure 3.6. This layer of air was used to mimic the cover of plastic that covers the coil.

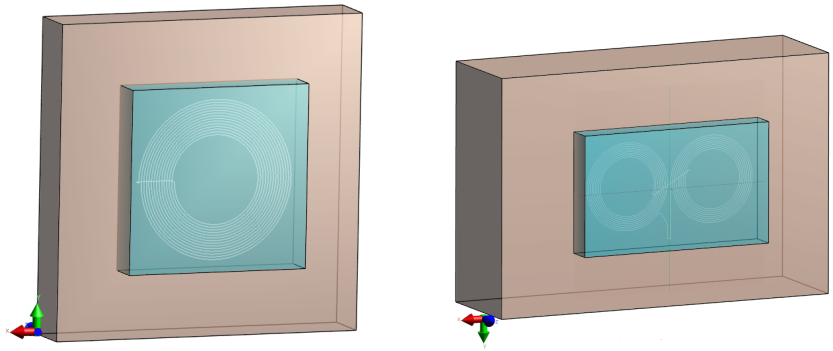

(a) Model of the Circular coil. The air's volume 140x141x26 $mm^3$ and the skin's volume 240x240x41 $mm^3$.

(b) Model of the 8-Figure coil. The air's volume is 194x118x26 $mm^3$ and the skin's volume is 345x234x105 $mm^3$.

Figure 3.6: Models of the two coil involved in air (blue volume), which represents the cover of the coil in reality and skin (brown volume), the dielectric material that will be used to calculate the E-field.

The quantities that are going to be considered to understand the validity of the modulation of the coils are the inductance, the B-field (T) and the E-field (V/m) distribution. The Peak Magnetic Field for the Circular coil is 2 T and for 8-Figure coil is $\geq$ 0,92 T. The inductance values are shown in Table 3.1 and the field distribution and intensity can be seen in Figure 3.7 for both coils.

In order to replicate the values that were given as a reference for the two coils, simulations in air were done to measure the B-field produced by each of the coils, as well as their inductance. Additionally, simulations in a dielectric material, such as the skin, were used to measure the E-field created.

The simulations done in air are summarized in Table 3.2 and the grids used are shown in Figure 3.8. In all the cases the frequency used for the simulation in 2500 Hz. The volume where the fields are calculated is left as default. The effect of considering the coil a current path or a real coil made of copper, with a wire with 1 mm of radius was studied with simulations LF1 and LF2, as well as, with LF3 and LF4.

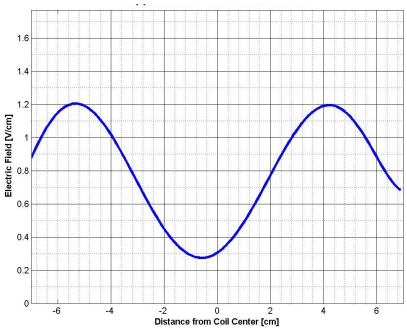


(a) E-field measured at the coil surface in a saline solution, in the case of the Circular coil.

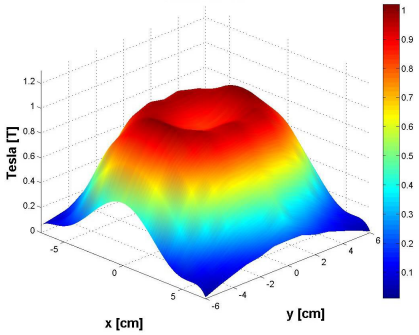


(b) The B-field distribution in air for the Circular coil.

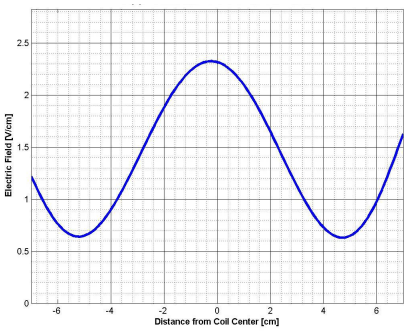


(c) E-field measured at the coil surface in a saline solution for the 8-Figure coil.

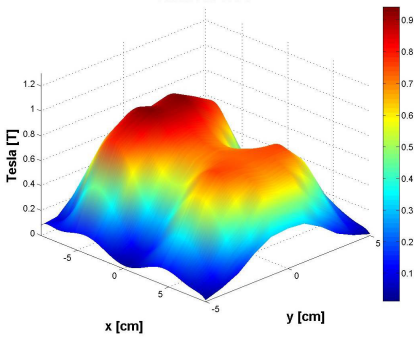


(d) The B-field distribution in air in the case of the 8-Figure coil.

Figure 3.7: The E-field and B-field distribution for the Circular coil and 8-Figure coil.

Table 3.2: Specifications of the simulations done in air.

| Name | Coil | Materials | Current (A) | Grid | Voxels |
|---|---|---|---|---|---|
| LF1 | Circular | Air (Background) | 4800 | 151x149x34 = 764.966 kCell | Topological Voxeler |
| LF2 | Circular | Air (Background), Copper (Coil) | 4800 | 151x149x34 = 764.966 kCell | Topological Voxeler |
| LF3 | 8-Figure | Air (Background) | 5600 | 203x126x32 = 818.496 kCell | Topological Voxeler |
| LF4 | 8-Figure | Air (Background), Copper (Coil) | 5600 | 203x126x32 = 818.496 kCell | Topological Voxeler |

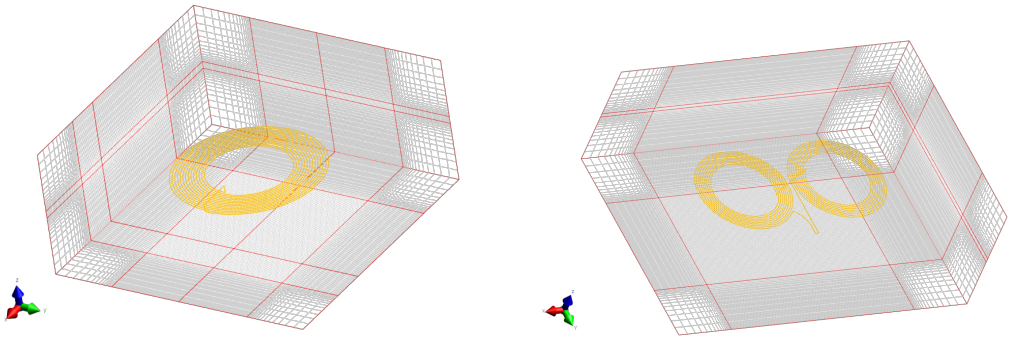

(a) The grid used for the simulations of the circular coil in air.

(b) The grid used for the simulations of the double coil in air.

Figure 3.8: Grids used for the simulations of the devices in air.

In Table 3.3 the simulations used to calculate the E-field in skin are shown. The voxelization was done by splitting the coil from the rest of the material and attributing a higher priority to the coil than the other materials to ensure the proper voxelization of the system. The grid was obtained by splitting the coil from the rest of the materials, which is fundamental because the volume that comprehends the coil is the most relevance, so it should have a higher resolution. The grid of the coils was obtained by using the manual mode, with a maximum step of 1 mm and a resolution of 0 mm. The grid of the materials was defined as default in the automatic mode. The grid of both coils can be seen in Figure 3.9. The effect of considering the coil a current path or a real coil made of copper with 1 mm radius was studied between simulation LF5 and LF6, as well as with LF7 and LF8.

Table 3.3: Specifications of the simulations done with the circular coil interacting with other materials.

| Name | Coil | Materials | Grid | Voxels |
|---|---|---|---|---|
| LF5 | Circular | Air (Background), Air (Cover), Skin (Conductive material) | 164x164x44 = 1.183 MCells | Topological Voxeler |
| LF6 | Circular | Air (Background), Air (Cover), Skin (Conductive material), Copper (Coil) | 164x164x44 = 1.183 MCells | Topological Voxeler |
| LF7 | 8-Figure | Air (Background), Air (Cover), Skin (Conductive material) | 221x140x46 = 1.423 MCells | Topological Voxeler |
| LF8 | 8-Figure | Air (Background), Air (Cover), Skin (Conductive material), Copper (Coil) | 221x140x46 = 1.423 MCells | Topological Voxeler |

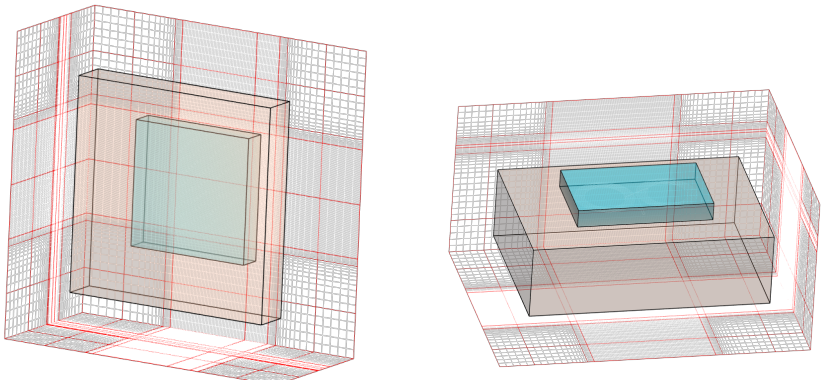

(a) The grid used for the simulations of the Circular coil.

(b) The grid used for the simulations of the 8-Figure coil.

Figure 3.9: The grids used both coils for the simulations that allowed the study of the interaction of them with the skin.

## 3.4 Multi-layered model

The Multi-layered model was done in order to have a simple model which would allow an estimation of the interaction of the electromagnetic fields generated by the stimulation device with the human body. The thickness of each layer of the Multi-layered model can be seen in Table 3.4.

Table 3.4: Layers of the Multi-layered model.

| Layer | Material | Thickness (mm) |
|---|---|---|
| $1^{st}$ Layer | Skin | 3 |
| $2^{nd}$ Layer | Subcutaneous adipose tissue (SAT) | 15 |
| $3^{rd}$ Layer | Muscle | 30 |
| $4^{st}$ Layer | Fat | 6 |
| $5^{th}$ Layer | Bone | 10 |
| $6^{th}$ Layer | Fat | 10 |
| $7^{th}$ Layer | Nerve | 5 |
| $8^{th}$ Layer | Fat | 20 |

As a first step, the model Ella from the Virtual family, from the IT'IS foundation, Ella, was transformed in voxels with a maximum step of 1 mm and resolution of 0 mm and then a transversal cut of its trunk in the lumbar area was done as it is shown in Figure 3.10. The tissue of most relevance is the nerve. This is the reason why the tissues that are located between the stimulation coil (which is located on the posterior part of the lumbar level) and the nerve were used to build the model; tissues that are located further away from the nerves are not going to be considered.

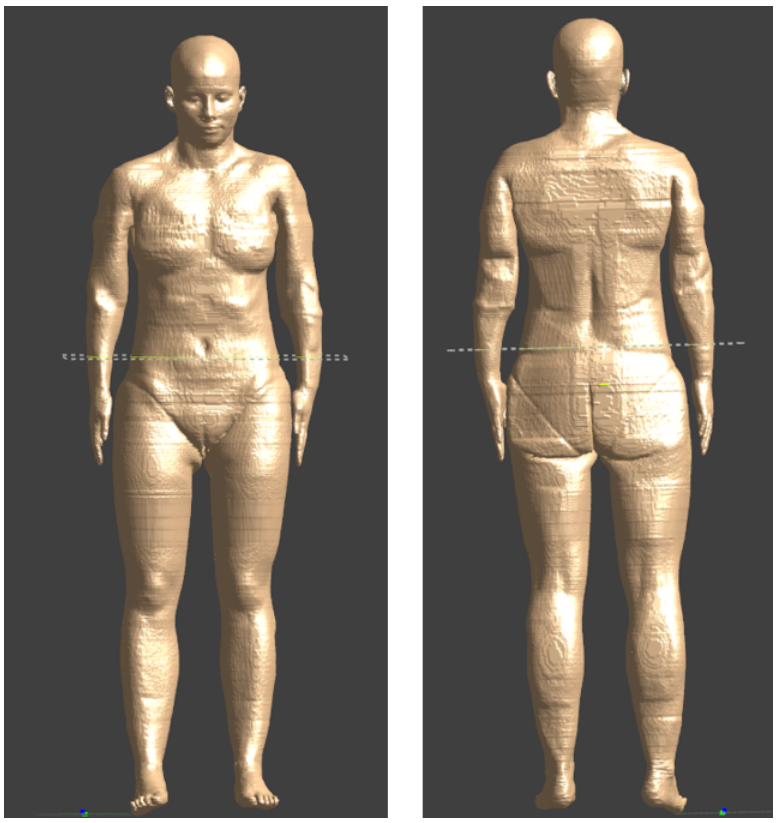

(a) The plane at which the transversal cut was done is at Z=985 and it is shown by a white line.

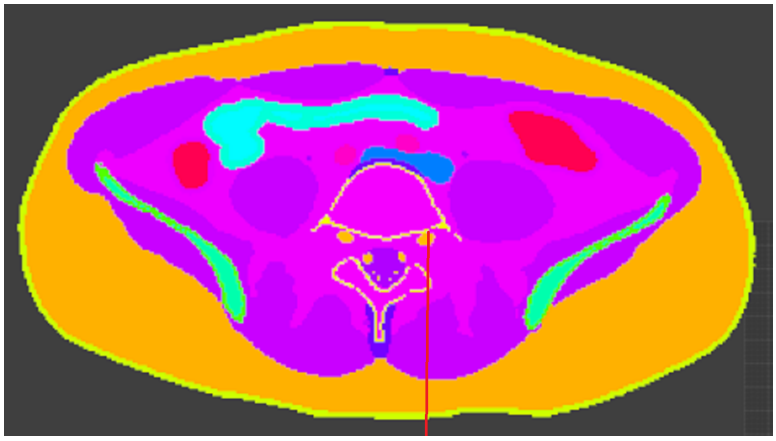

(b) Transversal cut which shows the distribution of the tissues.

Figure 3.10: Transversal cut of Ella at Z=985, which will be used to construct the Multi-layered model. The structure that is of most relevance is the nerve, due to this, the tissues that will be used for the model are involved by the red line shown in the transversal cut.

The final model can be seen in Figure 3.11. The last layer of fat was added to the simulations, only to ensure that there is no loss of information in the block of interest (7th layer - Nerve).


Figure 3.11: Multi-layered model. The area of each layer is 355x355 $mm^2$.

This model was used to study the effects of the change of the coil, the frequency of the pulse and dielectric properties of the biological tissues. The grid for each of the simulations was acquired by dividing the coils and the layers of the Multi-layered model. By doing this, the user can improve the resolution of a certain volume in the simulation, as it was already mentioned. The grid around the layers was constructed by using the "Very Fine"refinement in the automatic mode and the grid for the coil was constructed by using the manual mode were the maximum step was set to 1 mm and the resolution to 0 mm.

### 3.4.1 The effect of the stimulation coil

In this section the Circular coil and the 8-Figure coil are compared in the Multi-layered model. The main purpose of this set of simulations is to study the interaction of the coils with the Multi-layered model. Many experts claim that the 8-Figure coil allows a more focused stimulation. This will be studied with the dielectric properties from the standard database. The models that are going to be used can be seen in Figure 3.12 for both coils. The simulations that were done are summarized in Table 3.5.

(a) The Multi-layered model and the Circular coil.

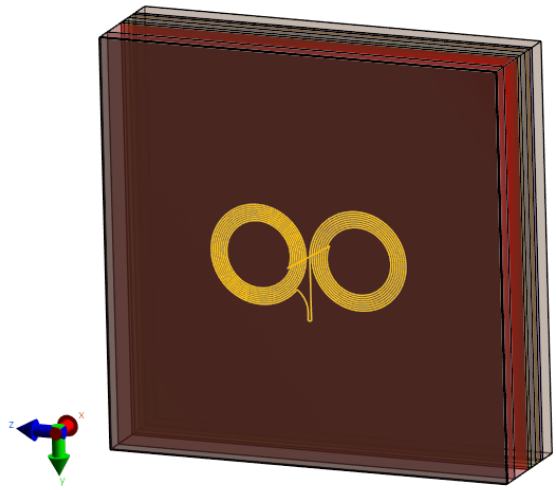

(b) The Multi-layered model and the 8-Figure coil.

Figure 3.12: The stimulation coils and the Multi-layered model.

| Name | Coil | Materials | Grid | Voxels |
|---|---|---|---|---|
| LF9 | Circular | Air, Skin, SAT, Muscle, Fat, Bone, Nerve | 80x238x239 = 4.551 MCells | Topological Voxeler |
| LF10 | 8-Figure | Air, Skin, SAT, Muscle, Fat, Bone, Nerve | 80x224x270 = 4.838 MCells | Topological Voxeler |

Table 3.5: Specifications for the simulations used to study the interaction of the Circular and 8-Figure coils with the Multi-layered model.

### 3.4.2 The effect of the pulse's frequency

In order to study the effect of the frequency of the pulse in this Multi-layered model three stimulations using the Circular coil were done. Three different frequencies were used to proceed this study, the frequencies were 25, 250 and 2500 Hz (Table 3.6). The physical

model (Figure 3.12a) and the grid used are the same as in the simulation LF9. This study is a proof of concept, the frequency of the pulse can't be changed in reality, but this simulations are important to ensure that the solver is in agreement with the Faraday's law.

Table 3.6: Specifications of each of the simulations.

| Experiment | Frequency (Hz) | Materials | Grid | Voxels |
|---|---|---|---|---|
| LF-25 | 25 | Air, Skin, SAT, Muscle, Fat, Bone, Nerve | 80x238x239 = 4.551 MCell | Topological Voxeler |
| LF-250 | 250 | Air, Skin, SAT, Muscle, Fat, Bone, Nerve | 80x238x239 = 4.551 MCell | Topological Voxeler |
| LF-2500 | 2500 | Air, Skin, SAT, Muscle, Fat, Bone, Nerve | 80x238x239 = 4.551 MCell | Topological Voxeler |

As it was mentioned before, the dielectric properties of the materials play an important role during the simulation. Its values for the diferent frequencies can be seen in Table 3.7 and they were taken from the IT'IS 3.1 database. As it is possible to see in this table, the value of $\sigma$ increases and the value of $\varepsilon_r$ decreases for higher frequencies.

Table 3.7: Dielectric properties of the materials for the three different frequencies that were used.

| Material | $\sigma$ (S/m) | $\varepsilon_r$ |
|---|---|---|
| Air | 0 | 1 |
| Skin | 0.0002 | 1135.98 |
| SAT | 0.0397765 | 1.47308e+06 |
| Muscle | 0.211123 | 2.33605e+07 |
| Fat | 0.0397765 | 1.47308e+06 |
| Bone | 0.0200483 | 18895.1 |
| Nerve | 0.0251848 | 5.58788e+06 |

(a) Dielectric properties for 25 Hz.

| Material | $\sigma$ (S/m) | $\varepsilon_r$ |
|---|---|---|
| Air | 0 | 1 |
| Skin | 0.000200005 | 1135.87 |
| SAT | 0.0408376 | 53779.7 |
| Muscle | 0.296339 | 2.71801e+06 |
| Fat | 0.0408376 | 53779.7 |
| Bone | 0.0200722 | 4549.45 |
| Nerve | 0.0282649 | 133154 |

(b) Dielectric properties for 250 Hz.

| Material | $\sigma$ (S/m) | $\varepsilon_r$ |
|---|---|---|
| Air | 0 | 1 |
| Skin | 0.000200338 | 1135.21 |
| SAT | 0.0424215 | 6425.32 |
| Muscle | 0.331585 | 124370 |
| Fat | 0.0424215 | 6425.32 |
| Bone | 0.0202637 | 1435.18 |
| Nerve | 0.0305804 | 59931.2 |

(c) Dielectric properties for 2500 Hz.

### 3.4.3 The effect of the properties of the biological tissue

The importance of the dielectric properties for the calculus of the E-field and J is going to be studied in this section. The B-field doesn't vary while interacting with the human body because the magnetic permeability of the human body is equal to vaccuum. Due to this, the dielectric properties that are going to play an important role in the E-field created inside the body are the electric conductivity ($\sigma$) and the electric permittivity ($\varepsilon$).

The simulations that were done are summarized in the Table 3.8. The standard and LF databases were used in the simulations. As it is possible to see in the Table 3.9b, the value of $\varepsilon_r$ is equal to 1 in this database for all the materials so, in order to study the effect of this parameter, a third simulation with the values of $\sigma$ from the LF database and the $\varepsilon_r$ from the standard database was done. The physical model used (Figure 3.12a) and the grid of the simulation are the same as in the LF9.

Table 3.8: Specifications of each of the simulations. The frequency used for all the simulations was 2500 Hz, the materials are the ones that constitute the Multi-layered model and its properties that are taken from each of the databases that appear after the name of the materials and the grid was constructed in the same way as in the study of the effect of the frequency.

| Name | Materials and Properties of materials | Grid | Voxels |
|---|---|---|---|
| LF-G | Air, Skin, SAT, Muscle, Fat, Bone, Nerve - Standard | 80x238x239 = 4.551 MCell | Topological Voxeler |
| LF-LF | Air, Skin, SAT, Muscle, Fat, Bone, Nerve - Low Frequency | 80x238x239 = 4.551 MCell | Topological Voxeler |
| LF-LF+G | Air, Skin, SAT, Muscle, Fat, Bone, Nerve - $\sigma$: Low Frequandy, $\varepsilon_r$: Standard | 80x238x239 = 4.551 MCell | Topological Voxeler |

| Material | $\sigma$ (S/m) | $\varepsilon_r$ |
|---|---|---|
| Air | 0 | 1 |
| Skin | 0.000200338 | 1135.21 |
| SAT | 0.0424215 | 6425.32 |
| Muscle | 0.331585 | 124370 |
| Fat | 0.0424215 | 6425.32 |
| Bone | 0.0202637 | 1435.18 |
| Nerve | 0.0305804 | 59931.2 |

(a) Dielectric properties from standard database used in LF-G.

| Material | $\sigma$ (S/m) | $\varepsilon_r$ |
|---|---|---|
| Air | 0 | 1 |
| Skin | 0.17 | 1 |
| SAT | 0.0573412 | 1 |
| Muscle | 0.355287 | 1 |
| Fat | 0.0573412 | 1 |
| Bone | 0.00350399 | 1 |
| Nerve | 0.265076 | 1 |

(b) Dielectric properties from LF database used in LF-LF.

| Material | $\sigma$ (S/m) | $\varepsilon_r$ |
|---|---|---|
| Air | 0 | 1 |
| Skin | 0.17 | 1135.21 |
| SAT | 0.0573412 | 6425.32 |
| Muscle | 0.355287 | 124370 |
| Fat | 0.0573412 | 6425.32 |
| Bone | 0.00350399 | 1435.18 |
| Nerve | 0.265076 | 59931.2 |

(c) The values of $\sigma$ are taken from LF database and the values of $\varepsilon_r$ are taken from standard database and they were used for LF.

Table 3.9: The dielectric properties shown in the two first tables are from standard and LF databases. The last table contains the $\sigma$ from the LF database and the $\varepsilon_r$ from the standard database.

## 3.5 Human model

Finally, human body models with different dielectric properties were used to calculate the electromagnetic field distribution created by the stimulation of different coils.

The stimulations were done on the spinal cord at T12 level and in the nerve roots at L5 level, in the area that involves the nerves that supply innervation to the gastronemius, soleus and tibialis anteriors mucles.

The Common peroneal nerve (L4-S1) branches into the deep peroneal nerve which supplies the tibialis anterior, which is responsible for the foot dorsiflexion and inversion. The tibial nerve (L4-S2) supplies innervation to the gastrocnemius and soleus muscles which is responsible for the main plantar flexion of the foot [85]. These muscles were selected because they are relevant for the study of the reflex pathways described in the theoretical concepts. Due to this, the coil was placed centered in T12 and L5. At T12 level, it is aimed to stimulate the circuitry of interneurons. At L5 level, it is expected to stimulate the afferent and efferent neurons that innervate the muscles of interest.

The models used to do the simulation of the stimulation of the spinal cord and the roots with the Circular coil and 8-Figure coil can be seen in Figure 3.13. In both cases, the fields were measured in the volume that involves the Wire Box (583x470x624) shown in

the Figures. Furthermore, the Voxels were constructed based on the Topological Voxeler. In Table 3.10 the simulations that were done are shown.

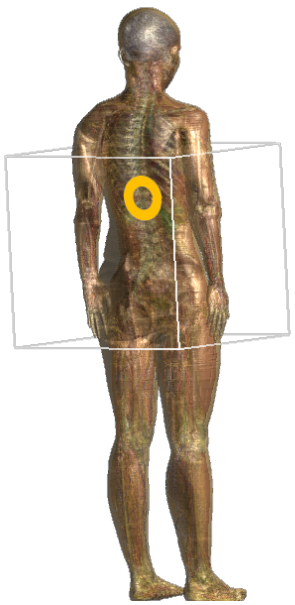

(a) Model of the magnetic stimulation at the spinal cord level with the circular coil.

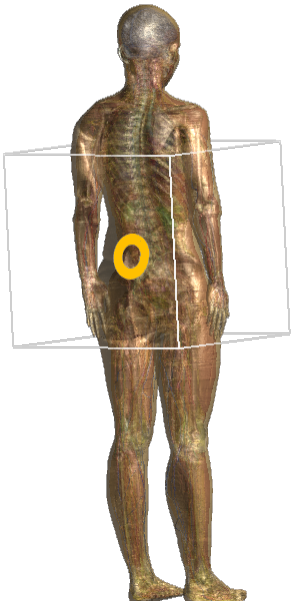

(b) Model of the magnetic stimulation at the roots with the circular coil.

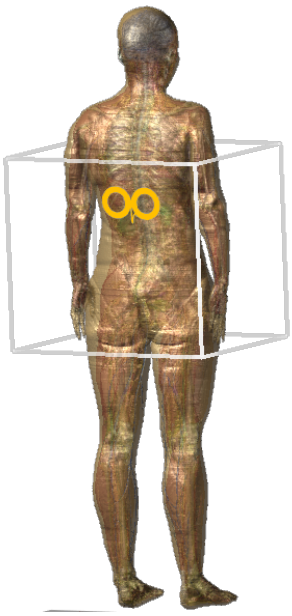

(c) Model of the magnetic stimulation at the spinal cord level with the 8-Figure coil.

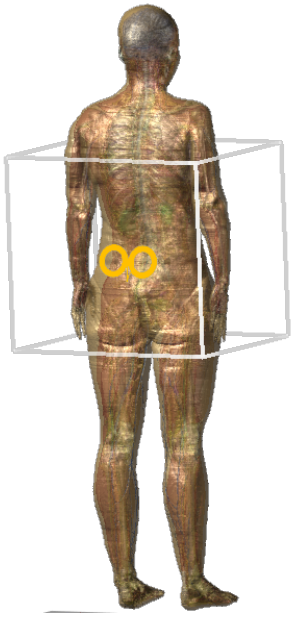

(d) Model of the magnetic stimulation at the roots with the 8-Figure coil.

Figure 3.13: Models used for the simulation of the magnetic stimulation with the Circular and 8-Figure coils.

In the next section the results obtained in all the simulations are shown. It is important

Table 3.10: Specifications of the simulations with the circular coil at the spinal cord level.

| Name | Coil | Stimulation Cite | Database | Grid |
|---|---|---|---|---|
| Ella-C-SC-G | Circular | Spinal Cord | IT'IS 3.1 database | 387x555x542 = 116.413 MCell |
| Ella-C-SC-LF | Circular | Spinal Cord | IT'IS LF 3.1 database | 387x555x542 = 116.413 MCell |
| Ella-C-SC-LF+G | Circular | Spinal Cord | $\sigma$: IT'IS 3.1 LF database, $\varepsilon$: IT'IS 3.1 database | 387x555x542 = 116.413 MCell |
| Ella-C-R-G | Circular | Nerve Roots | IT'IS 3.1 database | 388x554x544 = 116.504 MCell |
| Ella-C-R-LF | Circular | Nerve Roots | IT'IS 3.1 LF database | 388x554x544 = 116.934 MCell |
| Ella-C-R-LF+G | Circular | Nerve Roots | $\sigma$: IT'IS 3.1 LF database, $\varepsilon$: IT'IS 3.1 database | 388x554x544 = 116.504 MCell |
| Ella-DC-SC-G | 8-Figure | Spinal Cord | IT'IS 3.1 database | 385x553x540 = 114.969 MCell |
| Ella-DC-SC-LF | 8-Figure | Spinal cord | IT'IS 3.1 LF database | 385x553x540 = 114.969 MCell |
| Ella-DC-SC-LF+G | 8-Figure | Spinal cord | $\sigma$: IT'IS 3.1 LF database, $\varepsilon$: IT'IS 3.1 database | 385x553x540 = 114.969 MCell |
| Ella-DC-R-G | 8-Figure | Nerve roots | IT'IS 3.1 database | 386x553x541 = 115.481 MCell |
| Ella-DC-R-LF | 8-Figure | Nerve roots | IT'IS 3.1 LF database | 386x553x541 = 115.481 MCell |
| Ella-DC-R-LF+G | 8-Figure | Nerve roots | $\sigma$: IT'IS 3.1 LF database, $\varepsilon$: IT'IS 3.1 database | 386x553x541 = 115.481 MCell |

to mention that the fields that are calculated are sinusoidal. The intensities that are shown in all the images correspond to the maximum value of each field or sinusoidal wave.

CHAPTER 4

# Results

## 4.1 Characterization of the stimulation devices

The characterization of the stimulation devices is the first step to calculate appropriately the field distribution after magnetic stimulation (MS). As it was mentioned in the previous chapter, the characteristics that are evaluated are the B-field, the E-field and inductance. The B-field and inductance were calculated in air and the E-field in skin.

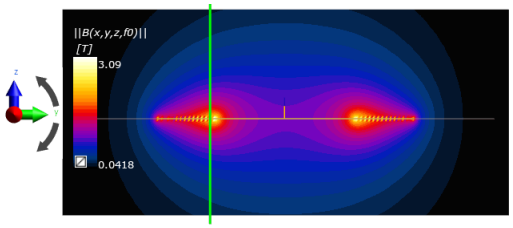


(a) The B-field of a circular coil in LF1 ($B_{max}$=3,09 T).

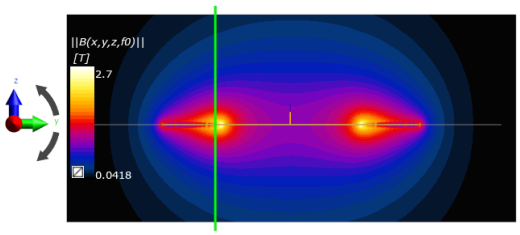


(b) The B-field of a 8-Figure coil in LF2 ($B_{max}$=2,7 T).

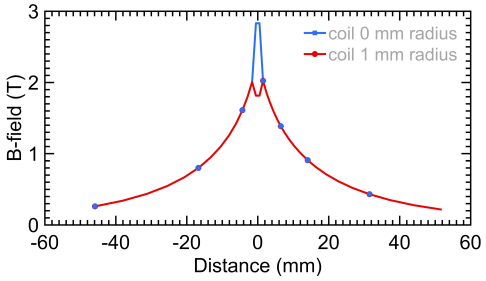


(c) The B-field along the green line (along Z and at Y=38) for both coils.

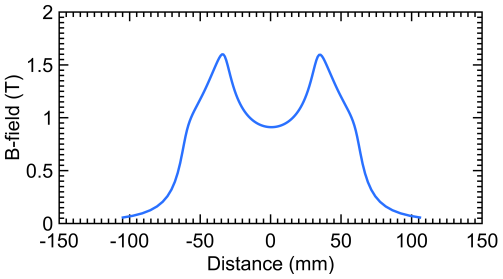


(d) The B-field 2 mm from the surface of the coil.

Figure 4.1: B-field distribution for a circular coil without and with copper as material on the plane XZ and the slice index 73 is shown. In both graphs, the distance 0 mm corresponds to the center of the coil.

The characteristics that needed to be estimated, were simulated for an ideal coil, without a material, and for a realistic coil made of copper and with an associated thickness. If the results indicate that the approximation is valid, it is possible to use the simplification of a current path to modulate the stimulation coils.

The results for the simulations in air for the Circular coil are shown in Figure 4.1. As it can be seen in Figure 4.1c the results obtained for an ideal and a realistic coil are similar. The B-field distribution at the surface of the coils (Figure 4.1d) is close from the distribution measured by Magstim (Figure 3.7b). The magnetic energy is 272.303 J and the inductance is 23.63 $\mu$H for the coil with 0 mm of radius and the coil of 1 mm of radius had a 260.931 J of magnetic energy and 22.65 $\mu$H of inductance. This values of conductance are really close from the reference values (Table 3.1).

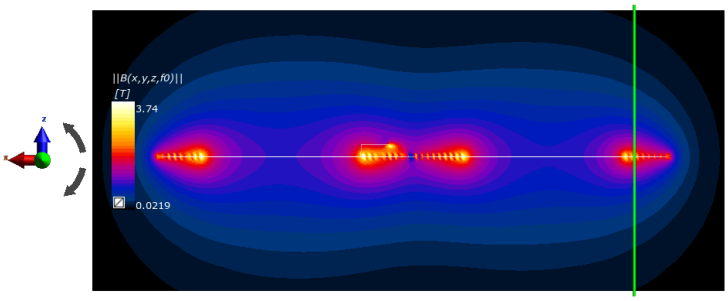


(a) The B-field distribution of an ideal 8-Figure coil in LF3 (B=3,74 T).

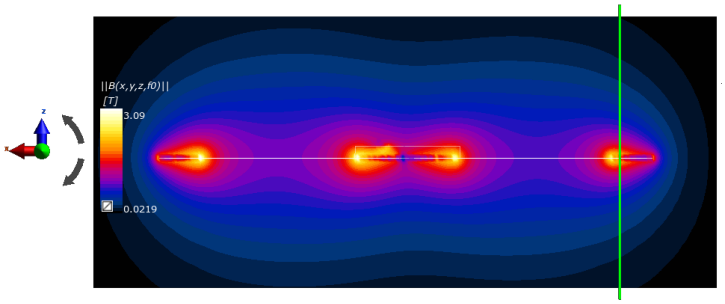


(b) The B-field distribution of a realistic 8-Figure coil in LF4 (B=3,09 T).

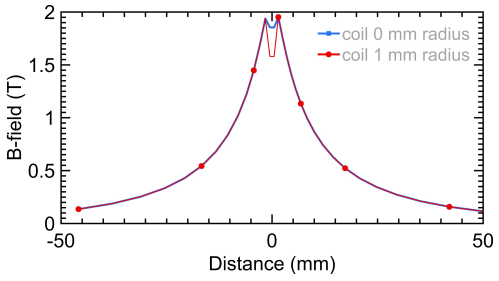


(c) The comparison of the B-field distribution through the green line for both coils.

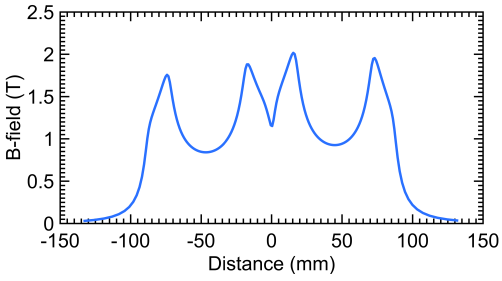


(d) The B-field distribution at the surface of the coil.

Figure 4.2: B-field distribution for the coils on the plane XZ, at slice index 61, the comparison between the two coils is done in (C) and in (D) the B-field distribution at the surface of both coils is shown.

The same procedure was done to characterize the 8-Figure coil. In Figure 4.2, it is possible to see the results. As it is shown in Figure 4.2c, there is no significant change on the B-field due to the use of a realistic coil. Additionally, the distribution of the B-field at the surface of the coils is the same and close from the measurements done by Magstim (Figure 3.7d). For an ideal coil the magnetic energy is 257.438 J and the inductance is 16.42 $\mu$H. Instead, the magnetic energy is 243.086 J and the inductance is 15.5 $\mu$H for a realistic coil. These values are as well close from the reference values showed in Table 3.1.

The E-field created by the circular coil in skin is shown in Figure 4.3. The E-field distribution in the skin with a realist and a ideal revealed similar results. Furthermore, the distribution of the field at the surface of the coil can be seen in Figure 4.3b. This results are in agreement with the values measured in a saline solution by Magstim (Figure 3.7a).

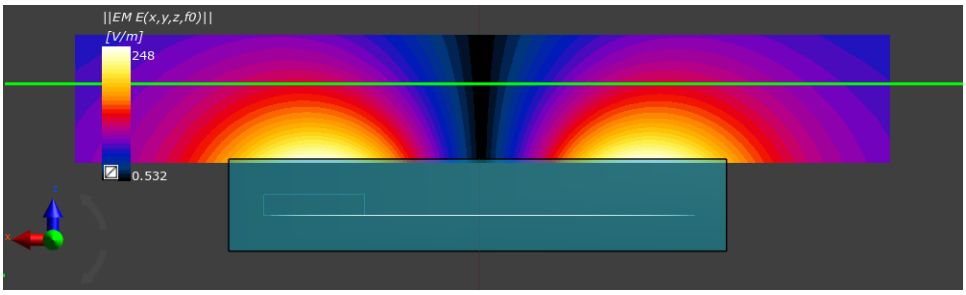


(a) The E-field created in skin by the ideal and realistic coils in LF5 and LF6.

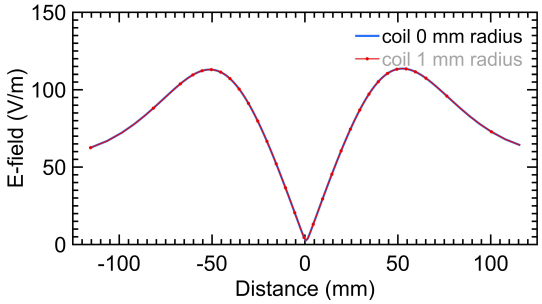


(b) The E-field along the green line 37 mm from the coil, shown in the previous Figures.

Figure 4.3: E-field distribution created by the circular coil on the plan YZ at slice index 81 and comparison of the E-field distribution for both coils. These are t

Lastly, the E-field of the 8-Figure coil was calculated and its results are shown in Figure 4.4. The E-field distribution created by the current path is the same as the one created by the realistic coil. This is evidenced in Figure 4.4b. The intensity of the E-field calculated is also close to the values measured experimentally by Magstim (See Figure 3.7c).

In Table 4.1 it is possible to see the comparison of the results obtained for the two ideal coil and the values measured by Magstim. These results show that the values of inductance, B-field and E-field are very close from the values measured by the company.

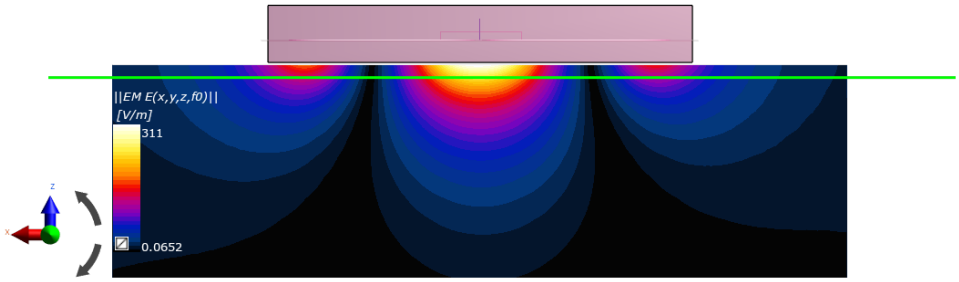


(a) The E-field created in skin by the ideal and realistic 8-Figure coil in LF7 and LF8.

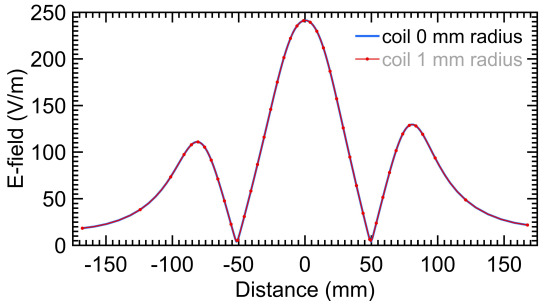


(b) The E-field distribution along the green line shown in (A) and (B).

Figure 4.4: E-field distribution for the 8-Figure coil on the plan XZ at slice index 64.

The results also indicate that both the Circular coil and the 8-Figure coil can be approximated to a current path. More important than this, the results show that the coils were appropriately modelled, since their inductance, B-field and E-field are closed from the values measured. Thus, these models can be used for the following simulations.

Table 4.1: Comparison of the results with the values of reference. $I_{ref}$, $B_{max,ref}$, $E_{max,ref}$ are the values of reference for the inductance, magnetic field peak and electric field peak. $I_{mes}$, $B_{max,mes}$ and $E_{max,mes}$ are the values obtained through the simulations with the ideal coil.

| Coil | $I_{ref}$ ($\mu$H) | $I_{mes}$ ($\mu$H) | $B_{max,ref}$ (T) | $B_{max,mes}$ (T) | $E_{max,ref}$ (V/m) | $E_{max,mes}$ (V/m) |
|---|---|---|---|---|---|---|
| Single 90 mm | 23,47 | 23,63 | 2 | 2 | 120 | 120 |
| Double 70 mm | 15,5 | 16,42 | $\geq$ 0,92 | 2 | 230 | 240 |

## 4.2 Multi-layered model

In this section the E-field and the electric current density (J) generated by the two coils while interacting with the Multi-layered model are analysed. The Multi-layered model was described in Chapter 3 (Figure 3.11). This model can be used to predict the effects of electromagnetic fields inside the human body by using a simplified human body

model. The parameters that are studied take into consideration the stimulation device and the dielectric properties of the biological tissue. The two stimulation coils previously described are used to study the field distribution in the Multi-layered model. The effect of the frequency of the pulse is used to ensure the validity of the solver. The study of the dielectric properties of the biological tissue is done by using two different databases. The results of each study are the E-field and J distribution, because they are important parameters to predict neuronal stimulation.

### 4.2.1 The effect of the stimulation coil

The Circular and 8-Figure coils were placed at the same distance from the Multi-layered model. In Figure 4.5, the E-field and J distribution created in the Multi-layered model with the circular coil are shown. Figure 4.5c evidences the expected exponential decay of the E-field. Additionally, it is evident that the tissue that is stimulated the most is the muscle in Figure 4.5d, which is due to its high electric conductivity.

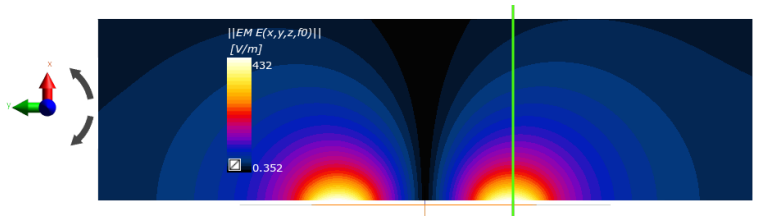


(a) The E-field of the circular coil in the Multi-layered model in the Plane XY in the Slice Index 119 ($E_{max}$=432 V/m).

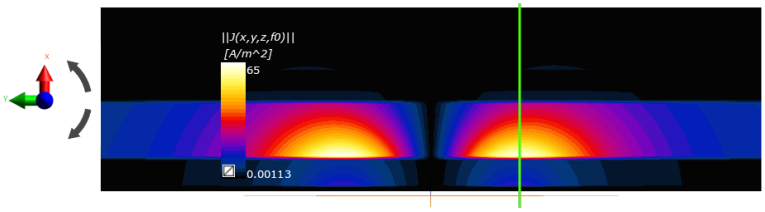


(b) The current density distribution (J) ($J_{max}$=65 A/m$^2$).

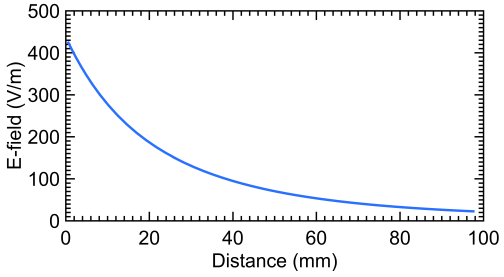


(c) The E-field distribution through the green line in (a).

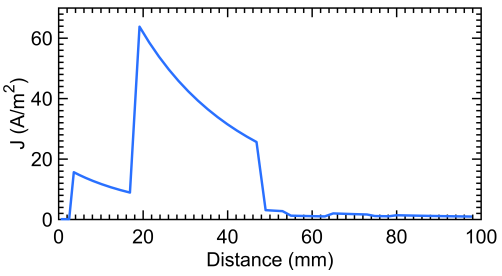


(d) The J distribution through the green line in (b).

Figure 4.5: The E-field and J distribution of the circular coil interacting in the Multi-layered model.

In the same way, Figure 4.6 shows the E-field and J distribution in the Multi-layered model created by the 8-Figure coil. The green lines in all the images were placed where the

field intensities are higher for both cases and the E-field and J intensities were measured through out this lines.

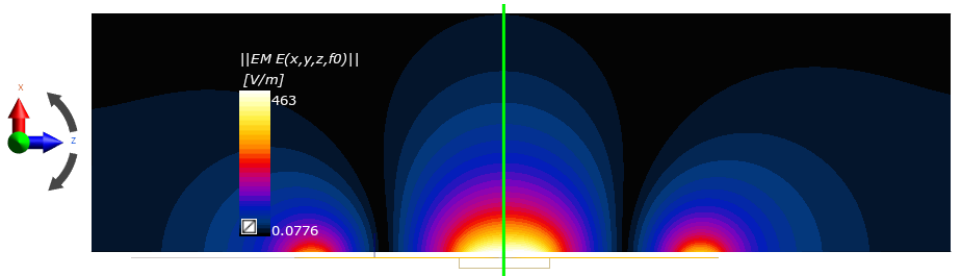


(a) The E-field distribution ($E_{max}$=463 V/m).

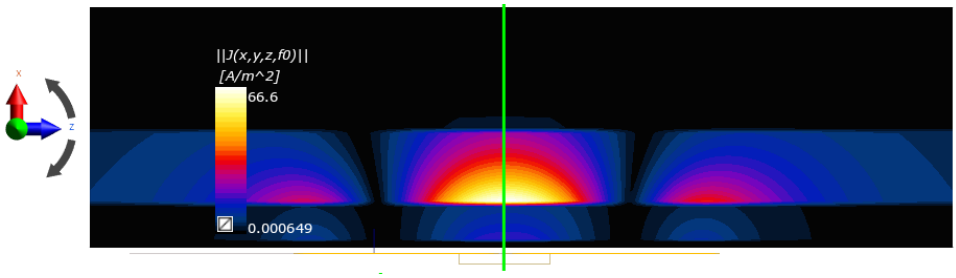


(b) The J distribution ($J_{max}$=66,6 A/m$^2$).

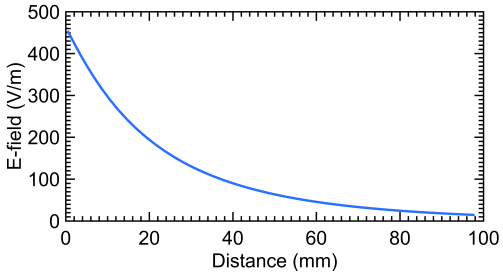


(c) The EF distribution along the green line in (a).

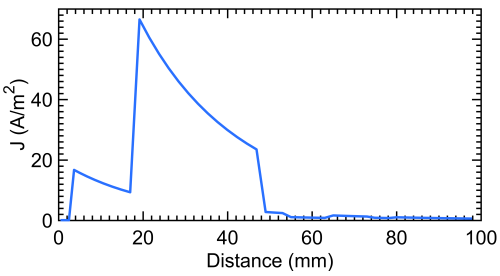


(d) The J distribution along the green line in (b)).

Figure 4.6: The E-field and J distribution created by the 8-Figure coil in the Multi-layered model on the Plane XZ at Slice index 106. The green lines are both located along the direction X at Z=131.

The E-field and J distribution created by the Circular and 8-Figure coil in the nerve layer can be seen in Figure 4.7. In this Figure the field distribution in the Nerve layer is shown and it is very interesting because it allows understanding the main effects of the stimulation done with these two coils. In Figure 4.7a, the E-field distribution created by the circular coil is not the one expected. It is known that the volume of higher intensity of the field is around the perimeter of the coil. This might mean that the distance between the coil and the nerve layer is too big to get the correct distribution of the field. In any case, as we can see in Figure 4.7a, the E-field distribution is very wide while comparing with the E-field created by the 8-Figure coil (see Figure 4.7b) and the same conclusion can be extracted from the J distribution. This result is very significant since it shows that the volume of stimulation when using the Circular coil is much larger than with the 8-Figure

coil. Another thing that is shown is that this Circular coil can penetrate deeper regions than this 8-Figure coil, as it can be seen with its higher intensity of E-field distribution in the nerve's layer. This confirms the importance of the coil's diameter, as it was mentioned in Chapter 2. The smaller diameter of the coil makes the intensity of the E-field higher at the surface of the coil (see Figure 4.6c) and also a more accentuated decay of the field, which leads to a lower intensity of the E-field in the nerve layer for the 8-Figure coil (see Figure 4.7b).

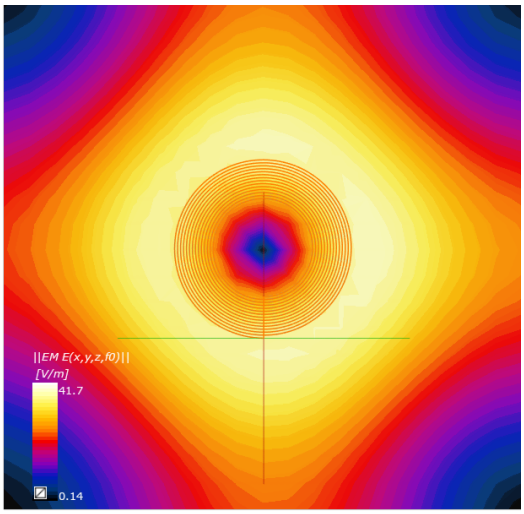


(a) The E-field distribution created by the Circular coil ($E_{max}$=41.7 V/m).

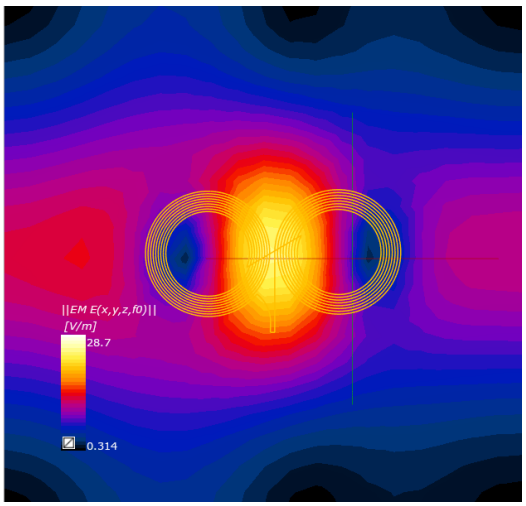


(b) The E-field distribution created by the 8-Figure coil ($E_{max}$=28.7 V/m).

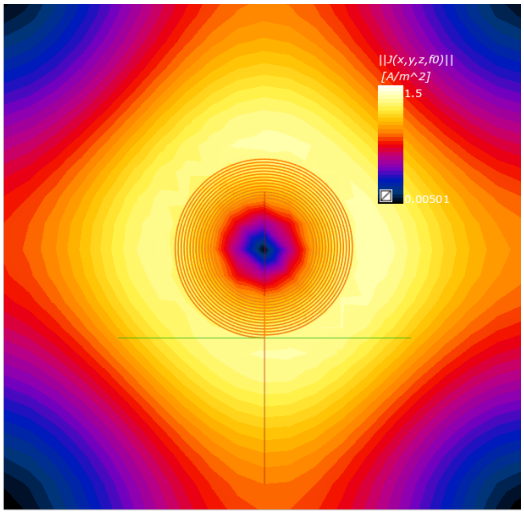


(c) The J distribution created by the Circular coil ($J_{max}$=1.5 A/m$^2$).

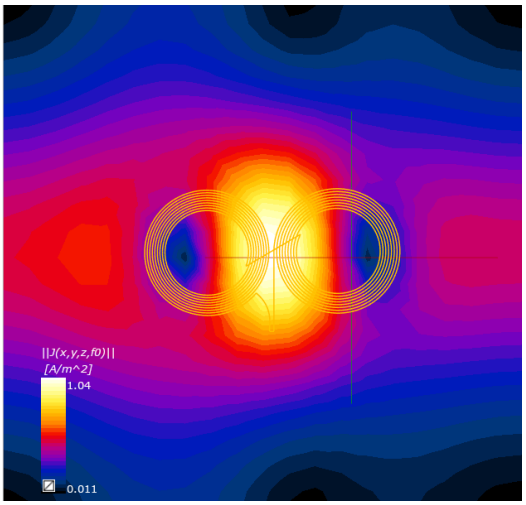


(d) The J distribution created by the 8-Figure coil ($J_{max}$=1.04 A/m$^2$).

Figure 4.7: The E-field and J distribution in the Nerve layer created by both coils.

### 4.2.2 The effect of pulse's frequency

Three different frequencies were used to study the effects of the frequency of the pulse in the E-field and J generated in the Multi-layered model. As it was mentioned in Chapter

3, this is a proof of concept to see if the solver is calculating the field distribution in agreement with Faraday's law. The results of the E-field distribution in the Multi-layered for the three frequencies are shown in Figure 4.8. It is shown that from the frequency of 25 Hz to the frequency of 250 Hz, the E-field increases ten times and the same happens with 250 Hz and 2500 Hz. Hence, the results show linearity and are in agreement with Faraday's law. In Figure 4.9 this linearity is also evident in the nerve layer.

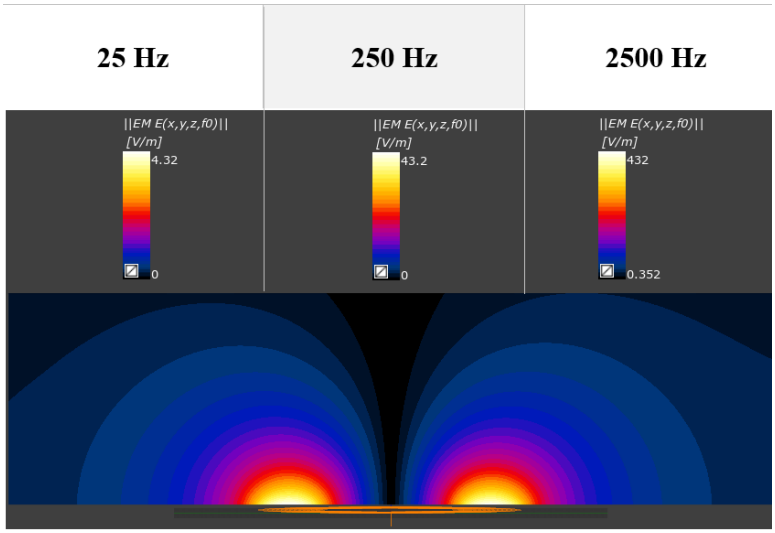


Figure 4.8: The E-field distribution in the Plane XY Slice Index 119 and intensity for each of the frequencies used for the input signal: 25 Hz (LF-25), 250 Hz (LF-250) and 2500 Hz (LF-2500).

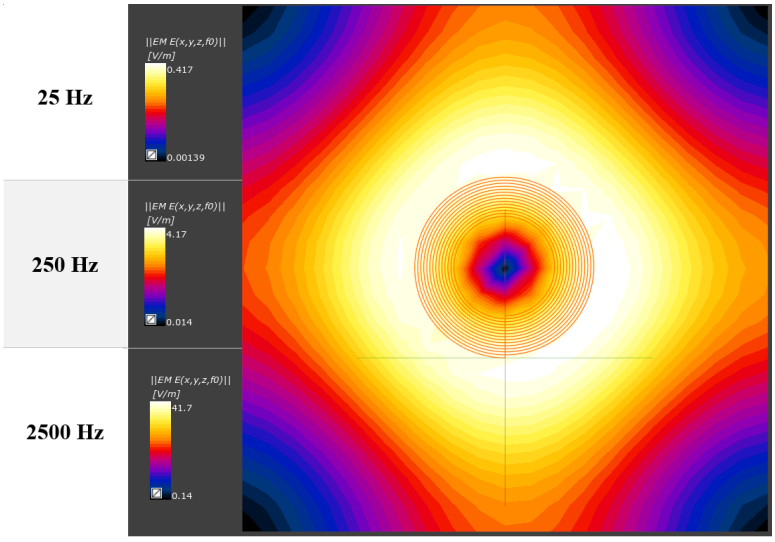


Figure 4.9: The E-field distribution for the frequencies 25 Hz (LF-25), 250 Hz (LF-250) and 2500 Hz (LF-2500) in the Nerve Layer.

These results are important again to show that the solver used by the software is calculating the E-field as expected. Although, it is not possible to change the frequency

of the pulse of the stimulator, this might be an important parameter of stimulation that should be further studied in order to achieve a more precise stimulation.

### 4.2.3 Effect of the properties of the biological tissue

As it was previously mentioned, the dielectric properties of the biological tissue play an important role in the distribution of the E-field and J. Thus, the changes in the field intensity were studied with dielectric properties from different databases. First, by using the standard database the E-field and J distributions were calculated. Then, the same was repeated with the LF database. Since the $\varepsilon_r$ is 1 in LF database, we also studied the effect of changing the $\varepsilon_r$, by using the values from the standard database. This last test, as it will be shown afterwards, wasn't necessary since it is known that for this range of frequencies the impact of the displacement current is very low and $\sigma$ is the property used to calculate the field distribution.

The E-field generated in the Multi-layered model with all the databases gave rise to the same distribution, which can be seen in Figure 4.10. The Figure 4.10b shows that the E-field intensity decays with distance and in the same way in the same simulations done. The E-field distribution does not vary with the use of different databases because there is no charge accumulation in the interfaces, since the current path is parallel to each interface. Thus, the E-field is created by electromagnetic induction and the vector potential $\vec{A}$ through the Biot Savart's law (Equation 2.29).

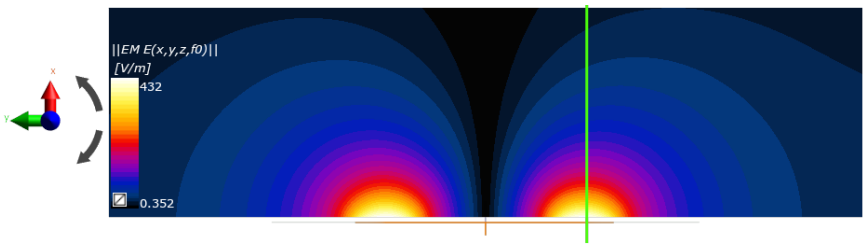


(a) The E-field in the Multi-layered model for LF-G, LF-LF and LF-LF+G.

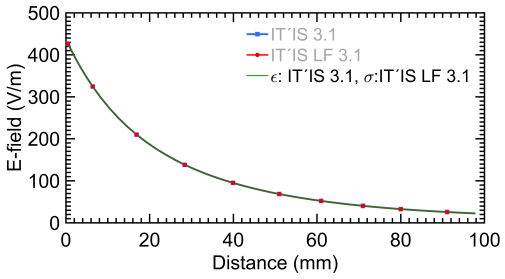


(b) The E-field distribution for all the coils the green line.

Figure 4.10: The E-field distribution of the circular coil interacting in the Multi-layered model in the Plane XY in the Slice Index 119. As it is seen in (b) the distribution is the same using different dielectric properties.

In Figure 4.11, it is shown the J distribution in all the simulations as well as the

comparison between them. The main difference that can be pointed out is that due to the different $\sigma$ of the skin, the J is much higher in the simulations where the $\sigma$ is from the LF database. Furthermore, the layer of the nerve situated between the 74 mm and 79 mm has a higher J due to the same reason as the skin. These results also show that the muscle is the most stimulated tissue during the magnetic stimulation.

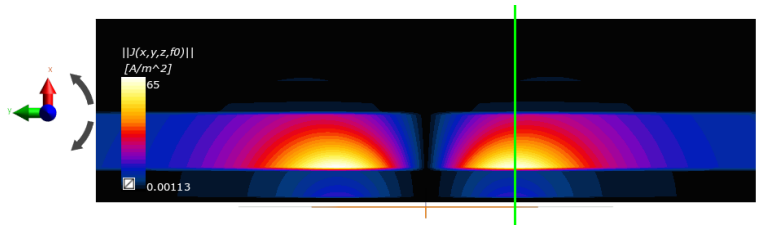


(a) The J(x,y,z) distribution LF-G.

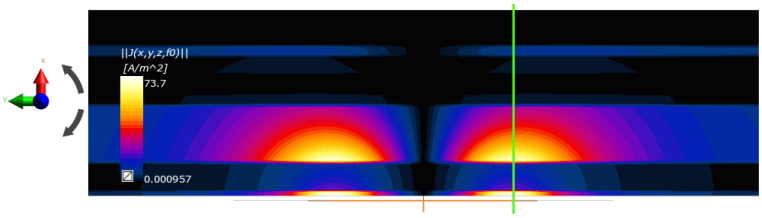


(b) The J(x,y,z) distribution in LF-LF and LF-LF+G.

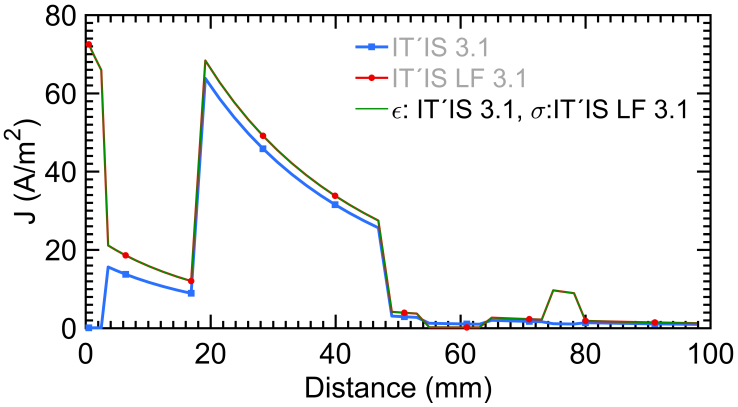


(c) The comparison of the J distribution between the different simulations.

Figure 4.11: The J(x,y,z) distribution in the Multi-layered model in the Plane XY in the Slice Index 119 created by the circular coil, using for three different simulations, different dielectric properties.

The E-Field and J distribution in the Nerve Layer is shown in Figure 4.12. It is evident that the differences in the E-field are very low between the three simulations, but the J intensity is much lower in the simulation where the dielectric properties were taken from the standard database.

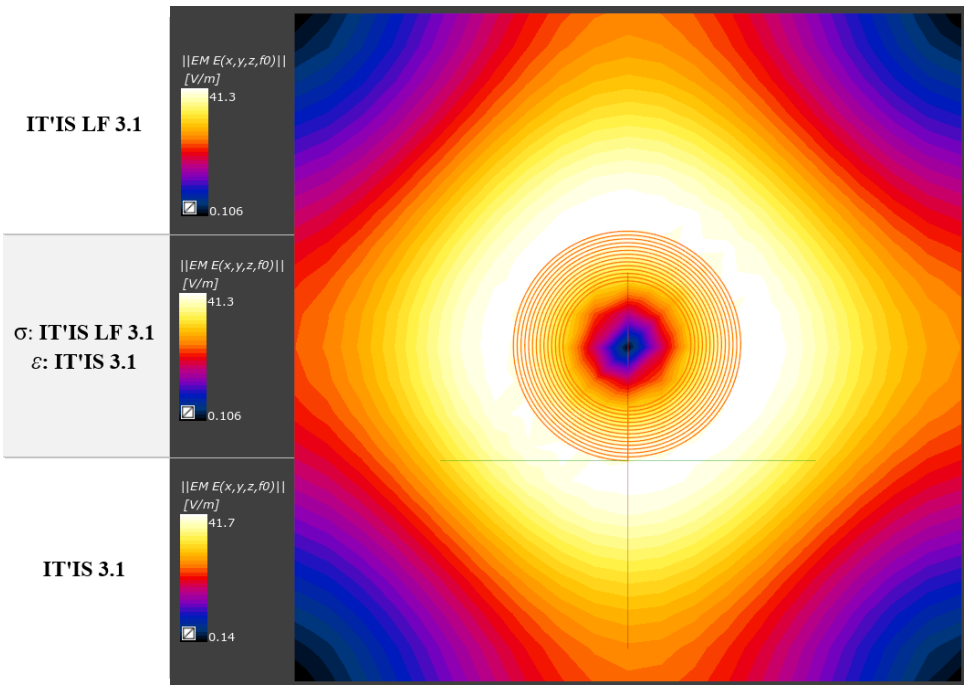


(a) The E-field distribution.

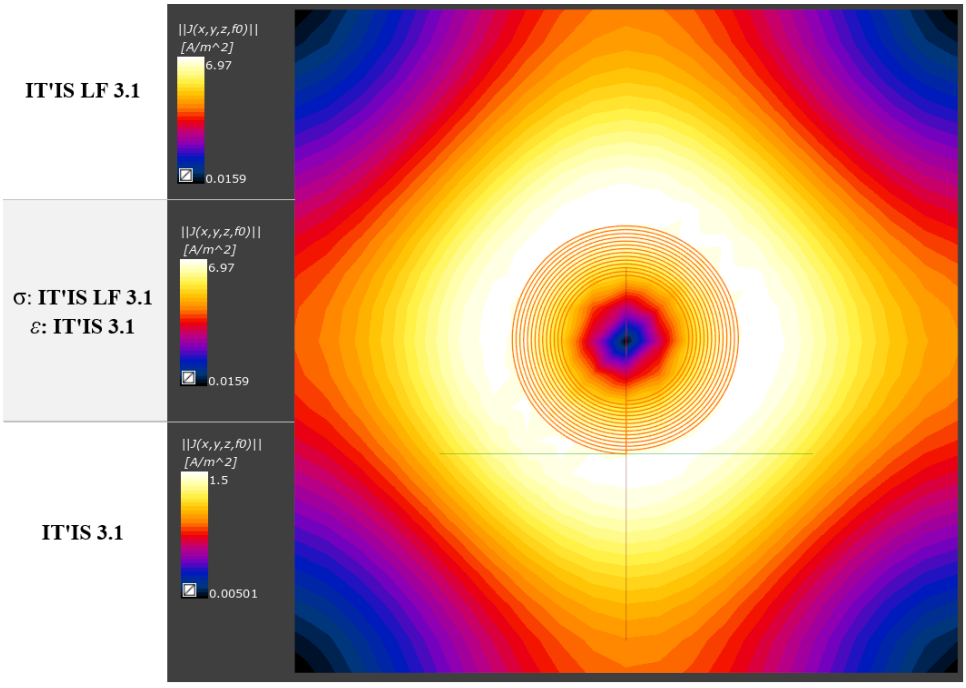


(b) The J distribution.

Figure 4.12: The E-field and J distribution and intensities in the Nerve layer obtained for the different dielectric properties used in the simulations.

The main results that can be deduced from the study of the MS in the Multi-layered model are:

- The shape of the coil used for the stimulation is very important: the circular coil makes a wider volume to be stimulated while the 8-Figure stimulates a more focused

volume;

- The diameter is pertinent to perceive the stimulation of deeper neuronal structures;
- Different $\sigma$ induce changes in the field intensity. The relevance of these changes needs to be further studied to understand if they lead to a wrong prediction of the structures that are stimulated.

The Multi-layered model is a simplistic model of the human body. It is important to study in a simplistic way the effect of electromagnetic fields in the human body to understand the basic phenomena of the stimulation. Nevertheless, the complex geometry of the human body play an important role, as it was mentioned before. The distance at which the neurons are from the stimulation device varies along the trunk and they can be in the spinal cord or in the nerve roots.

The parametrization of the Multi-layered model could give a better insight about all the possible configurations of tissue distribution. In this way, it would be possible to predict the neurons that might undergo stimulation in different parts of the trunk. This parametrization would comprehend the change of the thickness of each layer to mimic the different levels that are stimulated. The amount of simulations might increase a lot in case we consider all the possible cases and its analysis might become very complex. That's the reason why it is difficult to use the Multi-layered model to predict which spinal neuronal networks are excited during stimulation, through all the trunk. In the following section, the results of MS in the human model are shown.

An Heterogeneous model should be also used to study MS. In this way, the effect of charge accumulation at the interface between tissues of different conductivities could be studied. By Heterogeneous model it is meant the presence of tissues where the current induced in the medium is perpendicular to the surface between different tissues.

## 4.3 Human model

In this section the study of spinal cord stimulation with two magnetic coils is done in a realistic human model. The main goal is to study the electromagnetic field distribution inside a realistic human model. For that purpose a model of a 24 years old woman is used. The effect of the use of different databases of dielectric properties, the use of different coils and the positioning of them in the field distribution is studied.

The first set of simulations was done at T12 level with the Circular coil. The dielectric properties used lead to three simulations: Ella-C-SC-G, Ella-C-SC-LF and Ella-C-SCLF+G as it is shown in Table 3.10.

The E-field distribution on a sagittal plane of the trunk, in the spinal cord and nerve roots can be seen for all the three simulations can be seen in Figure 4.13. As it is shown, the results obtained in the E-field distribution diverge when the dielectric properties of the materials are from the standard database, while comparing with the other simulations. It

also shows the irregularities in the E-field intensity since it does not have an homogeneous decay with distance, as it was shown with the Multi-layered model (see Figure 4.5c). The Human body is an extremely heterogeneous medium, so there is the effect of charge accumulation in the interface between tissues of different conductivities. The Figure 4.13c and Figure 4.14e show that the E-field distribution is higher in the nerve roots than in the spinal cord.

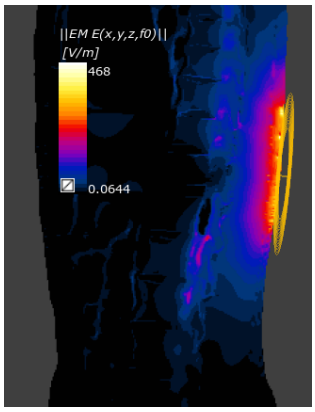


(a) The E-field calculated in Ella-C-SC-G (E-Field$_{max}$ = 468 V/m).

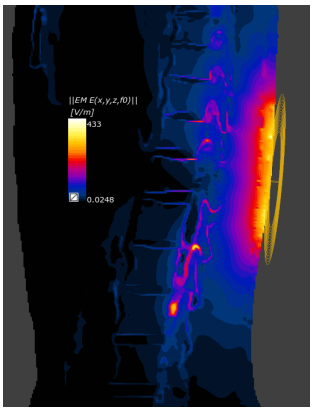


(b) The E-field calculated in Ella-C-SC-LF and in Ella-C-SC-LF+G (E-Field$_{max}$ = 433 V/m).

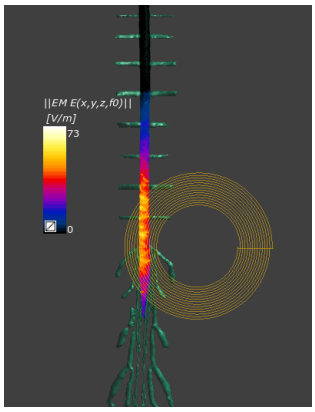


(c) The E-field in the spinal cord in Ella-C-SC-G (E-Field$_{max}$ = 73 V/m).

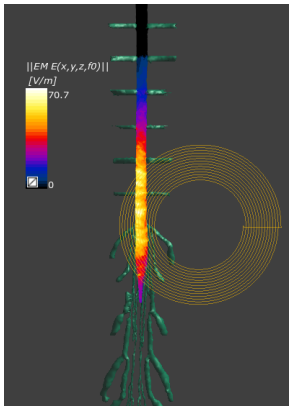


(d) The E-field in the spinal cord in Ella-C-SC-LF and Ella-C-SC-LF+G (E-Field$_{max}$ = 70.7 V/m).

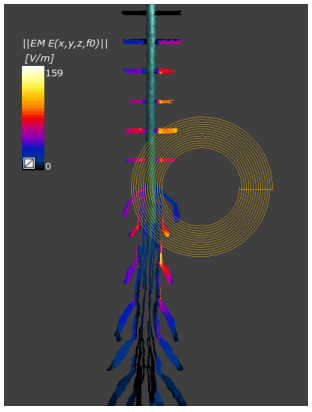


(e) The E-field generated in the nerves in Ella-C-SC-G (E-Field$_{max}$ = 159 V/m).

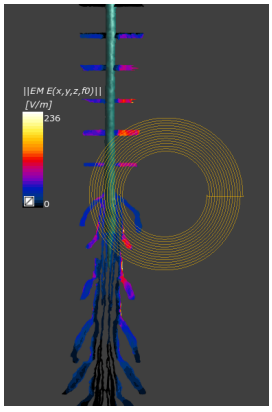


(f) The E-field in the nerves in Ella-C-SC-LF and Ella-C-SC-LF+G (E-Field$_{max}$ = 236 V/m).

Figure 4.13: The E-field distribution created by stimulation with the circular coil in the model Ella at spinal cord level. The sagital plane is located in Plane XZ in the Slice Index 263.

The J distribution is shown in Figure 4.14. The results reveal that the skin has a much higher J in the simulations where the $\sigma$ was taken from the LF database than in the simulation were the standard database is used (compare Figure 4.14a and Figure 4.14b). This result is straightforward because of Equation 2.20. Furthermore, we can see that the

muscle is the tissue with higher intensity of J, which can also be seen while stimulating with the magnetic coil in reality. Usually, during stimulation, the muscle gets contracted, which might cause discomfort to the person who is stimulated. The J intensity in the spinal cord and the nerve roots is very similar (see Figure 4.14c and Figure 4.14e).

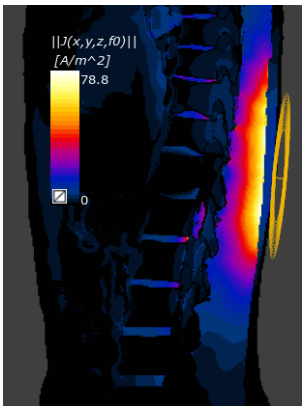


(a) The J calculated in Ella-C-SC-G ($J_{max}$ = 78,8 A/m$^2$).

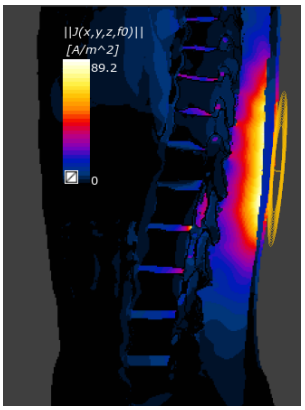


(b) The J calculated in Ella-C-SC-LF and Ella-C-SC-LF+G ($J_{max}$ = 89,2 A/m$^2$).

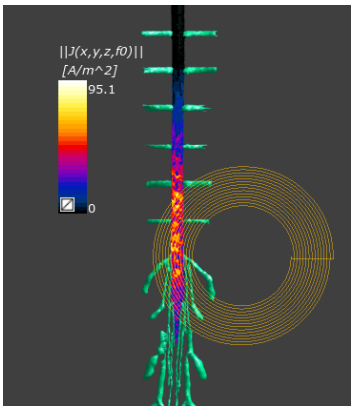


(c) The J created in the spinal cord in Ella-C-SC-G ($J_{max}$ = 95,1 A/m$^2$).

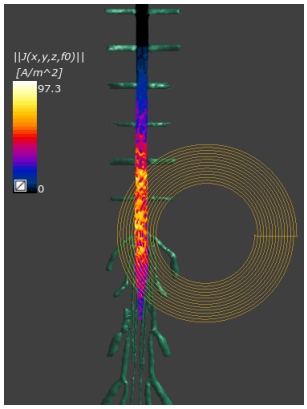


(d) The J in the spinal cord in Ella-C-SC-LF and Ella-C-SC-LF+G ($J_{max}$ = 97,3 A/m$^2$).

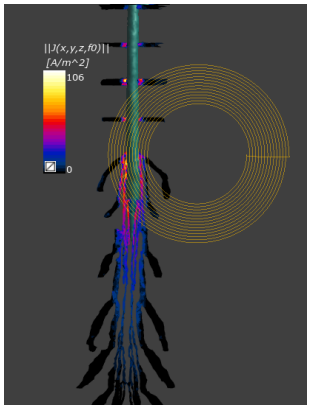


(e) The J in the nerves in Ella-C-SC-G ($J_{max}$ = 106 A/m$^2$).

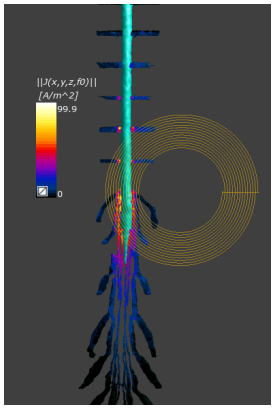


(f) The J in the nerves in Ella-C-SC-LF and Ella-C-SC-LF+G ($J_{max}$ = 99,9 A/m$^2$).

Figure 4.14: The J distribution in Ella created by the stimulation with the circular coil at the spinal cord level. The sagital plane is Plane XZ in the Slice Index 263.

Afterwards, simulations at L5 level were done. The simulation's name are Ella-C-R-G, Ella-C-R-LF and Ella-C-R-LF+G. In Figure 4.15 and in Figure 4.16 the E-field and J distributions are shown for all the simulations. The results obtained with the dielectric properties from LF database and the simulation where the $\sigma$ was taken from LF database and the $\varepsilon$ from the standard database have the same results in the simulations. If we compare these results with the previous ones, the E-field distribution varies again while using the standard database. The J in the skin is also higher when the $\sigma$ used is taken from the LF database, which means that the results are coherent. Furthermore, it is interesting

to see that the values of J are lower in the nerve roots but the E-field is around three times higher, than the E-field calculated at T12 level.

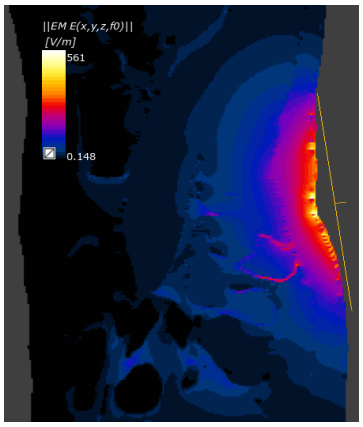


(a) The E-field in Ella-C-R-G on a sagital plane of Ella's model ($E_{max}$=561 V/m).

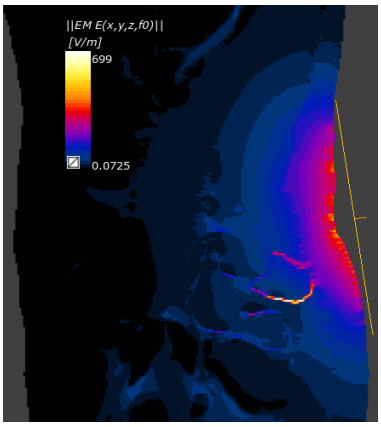


(b) The E-field in Ella-C-R-LF and Ella-C-R-LF+G ($E_{max}$=699 V/m).

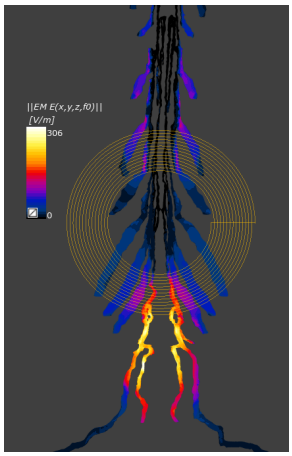


(c) The E-field generated in the nerves in Ella-C-R-G ($E_{max}$=306 V/m).

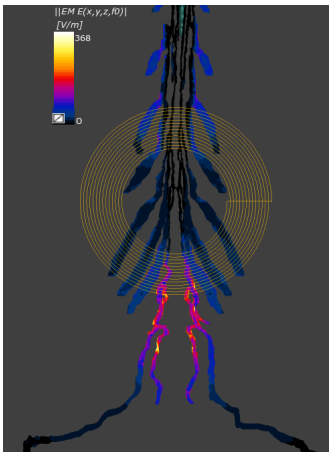


(d) The E-field generated in the nerves in Ella-C-R-LF and Ella-C-R-LF+G ($E_{max}$=368 V/m).

Figure 4.15: The E-field distribution created by a circular coil at the level of the roots in Ella model. The sagital plane is in Plane XZ in the Slice Index 229

If we take into consideration that the model that describes how the Eddy currents are created inside the body, this might be the reason why J is so low. As it was explained in Section 2.3, in an homogeneous media the currents inside the body are parallel to the coil and flow in the opposite direction than in the coil. Although the human model is not a homogeneous model, by doing this approximation, it can be predicted that the roots that are closer from the coil (the lower part of the roots where the E-field is higher - see Figure 4.15c) are perpendicular to the currents generated inside the body. This might be the reason why the J distribution is so low while there is such a high E-field. Other simulations should be done with this coil in different positions, in order to get the position

at which it would create a higher J.

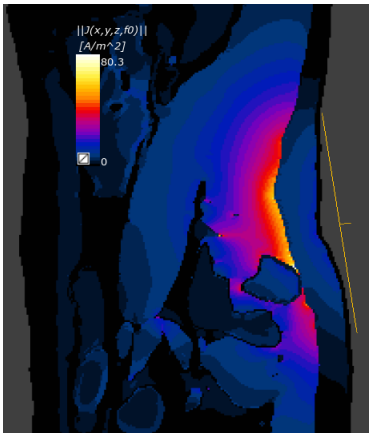


(a) The J generated in a sagital plane in Ella-C-R-G ($J_{max}$=80,3 A/m$^2$).

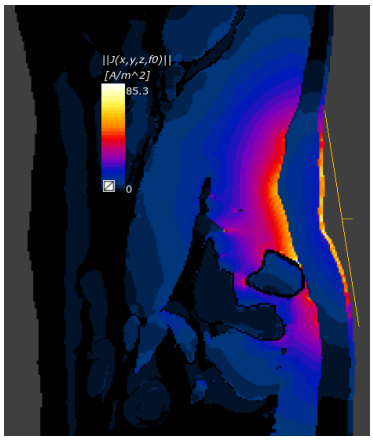


(b) The J generated in a sagital plane in Ella-C-R-LF and Ella-C-R-LF+G ($J_{max}$=85,3 A/m$^2$).

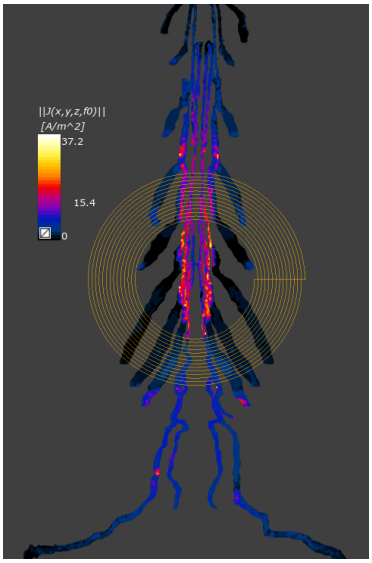


(c) The J generated in the nerves in Ella-C-R-G ($J_{max}$=37,2 A/m$^2$).

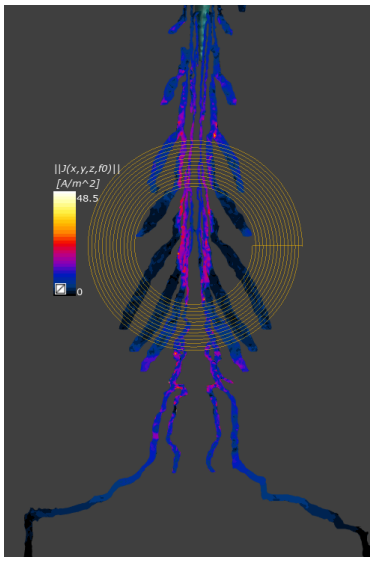


(d) The J generated in the nerves in Ella-C-R-LF and Ella-C-R-LF+G ($J_{max}$=48,5 A/m$^2$).

Figure 4.16: The J distribution created by the circular coil in a realist human model at the level of the roots. The sagital plane is in the Plane XZ in the Slice Index 229.

The same simulations were repeated with the 8-Figure coil. The 8-Figure coil was placed at T12 level and the E-field and J distributions were obtained in three simulations where the dielectric properties were changed.

The E-field distribution is shown in the Figure 4.17. In this case, the E-field intensity is very similar in all the cases and it is evidenced that the E-field that is created in the nerve roots is higher that the one that is created in the spinal cord. In general the values calculated are slightly higher in the simulation Ella-DC-SC-G.

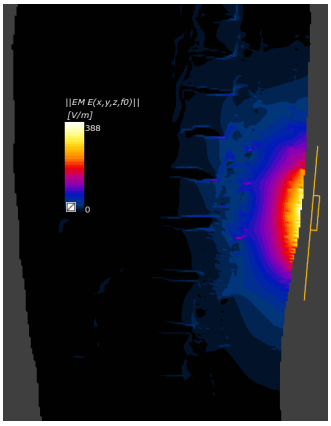


(a) The E-field created through a sagital cut in Ella-DC-SC-G ($E_{max}$=388 V/m).

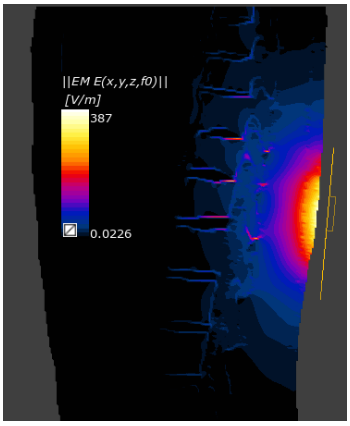


(b) The E-field calculated in Ella-DC-SC-LF and Ella-DC-SC-LF+G ($E_{max}$=387 V/m).

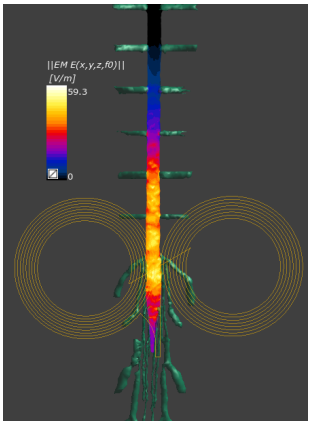


(c) The E-field generated in the spinal cord in Ella-DC-SC-G ($E_{max}$=59,3 V/m).

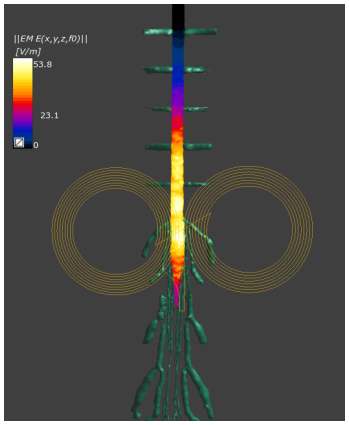


(d) The E-field generated in the spinal cord in Ella-DC-SC-LF and Ella-DC-SC-LF+G ($E_{max}$=53,8 V/m).

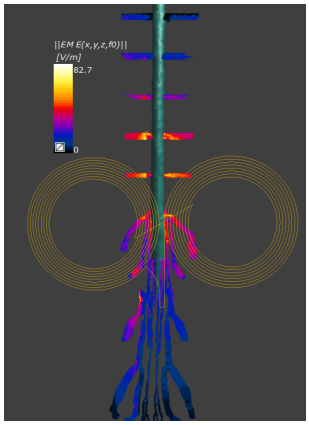


(e) The E-field generated in the nerves Ella-DC-SC-G ($E_{max}$=82,7 V/m).

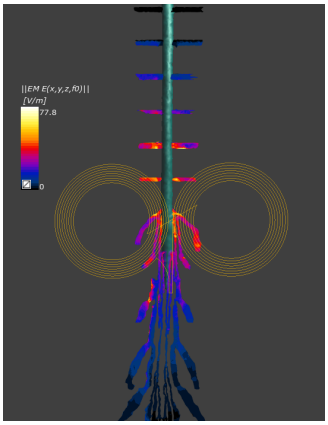


(f) The E-field generated in the nerves in Ella-DC-SC-LF and Ella-DC-SC-LF+G ($E_{max}$=77,8 V/m).

Figure 4.17: The E-field distribution created inside the human model at spinal cord level by the MS using the 8-Figure coil . The sagital cut is in the Plane XZ in the Slice Index 263.

The J distribution is shown in Figure 4.18 and it doesn't show big changes between simulations. The higher intensity of J is evident in Ella-DC-SC-LF and Ella-DC-SC-LF+G as it happened with the Circular coil (see Figure 4.18c and Figure 4.18d).

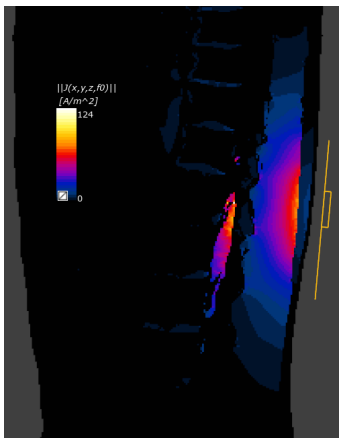


(a) The J calculated through a sagital section inside the realistic human model in Ella-DC-SC-G ($J_{max}$=124 A/m$^2$).

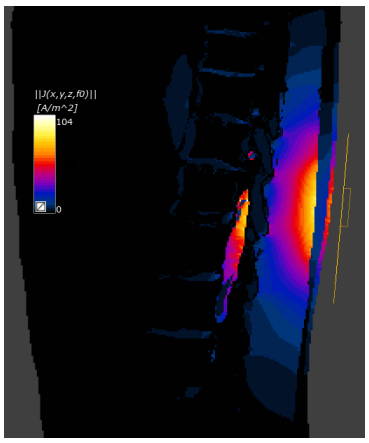


(b) The J calculated in Ella-DC-SC-LF and Ella-DC-SC-LF+G ($J_{max}$=104 A/m$^2$).

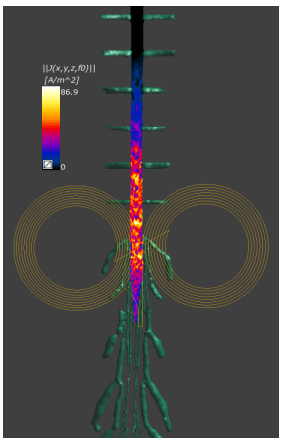


(c) The J generated in the spinal cord in Ella-DC-SC-G ($J_{max}$=86,9 A/m$^2$).

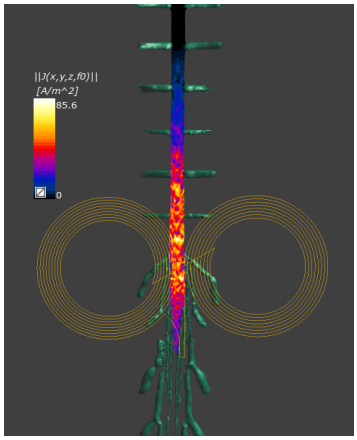


(d) The J generated in the spinal cord in Ella-DC-SC-LF and Ella-DC-SC-LF+G ($J_{max}$=85,6 A/m$^2$).

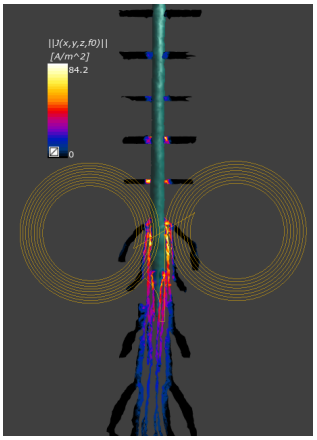


(e) The J created in the nerves in Ella-DC-SC-G ($J_{max}$=84,2 A/m$^2$).

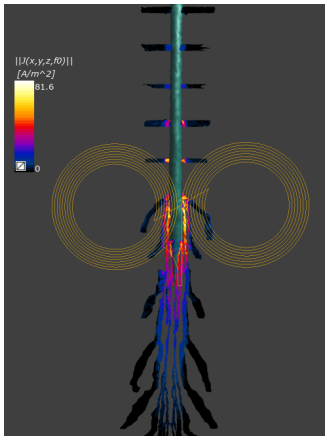


(f) The J created in the nerves in Ella-DC-SC-LF and Ella-DC-SC-LF+G ($J_{max}$=81,6 A/m$^2$).

Figure 4.18: The J distribution created inside the realistic human model by the 8-Figure coil at the spinal cord level. The sagital cut is in the Plane XZ in the Slice Index 263.

When comparing the results from the Circular coil with the 8-Figure coil, there are some conclusions that can be extrapolated. In general, the E-field distribution created by the Circular coil is higher as expected due to the results previously obtained with the Multi-layered model. The J distribution is similar between the two coils, although a bit higher for the circular coil, which is also expected.

Finally, the 8-Figure coil was placed at L5 level. The E-field and J distributions for all the simulations are shown in Figure 4.19 and Figure 4.20, respectively. The distribution of the E-field and J is very similar in all simulations, their values at the level of the roots is very similar.

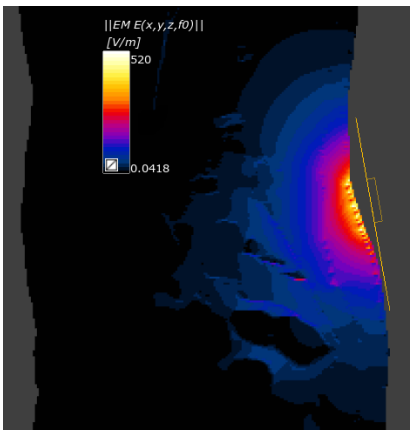


(a) The E-field generated throught a sagital cut ($E_{max}$=520 V/m) in Ella-DC-R-G.

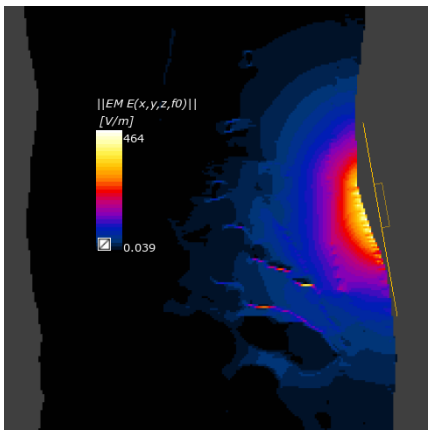


(b) The E-field created in Ella-DC-R-LF and Ella-DC-R-LF+G ($E_{max}$=464 V/m).

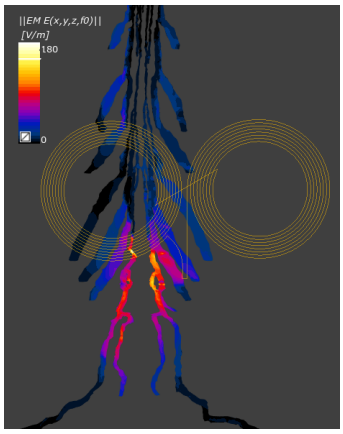


(c) The E-field generated in Ella-DC-R-G ($E_{max}$=180 V/m).

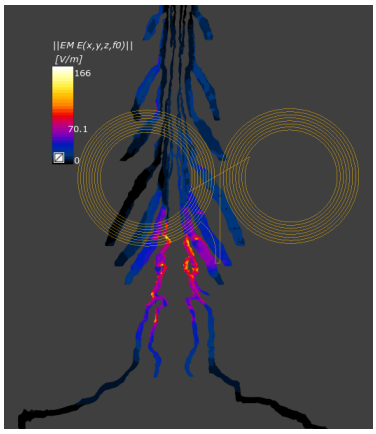


(d) The E-field generated in Ella-DC-R-LF and Ella-DC-R-LF+G ($E_{max}$=166 V/m).

Figure 4.19: The E-field distribution created by the 8-Figure coil at the level of the roots. The sagital cut is in the Plane XZ in the Slice Index 229

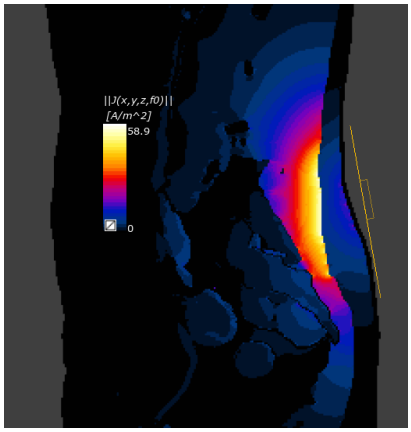


(a) The J created through the sagital cut in Ella-DC-R-G ($J_{max}$=58,9 V/m).

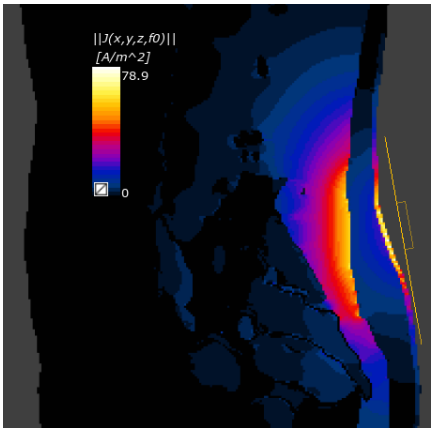


(b) The J created in Ella-DC-R-LF and Ella-DC-R-LF+G ($E_{max}$=78,9 V/m).

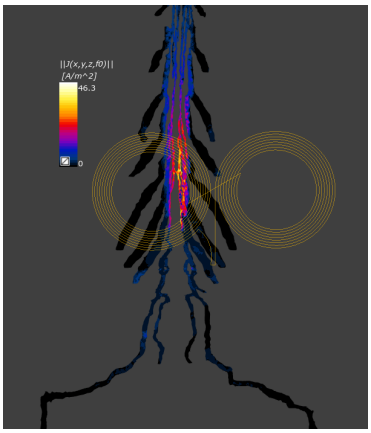


(c) The J generated in Ella-DC-R-G ($E_{max}$=46,3 V/m).

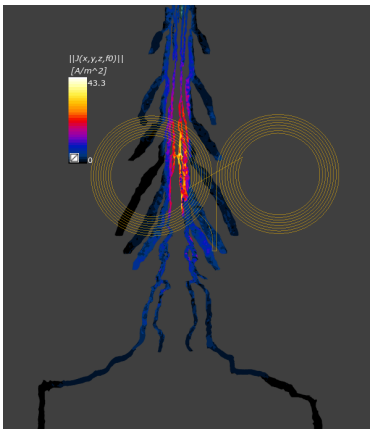


(d) The J generated in Ella-DC-R-LF and Ella-DC-R-LF+G ($E_{max}$=43,3 V/m).

Figure 4.20: The J distribution created by the 8-Figure coil place at the level of the roots. The sagital cut is in the Plane XZ in the Slice Index 229.

When comparing the Figures 4.19c and 4.19d with Figures 4.20c and 4.20d, it is easy to see that the relation Equation 2.20 is not straightforward when we are studying it in the human body. This comparison shows that the volume where the J has higher intensity is not the same volume where the E-field has high intensity. As a consequence, it is predicted that the orientation of the coil in relation to the fibres is also a relevant parameter for the J distribution.

Comparing Ella-C-SC-G, Ella-C-SC-LF and Ella-C-SC-LF+G with Ella-DC-SC-G, Ella-DC-SC-LF and Ella-DC-SC-LF+G, we can see that the E-field intensity is much higher in simulations where the circular coil was used. As it was mentioned before, this is an indicator that this coil might allow a deeper stimulation. The J-distribution is similar for both coils, while based on Equation 2.20 predicts that J should be higher for the Circular coil. This is not verified when the coils are placed in L5 and it might be due to the orientation of the fibres in relation to the coil. Further studies where the orientation

of the coils is studied should be done in order to understand what it the place where it should fixed.

The E-field intensity created by stimulating at T12 level is way lower than when the coil is placed at L5 level, which might indicate that it is easier to stimulate the neuronal circuitry at this second level.

As it was shown, the results obtained of E-field distribution diverge when the simulation used the tissue properties from the standard database to when $\sigma$ is taken from the LF database. The different $\sigma$ values and geometry of the biological tissues justify the differences in the field distribution. Furthermore, as it was said in Section 2.5.2, the E-field is calculated through Equation 2.30 and $\sigma$ is the dielectric property that is used to calculate the scalar potential. Thus, the E-field distribution varies when $\sigma$ values differ (see Figure 4.13a and Figure 4.13d).

CHAPTER 5

# Conclusions

This study is a proof of concept of the use of computational methods to fully understand the mechanisms of spinal cord magnetic stimulation. As it was mentioned in the Section 2.5, there are four main steps that should be followed until this treatment is fully understood. The goal of this thesis is to calculate the field distribution inside the human body during spinal cord magnetic stimulation, which corresponds to the first step. The approach used involved the platform Sim4Life to solve the electromagnetic problems, databases of properties of the biological tissues and a realistic human body model. Furthermore, it was ensured that the stimulation device was properly defined and simulations in a simplistic and realistic human model model were performed.

The characterization of the Single 90 mm and Double 70 mm coils was properly done, as it can be seen in Table 4.1. The values that were obtained by simulating in air and in skin are very close from the values measured by the Magstim. Additionally, the simulations showed that each coil could be approximated to a closed current path.

A Multi-Layered model based on a realistic human model is a useful tool to predict some effects of MS. At first, two coils were used to study the effect of changing the stimulation device. These coils were the Single 90 mm and the Double 70 mm from Magstim. As expected, the stimulation with the 8-Figure coil leads to a much more focused field distribution than in the case of the Circular coil. Moreover, although the 8-Figure coil has a higher intensity of E-field at its surface, it decays faster than the Circular coil, which makes the latter able to penetrate deeper regions due to difference of diameter between coils. The effect of the dielectric properties showed that the E-field doesn't vary a lot with this geometry and that the conduction current (J) varies with different values of electric conductivity.

The simulations done with a realistic human body studied the influence of the use of different coils, placed in two positions and the use of different databases of dielectric

properties. The E-field distribution inside the human body the importance of using a realist model, since the human body is very heterogeneous. Futhermore, it was shown that the stimulation at deeper regions is more difficult due to the decay of E-field with an increased distance from the coil so, it is easier to create a contraction of the muscle at the level L5.

The relation between the orientation of the coil in relation to the volume that is aimed to be stimulated is very important. As it was mentioned in Section 2.2.2, the orientation of the neurons in relation to the E-field determines if the neuron will be activated after stimulation.

The results of using different databases showed that the parameter that is more relevant to the calculation of the field intensity is the electric conductivity, as it is expected due to what is explained in Section 2.5.2. The use of different databases revealed more importance in the study with a more complex geometry. Thus, as it was mentioned before, the dielectric properties of the biological tissues for low frequencies need to be further studied. In this way, it can be ensured the proper modelling of the biological tissues. The differences between the results obtained by using different databases might not be significant enough to alter the state of depolarization or hyperpolarization of the neuron but also this needs to be studied.

In the macroscopic point of view, the parameter that is usually used for determining neuronal stimulation is the electric conduction current. In Reference [78] they give values of conduction current that might lead to the stimulation of neurons. A better approach would be to use the microscopic scale, where it is possible to predict which neurons are actually stimulated during intervention, as well as its timing. In this case, a complex neuronal circuitry model should be modelled. The spatial derivative of the E-field along the axon (activation function) is used to predict the stimulation, as it happens in the cable model (see Section 2.2.2.1). The platform T-Neuron can simulate the neuron activation due to an E-field [86]. In this case, the second step to fully understand the mechanisms of spinal cord stimulation would be studied (Section 2.5).

The solver that has the following limitations: it only allows the study of each single pulse delivered by the coil to the body-not allowing to study the effect of the repetition in the stimulation. This limitation makes the task of studying the fields in time harder. One way of studying this in time is by doing the spectral analysis of the input current and simulate the experiment with the frequencies that are more relevant. Then, the field intensity in the frequency domain is obtained. The application of an inverse Fourier transform to this spectrum can allow to establish the field distribution in time.

It would be also interesting to study magnetic stimulation with different realistic human body models in order to understand the impact that different genders and body composition might have in the output results.

Finally, this master thesis had as main goal to characterize the field distribution during spinal cord magnetic stimulation. Although the goal wasn't fully achieved, many problems and topics that should be further studied were revealed and that's the relevance of this study.

Instead of solving the problem, problems inside this topic that are not fully understood are described and discussed. The results obtained still can not be used for improving the protocols used in magnetic stimulation but, extra simulations should be done to improve them and give a better insight about spinal cord magnetic stimulation.

# Bibliography


[1] M. Wyndaele and J. J. Wyndaele. *Incidence, prevalence and epidemiology of spinal cord injury: What learns a worldwide literature survey?* 2006. DOI: 10.1038/sj.sc.3101893.

[2] L. Dobkin, Bruce; Havton. "Basic Advances and New Avenues in Therapy of Spinal Cord Injury." In: *Annu Rev Med* 55 (2004), pp. 255–282. DOI: 10.1146/annurev.med.55.091902.104338.Basic.

[3] N. A. Silva, N. Sousa, R. L. Reis, and A. J. Salgado. "From basics to clinical: A comprehensive review on spinal cord injury." In: *Progress in Neurobiology* 114 (2014), pp. 25–57. ISSN: 18735118. DOI: 10.1016/j.pneurobio.2013.11.002.

[4] K. Nas, L. Yazmalar, V. Şah, A. Aydın, and K. Öneş. "Rehabilitation of spinal cord injuries." In: *World journal of orthopedics* 6.1 (2015), pp. 8–16. ISSN: 2218-5836. DOI: 10.5312/wjo.v6.i1.8. URL: http://www.pubmedcentral.nih.gov/articlerender.fcgi?artid=4303793{\&}tool=pmcentrez{\&}rendertype=abstract.

[5] A. Frigon and S. Rossignol. "Functional plasticity following spinal cord lesions." In: *Progress in brain research* 157.5 14 (2006), pp. 231–260. ISSN: 0079-6123. DOI: 10.1016/S0079-6123(06)570. URL: http://www.sciencedirect.com/science/article/pii/S0079612306570165{\%}5Cnhttp://www.ncbi.nlm.nih.gov/pubmed/17167915.

[6] S. L. Gonzalez Andino, C. Herrera-Rincon, F. Panetsos, and R. Grave de Peralta. "Combining BMI stimulation and mathematical modeling for acute stroke recovery and neural repair." In: *Frontiers in Neuroscience* JUL (2011). ISSN: 16624548. DOI: 10.3389/fnins.2011.00087.

[7] F. L. Da Silva. "EEG: Origin and measurement." In: *EEG - fMRI: Physiological Basis, Technique, and Applications*. 2010, pp. 19–38. ISBN: 9783540879183. DOI: 10.1007/978-3-540-87919-0_2. arXiv: arXiv:1011.1669v3.

[8] E. Miyamoto. "Molecular mechanism of neuronal plasticity: induction and maintenance of long-term potentiation in the hippocampus." In: *Journal of pharmacological sciences* 100.5 (2006), pp. 433–442. ISSN: 1347-8613. DOI: 10.1254/jphs.CPJ06007X.

[9] M.-S. Rioult-Pedotti, J. P. Donoghue, and A. Dunaevsky. "Plasticity of the Synaptic Modification Range." In: *Journal of Neurophysiology* 98.6 (2007), pp. 3688–3695. ISSN: 0022-3077. DOI: 10.1152/jn.00164.2007. URL: http://jn.physiology.org/cgi/doi/10.1152/jn.00164.2007.

[10] V. Di Lazzaro, P. Profice, F. Pilato, F. Capone, F. Ranieri, P. Pasqualetti, C. Colosimo, E. Pravatã, A. Cianfoni, and M. Dileone. "Motor cortex plasticity predicts recovery in acute stroke." In: *Cerebral Cortex* 20.7 (2010), pp. 1523–1528. ISSN: 10473211. DOI: 10.1093/cercor/bhp216.

[11] E. Castel-Lacanal, P. Marque, J. Tardy, X. De Boissezon, V. Guiraud, F. Chollet, I. Loubinoux, and M. S. Moreau. "Induction of cortical plastic changes in wrist muscles by paired associative stimulation in the recovery phase of stroke patients." In: *Neurorehabilitation and Neural Repair* 23.4 (2009), pp. 366–372. ISSN: 15459683. DOI: 10.1177/1545968308322841.

[12] E. Neufeld, I. V. Oikonomidis, M. I. Iacono, E. Akinnagbe, L. M. Angelone, W. Kainz, and N. Kuster. "Simulation platform for coupled modeling of EM-induced neuronal dynamics and functionalized anatomical models." In: *International IEEE/EMBS Conference on Neural Engineering, NER*. Vol. 2015-July. 2015, pp. 517–520. ISBN: 9781467363891. DOI: 10.1109/NER.2015.7146673.

[13] M. C. Gosselin, E. Neufeld, H. Moser, E. Huber, S. Farcito, L. Gerber, M. Jedensjo, I. Hilber, F. D. Gennaro, B. Lloyd, E. Cherubini, D. Szczerba, W. Kainz, and N. Kuster. "Development of a new generation of high-resolution anatomical models for medical device evaluation: The Virtual Population 3.0." In: *Physics in Medicine and Biology* 59.18 (2014), pp. 5287–5303. ISSN: 13616560. DOI: 10.1088/0031-9155/59/18/5287.

[14] A. Christ, W. Kainz, E. G. Hahn, K. Honegger, M. Zefferer, E. Neufeld, W. Rascher, R. Janka, W. Bautz, J. Chen, B. Kiefer, P. Schmitt, H. P. Hollenbach, J. Shen, M. Oberle, D. Szczerba, A. Kam, J. W. Guag, and N. Kuster. "The Virtual Family - Development of surface-based anatomical models of two adults and two children for dosimetric simulations." In: *Physics in Medicine and Biology* 55.2 (2010). ISSN: 00319155. DOI: 10.1088/0031-9155/55/2/N01.

[15] J. C. Horvath, J. M. Perez, L. Forrow, F. Fregni, and A. Pascual-Leone. "Transcranial magnetic stimulation: A historical evaluation and future prognosis of therapeutically relevant ethical concerns." In: *Journal of Medical Ethics* 37.3 (2011), pp. 137–143. ISSN: 03066800. DOI: 10.1136/jme.2010.039966.

[16] P. A. Merton and H. B. Morton. *Stimulation of the cerebral cortex in the intact human subject*. 1980. DOI: 10.1038/285227a0.

[17] A. T. Barker, R. Jalinous, and I. L. Freeston. "Non-Invasive Magnetic Stimulation of Human Motor Cortex." In: *The Lancet* 325.8437 (1985), pp. 1106–1107. ISSN: 01406736. DOI: 10.1016/S0140-6736(85)92413-4.

[18] W. Klomjai, R. Katz, and A. Lackmy-Vallée. "Basic principles of transcranial magnetic stimulation (TMS) and repetitive TMS (rTMS)." In: *Annals of Physical and Rehabilitation Medicine* 58.4 (2015), pp. 208–213. ISSN: 18770665. DOI: 10.1016/j.rehab.2015.05.005.

[19] W. J. Levy, V. E. Amassian, M. Traad, and J. Cadwell. "Focal magnetic coil stimulation reveals motor cortical system reorganized in humans after traumatic quadriplegia." In: *Brain Research* 510.1 (1990), pp. 130–134. ISSN: 00068993. DOI: 10.1016/0006-8993(90)90738-W.

[20] L Bunday and M Perez. "Motor Recovery after Spinal Cord Injury Enhanced by Strengthening Corticospinal Synaptic Transmission." In: 22.24 (2012), pp. 2355–2361. DOI: 10.1016/j.cub.2012.10.046.Motor.

[21] P. H. Ellaway, M. Catley, N. J. Davey, A. Kuppuswamy, P. Strutton, H. L. Frankel, A. Jamous, and G. Savic. "Review of physiological motor outcome measures in spinal cord injury using transcranial magnetic stimulation and spinal reflexes." In: *Journal Of Rehabilitation Research And Development* 44.1 (2007), pp. 69–76. ISSN: 1938-1352. DOI: 10.1682/JRRD.2005.08.0140. URL: http://www.ncbi.nlm.nih.gov/pubmed/17551860.

[22] M. Oudega and M. A. Perez. "Corticospinal reorganization after spinal cord injury." In: *Journal of Physiology* 590.16 (2012), pp. 3647–3663. ISSN: 00223751. DOI: 10.1113/jphysiol.2012.233189.

[23] P. M. Rossini and S. Rossi. *Transcranial magnetic stimulation: Diagnostic, therapeutic, and research potential.* 2007. DOI: 10.1212/01.wnl.0000250268.13789.b2.

[24] E. A. Allen, B. N. Pasley, T. Duong, and R. D. Freeman. "Transcranial magnetic stimulation elicits coupled neural and hemodynamic consequences." In: *Science* 317.5846 (2007), pp. 1918–1921. ISSN: 00368075. DOI: 10.1126/science.1146426. arXiv: 9809069v1 [arXiv:gr-qc].

[25] J. M. Hoogendam, G. M. J. Ramakers, and V. Di Lazzaro. "Physiology of repetitive transcranial magnetic stimulation of the human brain." In: *Brain Stimulation* 3.2 (2010), pp. 95–118. ISSN: 1935861X. DOI: 10.1016/j.brs.2009.10.005. URL: http://dx.doi.org/10.1016/j.brs.2009.10.005.

[26] F Maeda, J. P. Keenan, J. M. Tormos, H Topka, and A Pascual-Leone. "Modulation of corticospinal excitability by repetitive transcranial magnetic stimulation." In: *Clinical Neurophysiology* 111 (2000), pp. 800–805. ISSN: 1388-2457. DOI: 10.1016/s1388-2457(99)00323-5.

[27] K. Stefan. "Induction of plasticity in the human motor cortex by paired associative stimulation." In: *Brain* 123.3 (2000), pp. 572–584. ISSN: 14602156. DOI: 10.1093/brain/123.3.572. URL: https://academic.oup.com/brain/article-lookup/doi/10.1093/brain/123.3.572.

[28] A. Wolters. "A Temporally Asymmetric Hebbian Rule Governing Plasticity in the Human Motor Cortex." In: *Journal of Neurophysiology* 89.5 (2003), pp. 2339–2345. ISSN: 0022-3077. DOI: 10.1152/jn.00900.2002. URL: http://jn.physiology.org/cgi/doi/10.1152/jn.00900.2002.

[29] K. A. McConnell, Z. Nahas, A. Shastri, J. P. Lorberbaum, F. A. Kozel, D. E. Bohning, and M. S. George. "The transcranial magnetic stimulation motor threshold depends on the distance from coil to underlying cortex: A replication in healthy adults comparing two methods of assessing the distance to cortex." In: *Biological Psychiatry* 49.5 (2001), pp. 454–459. ISSN: 00063223. DOI: 10.1016/S0006-3223(00)01039-8.

[30] B. N. Pasley, E. A. Allen, and R. D. Freeman. "State-Dependent Variability of Neuronal Responses to Transcranial Magnetic Stimulation of the Visual Cortex." In: *Neuron* 62.2 (2009), pp. 291–303. ISSN: 08966273. DOI: 10.1016/j.neuron.2009.03.012.

[31] V. Di Lazzaro, M. Dileone, F. Pilato, F. Capone, G. Musumeci, F. Ranieri, V. Ricci, P. Bria, R. Di Iorio, C. de Waure, P. Pasqualetti, and P. Profice. "Modulation of motor cortex neuronal networks by rTMS: comparison of local and remote effects of six different protocols of stimulation." In: *Journal of Neurophysiology* 105.5 (2011), pp. 2150–2156. ISSN: 0022-3077. DOI: 10.1152/jn.00781.2010. URL: http://jn.physiology.org/cgi/doi/10.1152/jn.00781.2010.

[32] M. T. Rubens and T. P. Zanto. "Parameterization of transcranial magnetic stimulation." In: *Journal of Neurophysiology* 107.5 (2012), pp. 1257–1259. ISSN: 0022-3077. DOI: 10.1152/jn.00716.2011. URL: http://jn.physiology.org/cgi/doi/10.1152/jn.00716.2011.

[33] P. J. Basser and B. J. Roth. "Stimulation of a myelinated nerve axon by electromagnetic induction." In: *Medical & Biological Engineering & Computing* (1991). ISSN: 01400118. DOI: 10.1007/BF02446708.

[34] K. P. Esselle and M. a. Stuchly. "Neural stimulation with magnetic fields: Analysis of induced electric fields." In: *IEEE Transactions on Biomedical Engineering* (1992). ISSN: 00189294. DOI: 10.1109/10.142644.

[35] W. Wang and S. Eisenberg. "A three-dimensional finite element method for computing magnetically induced currents in tissues." In: *IEEE Transactions on Magnetics* 30.6 (1994). ISSN: 0018-9464. DOI: 10.1109/20.334289.

[36] J. Ladenbauer, K. Minassian, U. S. Hofstoetter, M. R. Dimitrijevic, and F. Rattay. "Stimulation of the human lumbar spinal cord with implanted and surface electrodes: A computer simulation study." In: *IEEE Transactions on Neural Systems and Rehabilitation Engineering* 18.6 (2010), pp. 637–645. ISSN: 15344320. DOI: 10.1109/TNSRE.2010.2054112.

[37] E. Neufeld, I. V. Oikonomidis, M. Iacono, L. Angelone, W. Kainz, and N. Kuster. "Investigation of Assumptions Underlying Current Safety Guidelines on EM-Induced Nerve Stimulation." In: *Physics in Medicine and Biology* 4466 (2016), p. 4466. ISSN: 0031-9155. DOI: 10.1088/0031-9155/61/12/4466. URL: http://dx.doi.org/10.1088/0031-9155/61/12/4466.

[38] M. Davids, B. Guérin, M. Malzacher, L. R. Schad, and L. L. Wald. "Predicting Magnetostimulation Thresholds in the Peripheral Nervous System using Realistic Body Models." In: *Scientific Reports* 7.1 (2017), pp. 1–14. ISSN: 20452322. DOI: 10.1038/s41598-017-05493-9.

[39] C. Gabriel, S. Gabriel, and E Corthout. "The dielectric properties of biological tissues: 1. Literature survey." In: *Physics in medicine and biology* 41.11 (1996), p. 2231.

[40] S Gabriel, R. W. Lau, and C Gabriel. "The dielectric properties of biological tissues: II. Measurements in the frequency range 10 Hz to 20 GHz." In: *Physiologiy Medical Biology* 41 (1996), pp. 2251 –2269. ISSN: 0031-9155. DOI: 10.1088/0031-9155/41/11/002.

[41] S Gabriel, R. W. Lau, and C Gabriel. "The dielectric properties of biological tissues .3. Parametric models for the dielectric spectrum of tissues." In: *Physics in Medicine and Biology* 41.11 (1996), pp. 2271–2293. DOI: 10.1088/0031-9155/41/11/003.

[42] S. Bestmann, A. O. D. Berker, and J. Bonaiuto. "Understanding the behavioural consequences of noninvasive brain stimulation." In: *Trends in Cognitive Sciences* 19.1 (2015), pp. 13–20. ISSN: 1364-6613. DOI: 10.1016/j.tics.2014.10.003. URL: http://dx.doi.org/10.1016/j.tics.2014.10.003.

[43] M. Bikson, D. Q. Truong, A. P. Mourdoukoutas, M. Aboseria, N. Khadka, D. Adair, and A. Rahman. "Modeling sequence and quasi-uniform assumption in computational neurostimulation." In: *Computational Neurostimulation*. Ed. by S. Bestmann. 1st Editio. Vol. 222. Elsevier, 2015. Chap. 1, pp. 1–22. ISBN: 9780444635471.

[44] E. Neufeld, M. I. Iacono, E. Akinnagbe, J. Wolf, I. V. Oikonomidis, D. Sharma, B. Wilm, M. Wyss, A. Jakab, E. Cohen, N. Kuster, W. Kainz, and L. M. Angelone. "Computational platform combining detailed and precise functionalized anatomical phantoms with EM-Neuron interaction modeling." In: *2014 31th URSI General Assembly and Scientific Symposium, URSI GASS 2014* (2014). DOI: 10.1109/URSIGASS.2014.6930117.

[45] S. Gabriel. *Compilation of the Dielectric Properties of Body Tissues At Rf and Microwave Frequencies*. 1996. DOI: ReportN.AL/OE-TR-1996-0037.

[46] Van-De-Graaff. "Human Anatomy." In: *McGraw-Hill* (2001).

[47] D. Vander, A.; Sherman, J.; Luciano. "Human Physiology: The Mechanisms of Body Function." In: *McGraw-Hill* (2001).

[48] C. Watson and G. Kayalioglu. "The Organization of the Spinal Cord." In: *The Spinal Cord*. 2009, pp. 1–7. ISBN: 9780123742476. DOI: 10.1016/B978-0-12-374247-6.50005-5.

[49] O. Bican, A. Minagar, and A. A. Pruitt. "The Spinal Cord. A Review of Functional Neuroanatomy." In: *Neurologic Clinics* 31.1 (2013), pp. 1–18. ISSN: 07338619. DOI: 10.1016/j.ncl.2012.09.009. URL: http://dx.doi.org/10.1016/j.ncl.2012.09.009.

[50] M.-p. Côté, L. M. Murray, and M. Knikou. "Spinal Control of Locomotion: Individual Neurons, Their Circuits and Functions." In: *Frontiers in Physiology* 9.June (2018), p. 784. ISSN: 1664-042X. DOI: 10.3389/fphys.2018.00784.

[51] S. Khalid and R. S. Tubbs. "Neuroanatomy and Neuropsychology of Pain." In: *Cureus* (2017). ISSN: 2168-8184. DOI: 10.7759/cureus.1754.

[52] M. Patestas and L. P. Gartner. "Chapter 10: Ascending Sensory Pathways." In: *A Textbook of Neuroanatomy* (2009), pp. 137–170. ISSN: 0717-9502. DOI: 140510340X. arXiv: arXiv:1011.1669v3. URL: http://books.google.com/books?id=1r7qf63uXjQC{\&}pgis=1.

[53] A. Lingford-Hughes and N. Kalk. "Clinical neuroanatomy." In: *Core Psychiatry*. Ed. by P. Wright, J. Stern, and M. Phelan. 3rd Editio. Elsevier, 2012. Chap. 2, pp. 13–34. ISBN: 9780702048586.

[54] G. Kayalioglu. "Projections from the Spinal Cord to the Brain." In: *The Spinal Cord*. 2009, pp. 148–167. ISBN: 9780123742476. DOI: 10.1016/B978-0-12-374247-6.50014-6.

[55] J. Steven D. Waldman MD. "The Spinothalamic Pathway." In: *Pain Review*. 1st. 2009. Chap. 101, p. 176. ISBN: 9781416058939.

[56] P. Rea. "Chapter 9 - Spinal Tracts – Descending/Motor Pathways." In: *Essential Clinical Anatomy of the Nervous System*. Ed. by P. Rea. San Diego: Academic Press, 2015, pp. 161–176. ISBN: 978-0-12-802030-2. DOI: https://doi.org/10.1016/B978-0-12-802030-2.00009-1. URL: http://www.sciencedirect.com/science/article/pii/B9780128020302000091.

[57] D. L. Felten, M. K. O'Banion, and M. S. Maida. "15 - Motor Systems." In: *Netter's Atlas of Neuroscience (Third Edition)*. Ed. by D. L. Felten, M. K. O'Banion, and M. S. Maida. Third Edit. Philadelphia: Elsevier, 2016, pp. 391–420. ISBN: 978-0-323-26511-9. DOI: https://doi.org/10.1016/B978-0-323-26511-9.00015-1. URL: http://www.sciencedirect.com/science/article/pii/B9780323265119000151.

[58] A. Ropper and R. Brown. "Motor paralysis." In: *Principles of Neurology*. 8th. McGraw-Hill, 2005. Chap. 3, pp. 39–54. DOI: 10.1036/0071469710.

[59] A. Rossi, B. Decchi, A. Zalafi, and R. Mazzocchio. "Group Ia non-reciprocal inhibition from wrist extensor to flexor motoneurones in humans." In: *Neuroscience Letter* 191 (1995), pp. 205–207.

[60] E. Pierrot-Deseilligny and D. Burque. *The circuitry of the human spinal cord: its role in motor control and movement disorders*. Vol. 129. 2. 2005, p. 642. ISBN: 10 0-521-82581-8. DOI: 10.1017/CBO9781139026727. URL: http://www.brain.oxfordjournals.org/cgi/doi/10.1093/brain/awh731.

[61] A. Ropper and R. Brown. "Neurophysiological measurements." In: *Principles of Neurology*. 8th. McGraw-Hill, 2005. Chap. 45, pp. 39–54. DOI: 10.1036/0071469710.

[62] D. Johnston and S. M.-S. Wu. "Electrical Properties of the Excitable Membrane." In: *Foundations of Cellular Neurophysiology*. 6th editio. London, England: MIT Press Cambridge, Massachusetts, 1995. Chap. 3, pp. 39–54.

[63] D. Johnston and S. M.-S. Wu. "Ion Movement in Excitable Cells." In: *Foundations of Cellular Neurophysiology*. 6th Editio. London, England: MIT Press Cambridge, Massachusetts, 1995. Chap. 2, pp. 9–38.

[64] J. Platkiewicz and R. Brette. "A threshold equation for action potential initiation." In: *PLoS Computational Biology* 6.7 (2010), p. 25. ISSN: 1553734X. DOI: 10.1371/journal.pcbi.1000850.

[65] D. Debanne. "Long-Term Plasticity of Intrinsic Excitability : Learning Rules and Mechanisms." In: *Learning and Memory* 10 (2003), pp. 456–465. DOI: 10.1101/lm.64103.

[66] A. Rahman, B. Lafon, and M. Bikson. "Multilevel computational models for predicting the cellular effects of noninvasive brain stimulation." In: *Computational Neurostimulation*. Ed. by Vincent Walsh. 1st. London: Elsevier, 2015. Chap. 2, pp. 25–40. ISBN: 978-0-444-63546-4.

[67] J. Ruohonen, M. Ollikainen, V. Nikouline, J. Virtanen, and R. J. Ilmoniemi. "Coil design for real and sham transcranial magnetic stimulation." In: *IEEE Transactions on Biomedical Engineering* 47.2 (2000), pp. 145–148. ISSN: 00189294. DOI: 10.1109/10.821731.

[68] P. S. Tofts. "The distribution of induced currents in magnetic stimulation of the nervous system." In: *Physics in Medicine and Biology* 35.8 (1990), pp. 1119–1128. ISSN: 00319155. DOI: 10.1088/0031-9155/35/8/008.

[69] T. a. Wagner, T. a. Wagner, M. Zahn, M. Zahn, A. J. Grodzinsky, A. J. Grodzinsky, A. Pascual-Leone, and A. Pascual-Leone. "Three-dimensional head model simulation of transcranial magnetic stimulation." In: *IEEE transactions on bio-medical engineering* 51.9 (2004), pp. 1586–98. ISSN: 0018-9294. DOI: 10.1109/TBME.2004.827925. URL: http://www.ncbi.nlm.nih.gov/pubmed/15376507.

[70] S. Groppa, A. Oliviero, A. Eisen, A. Quartarone, L. G. Cohen, V. Mall, A. Kaelin-Lang, T. Mima, S. Rossi, G. W. Thickbroom, P. M. Rossini, U. Ziemann, J. Valls-Solé, and H. R. Siebner. *A practical guide to diagnostic transcranial magnetic stimulation: Report of an IFCN committee.* 2012. DOI: 10.1016/j.clinph.2012.01.010. arXiv: 9809069v1 [arXiv:gr-qc].

[71] M Hallett. "Transcranial magnetic stimulation and the human brain." In: *Nature* 406 (2000), pp. 147–150. ISSN: 0028-0836. DOI: 10.1038/35018000.

[72] L. Brown, Katlyn; Neva, Jason; Ledwell, Noah; Boyd. "Use of transcranial magnetic stimulation in the treatment of selected movement disorders." In: *Degenerative Neurological and Neuromuscular Disease* 4 (2014), pp. 133–151.

[73] C. Hovey and R. Jalinous. "The guide to magnetic stimulation." In: *Magstim* 20.4 (2006), pp. 284–287. ISSN: 0883153X.

[74] C. M. Epstein, D. G. Schwartzberg, K. R. Davey, and D. B. Sudderth MD. "Localizing the site of magnetic brain stimulation in humans." In: *Neurology* 40.4 (1990), pp. 666–666. ISSN: 0028-3878. DOI: 10.1212/WNL.40.4.666. eprint: http://n.neurology.org/content/40/4/666.full.pdf. URL: http://n.neurology.org/content/40/4/666.

[75] B. J. Roth, J. M. Saypol, M. Hallett, and L. G. Cohen. "A theoretical calculation of the electric field induced in the cortex during magnetic stimulation." In: *Electroencephalography and Clinical Neurophysiology/ Evoked Potentials* 81 (1991), pp. 47–56. ISSN: 01685597. DOI: 10.1016/0168-5597(91)90103-5.

[76] P. C. Miranda, M. Hallett, and P. J. Basser. "The electric field induced in the brain by magnetic stimulation: A 3-D finite-element analysis of the effect of tissue heterogeneity and anisotropy." In: *IEEE Transactions on Biomedical Engineering* 50.9 (2003), pp. 1074–1085. ISSN: 00189294. DOI: 10.1109/TBME.2003.816079.

[77] S. Yang, G. Xu, L. Wang, Y. Chen, H. Wu, Y. Li, and Q. Yang. "3D realistic head model simulation based on transcranial magnetic stimulation." In: *Conference proceedings : ... Annual International Conference of the IEEE Engineering in Medicine and Biology Society. IEEE Engineering in Medicine and Biology Society. Conference* 3 (2006), pp. 6469–6472. ISSN: 1557-170X. DOI: 10.1109/IEMBS.2006.260877.

[78] International Commission on Non-Ionizing Radiation. "Icnirp Guidelines for Limiting Exposure To Time - Varying Guidelines for Limiting Exposure To Time-Varying." In: *Health Physics* 74.(4) (1998), pp. 494–522; DOI: 10.1097/HP.0b013e3181f06c86.

[79] M. A. Macrì, S. Di Luzio, and S. Di Luzio. "Biological effects of electromagnetic fields." In: *International Journal of Immunopathology and Pharmacology* 15.2 (2002), pp. 95–105. ISSN: 03946320. DOI: 10.1177/039463200201500204.

[80] S. Raspopovic, M. Capogrosso, and S. Micera. "A computational model for the stimulation of rat sciatic nerve using a transverse intrafascicular multichannel electrode." In: *IEEE Transactions on Neural Systems and Rehabilitation Engineering* 19.4 (2011), pp. 333–344. ISSN: 15344320. DOI: 10.1109/TNSRE.2011.2151878.

[81] E. Purcell. "Electrostatics: Charges and Fields." In: *Electricity and Magnetism*. 2nd ed. Cambridge University Press, 2011. Chap. 1, pp. 1–40. ISBN: 9781107013605.

[82] E. Purcell. "The Magnetic Field." In: *Electricity and Magnetism*. 2nd ed. Cambridge University Press, 2011. Chap. 6, pp. 207–253.

[83] S. Team. "EM LF (LOW FREQUENCY) SOLVER." In: *Sim4Life Reference Guide*. Release 3. 2017. Chap. 6, pp. 163–180.

[84] The Magstim Company Ltd. "Magstim Coils & Accessories Operating Manual 1623-23-07." In: (2010), p. 20.

[85] D. L. Felten, M. K. O'Banion, and M. S. Maida. "9 - Peripheral Nervous System." In: *Netter's Atlas of Neuroscience (Third Edition)*. Ed. by D. L. Felten, M. K. O'Banion, and M. S. Maida. Third Edit. Philadelphia: Elsevier, 2016, pp. 153–231. ISBN: 978-0-323-26511-9. DOI: https://doi.org/10.1016/B978-0-323-26511-9.00009-6. URL: http://www.sciencedirect.com/science/article/pii/B9780323265119000096.

[86] M. L. Hines and N. T. Carnevale. "The NEURON Simulation Environment." In: *Neural Computation* 9.6 (1997), pp. 1179–1209. ISSN: 0899-7667. DOI: 10.1162/neco.1997.9.6.1179. arXiv: 1501.01854. URL: http://www.mitpressjournals.org/doi/10.1162/neco.1997.9.6.1179.